Cubic AlN/GaN multi-quantum-wells for unipolar device applications

Dem Department Physik

der Universität Paderborn

zur Erlangung des akademischen Grades eines

Doktor der Naturwissenschaften

vorgelegte

Dissertation

von

Christian Mietze

28.02.2013

Abstract

The cubic phase of group III-nitrides is characterized by the absence of strong internal piezoelectric and pyroelectric fields, which are present in the polar hexagonal phase along the c-axis and are undesirable for many optoelectronic devices. For example, in multi-quantum-wells or superlattices, these internal fields complicate the design and limit the tunability of intersubband transition energies. In polar group-III nitride QWs, the transition energy is observed to be almost independent of the well width for thick wells due to the confinement of carriers in a triangular potential caused by the internal field.

In this work, intersubband transitions in meta-stable cubic AlN/GaN and $Al_xGa_{1-x}N$/GaN superlattices are studied. The samples presented were grown using plasma assisted molecular beam epitaxy on 3C-SiC substrates, which are known to be the most adequate substrates for cubic GaN, AlN and their alloys. Growth of the samples was controlled using reflection high energy electron diffraction, which is a powerful tool to adjust parameters for the growth of the meta-stable phase.

Structural properties like dislocation densities, content of hexagonal inclusions or layer thicknesses of superlattices were investigated by high resolution X-ray diffraction. Using X-ray diffraction and simulations of the diffraction profile, it was possible to estimate the layer thickness with an accuracy of ±1 monolayer and to determine potential relaxation of the layers. Furthermore transmission electron microscopy was performed in order to get a profound understanding of superlattice growth concerning development of dislocations or layer thickness fluctuations. It could be shown that, although the surface of the samples has a certain roughness, even thin quantum wells are not broken and large areas show high crystalline quality and reproducible superlattice growth.

For optical characterization of interband transitions, low and room temperature (13 K-300 K) photoluminescence as well as cathodoluminescence spectroscopy was used while intersubband transitions were investigated by Fourier transform infrared spectroscopy in a temperature range from 4.7 K to 300 K.

Resonant tunneling through double barrier Al(Ga)N/GaN resonant tunneling diodes grown on free standing 3C-SiC was measured for the first time with peak-to-valley ratios between 1.3 and 2.7. Resonant tunneling was shown at room temperature as well as at low temperature. After disappearance in subsequent voltage sweeps, the negative differential resistance could be restored by illuminating the samples with UV-light hinting at charge trapping mechanisms.

The intersubband transition energy in Al(Ga)N/GaN superlattices could be tuned over a large spectral range by variation of the quantum well thickness, barrier thickness and barrier height. The barrier height was varied by changing the Al-content. Thus, it was possible to obtain the shortest and longest wavelength of intersubband transitions ever reported in cubic nitrides covering the technologically important 1.55 μm region as well as reaching the THz region 4.8 THz (62.5 μm). Performing a very detailed analysis of these transition energies compared to model calculations and finite elements calculations, it was possible to estimate the band discontinuities in AlN/GaN superlattices. The band offset between GaN and AlN was determined to be (55±5) % of the band gap difference in the conduction band and (45±5) % in the valence band. Thus, a conduction band offset of (1.4 ± 0.1) eV and a valence band offset of (0.5 ± 0.1) eV is obtained.

Infrared absorption was measured in asymmetric coupled quantum wells which form the basis for future optically pumped laser devices. Model calculations have shown the possibility to reach the 1.55 μm region with such devices. First experiments suggest that the doping concentration and layer thicknesses have to be controlled very carefully for these applications. Transmission electron microscopy is used to study structural properties of asymmetric coupled quantum well samples revealing thickness fluctuations as well as regions with smooth and uniform layers.

Contents

1 Introduction

Since the 1970s research on Gallium Nitride, Aluminum Nitride, Indium Nitride and their alloys has found rising interest until in the 1990s it became one of the most important materials for optoelectronic applications like solid state lighting, lasers or field effect transistors. Its possibility to cover the ultra violet (UV) spectral range and the whole visible spectrum makes it the material of choice until today. Since in 1992, the first blue light emitting diode by S. Nakamura and in 1993, the first blue laser in GaN has been realized by Nichia a lot of progress has been achieved and a lot of new challenges have turned up. In the last decades, the drawbacks of the spontaneous internal fields due to the wurtzite crystal structure of group III-nitrides have more and more come to the fore. These fields decrease the transition probability in quantum wells due to a lack of spatial overlap of the electron and hole wave functions. Furthermore, they limit the tunability of transition energies because carriers become confined in a thickness independent triangular potential. Thus, the design of devices based on intersubband transitions like quantum cascade lasers is complicated. The growth of non-polar and semi-polar nitrides has found increasing interest in the past years to avoid these strong internal fields. In these non-polar (semi-polar) nitrides, the c-axis is orthogonal (inclined) to the growth direction eliminating the field effects in the growth direction, but remaining in plane. Nevertheless, the absence of these internal fields leads to an increased transition probability and therefore to enhanced luminescence intensity and reduced shift in emission wavelength in LEDs. However, the electrical, optical, and structural properties show strong lateral anisotropy since the polarization field is now in the plane of growth. Furthermore, due to the large anisotropic biaxial stress, relaxation and cracking of AlGaN in one direction is observed. An alternative way to fabricate group-III nitrides without any spontaneous polarization fields is the growth of meta-stable real non-polar cubic (c) group-III nitrides [1]. Zinc-blende GaN, InN, and AlN epilayers and, just recently, free standing GaN substrates have been successfully synthesized using plasma assisted molecular beam epitaxy (PA-MBE) [1, 2]. Especially, the determination of optimal growth conditions for non-polar c-GaN [3] and c-AlN [4] has pushed the development of electronic and optoelectronic devices.

In my work, I have focused on the physics and applications of intersubband transitions in cubic Al(Ga)N/GaN quantum wells, multi-quantum wells and superlattices. An intersubband transition is defined as an optical transition between quasi-two-dimensional electronic states in semiconductors [5]. These quasi-two-dimensional states, in the following called subbands, are formed due to a confinement of the electron wave function in one dimension. This can easily be realized by embedding a

thin layer of a semiconductor material into another semiconductor material with a larger band gap. This layer system is called a quantum well (QW). The QW system is described in more detail in chapter 2.1. Two of the most important device applications of intersubband transitions are quantum well infrared photodetectors (QWIP) and the quantum cascade laser (QCL). Another light emitting device, but not as well known as the QCL, based on intersubband transitions is the quantum fountain laser (QFL) which is an optically pumped laser. Cubic nitrides offer great potential for all these applications due to the absence of internal fields, which makes the design of multi-quantum-wells or superlattice structures much easier. Furthermore, the tunability of the intersubband transition energy covers a larger spectral range. However, a lot of challenges have yet to be overcome. In the last years, a lot of progress in the growth and device application of cubic nitrides has been done. Just to mention a few, a hetero-junction field-effect transistor [6], resonant tunneling diodes [7], and QWIPs [8] based on zinc-blende group-III nitrides have been fabricated. Furthermore, the tunability of intersubband transitions (ISBT) from mid- to far-infrared regions in cubic AlN/GaN SLs has been shown [9]. Nevertheless, there is still work to be done.

In the first part of the experimental results 4.1, I will present the large tunability of intersubband transition energies in cubic nitrides and will thereby show infrared absorptions with the, as far as I know, lowest and highest energy ever published in this material system up to now (0.02 eV - 0.9 eV). By a very detailed analysis of transition energies and in cooperation with a theoretical physics group, we managed to determine the so far unknown band offset between cubic GaN and AlN in superlattice structures, which is of fundamental interest for the design of future devices. The height of the barrier material in a QW also determines the position of localized states. Therefore, the band offset is one of the most significant values that determine the physics in hetero-structures. For the optimization and design of optoelectronic devices based on e.g. quantum wells (QWs) the electronic band alignment at the interface between two semiconductors is an essential parameter. More precisely, the interest is on the valence band offset (VBO) and the conduction band offset (CBO), which reflect how the band-gap difference of the involved semiconductor materials is portioned between the discontinuities of the occupied and unoccupied energy bands. Due to their technological importance, the band offsets between various semiconductor alloys have been subjected to extensive experimental and computational studies. In this work, I will present results of the experimental determination of the band offset in cubic AlN/GaN superlattices.

In the following chapter 4.3 I will show recent progress in resonant tunneling. Tunneling of electrons through a potential barrier is one of the most crucial phenomena in quantum mechanics, but the investigation of tunneling processes in novel materials like cubic nitrides is also of technological interest. Resonant tunneling through quantized states in e.g. a double barrier structure is an important effect used in e.g. QCLs. For a more general understanding of current transport through multi quantum wells or superlattices, it is also very important to explore tunneling processes. Therefore, as a first step towards potential future devices, I have investigated current-voltage characteristics of Al(Ga)N /GaN double barrier structures.

Afterwards, I will show first infrared absorption results of asymmetric coupled quantum well (ACQW) samples. In ACQWs it is possible to realize a coupled three level system where population inversion and lasing can be realized by optical pumping from the occupied ground state to the second excited state. Excited electrons relax to the first excited state under emission of light while a phonon assisted scattering process is used to depopulate the first excited state and transfers electrons back to the ground state. First results of absorptions in cubic nitride ACQWs are shown in 4.4 forming another step towards a unipolar light emitting device like a quantum fountain laser.

2 Fundamentals

In this chapter, the most important fundamentals for this work are summarized. First, the physics of quantum wells and superlattices is recapitulated. The focus here lies on intersubband transitions. In the second part of this chapter, the general differences between hexagonal and cubic III-nitrides with regard to quantum wells are discussed. Furthermore, the growth of cubic AlN and GaN is described in short.

2.1 Quantum Wells

From quantum mechanics we know that, if an electron is confined in a potential well, whose width is in the same order as the de Broglie wavelength of the electron, quantization effects emerge. The electron wave function is confined in one dimension so that quantized states at higher energies than the ground state are formed. Hence, the electron can only occupy states of discrete energy. This is well known from the particle in a box model [10]. An infinite potential well with quantized states is shown in Fig. 1. The electron states are labeled with quantum numbers. The main difference between an infinite potential well and a finite well is that the electron wave function can penetrate the barrier depending on the barrier height.
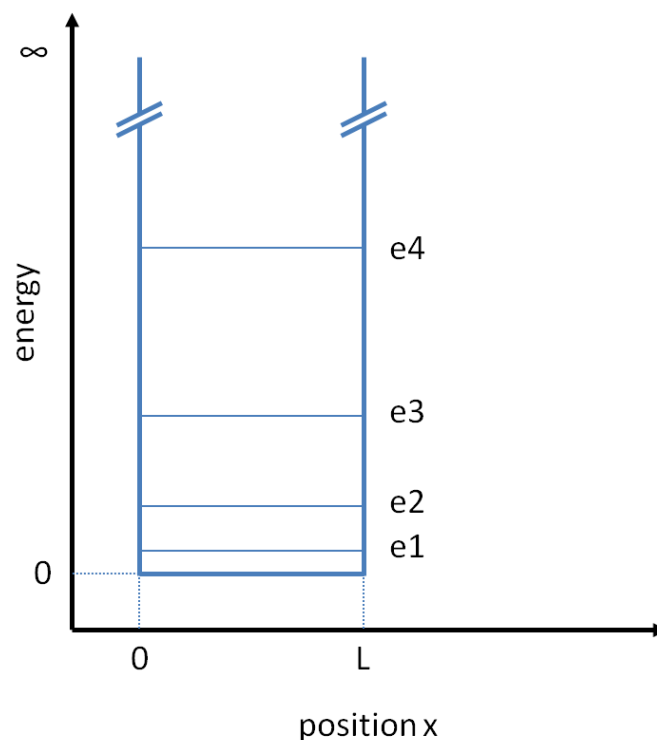

Fig. 1: Infinite potential well of width L showing quantized electron states e1-e4.

In semiconductor physics such a potential well with finite barriers is pretty easy to realize. For this purpose a thin layer of a semiconductor has to be sandwiched between two layers of another semiconductor with a larger band gap. This layer system is called a quantum well (QW). The band alignment of these double hetero structures can be classified in different types. Fig. 2 shows the band alignment for the different types of QWs. The cubic nitride system forms a type I band alignment, hence I will focus on the type I alignment.

type I   type II   type III
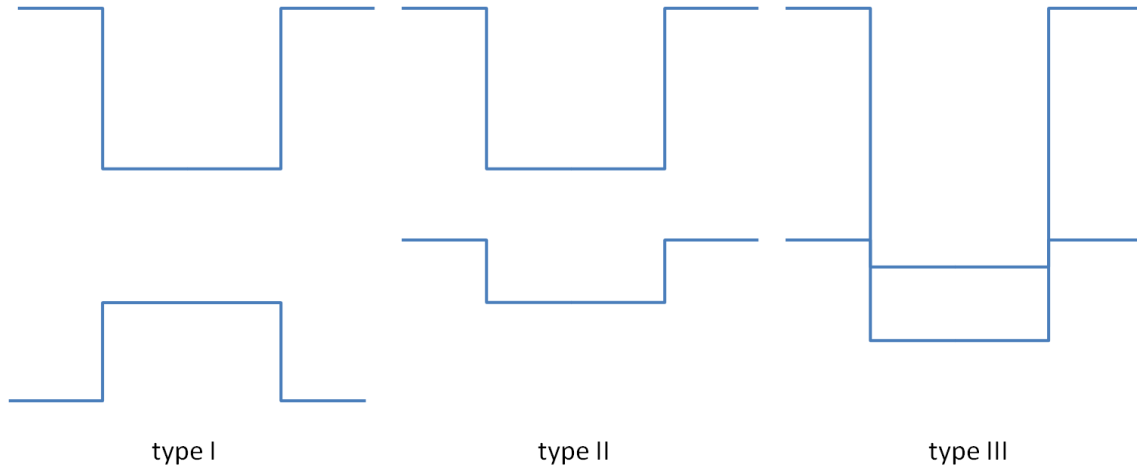
Fig. 2: Different types of band alignment in semiconductor hetero structures or quantum wells. Type I is called straddling gap, type II staggered gap and type III broken gap.

For a type I hetero-structure electrons in the conduction band are confined in one dimension as well as holes in the valence band. In Fig. 3 the band structure for such a quantum well is shown. Transitions between the different valence- and conduction-band states can be induced by different methods. Light with a suitable energy above the band gap can transfer an electron from the valence band to the ground state in the conduction band (e1) leaving a defect electron or hole in the correspondent valence band state (h1). This process is called absorption. Vice versa an electron in the conduction band can recombine with a hole in the valence band by sending out a photon with the energy of this transition. This process is called radiative recombination or light emission. But not all possible transitions between electron and hole states are allowed. The interband transitions (IBT) underlie certain selection rules. Only transitions with $\Delta n=0, 2,\dots$ are allowed (e.g. e1-h1, e2-h2) while other transitions are forbidden. In real structures with finite barrier heights these transition rules are weakened, but still the transitions with $\Delta n=0, 2,\dots$ are dominant. The position of the quantized energy levels depends on the thickness of the quantum well and on the height of the barrier. Hence the energy of a transition from the conduction band state with the lowest energy (e1) to

the highest-energy hole state (h1) can be varied over a large energy range. Taking advantage of this fact the emission energy can be tuned to a large spectral range.
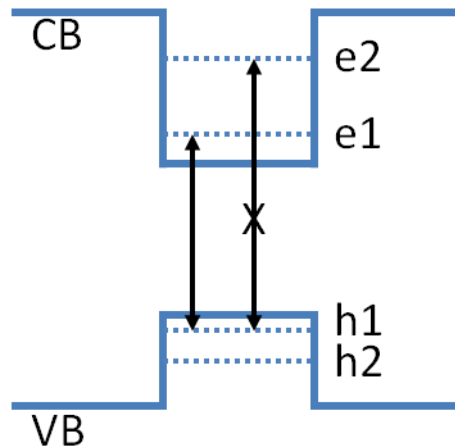
Fig. 3: Schematic band structure for a quantum well with finite barriers. Quantized electron and hole states are e1, e2 and hole states h1, h2.

A multi-layer system of periodically repeated quantum wells equal in width and separated by thin barriers is called a superlattice (SL). The main difference between multi-quantum-wells and a superlattice is the coupling of the QWs which results in a change in the density of states (DOS). The difference in the density of states between MQW and SL is schematically drawn in Fig. 4. If the barrier is thick enough to completely isolate the wave functions in two adjacent QWs, there is no interaction of charge carriers, because there is no spatial overlap of their wave functions. Thinner barriers allow the wave functions of electrons or holes in adjacent QWs to overlap and therefore interact. The step like DOS function of the MQW is softened by the formation of minibands. The width of the miniband is increasing with the quantum number and is illustrated by the widths W_1 and W_2. The width of a miniband is furthermore influenced by thickness fluctuations and surface roughness of such a periodic structure.
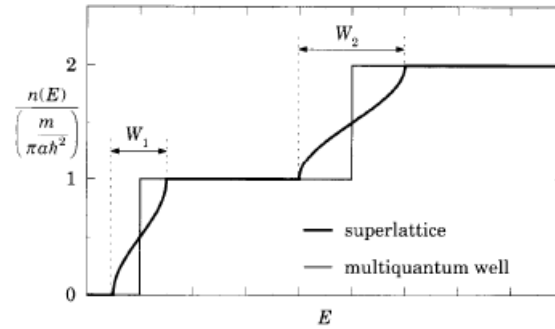
Fig. 4: Density of states versus energy for a multi quantum well system and a superlattice. The width of the formed minibands is illustrated by W_1 and W_2 [10].

Charge carriers can move freely in these minibands by resonant tunneling processes. Thus, an artificial crystal with low energy band gap can be formed by using a layer system of semiconductors with larger band gaps. Both previously described cases are shown in Fig. 5 using the example of the conduction band of two Gallium Nitride QWs separated by an Aluminum Nitride barrier. On the left hand, the barrier is thin enough to allow the electron wave functions to penetrate through the barrier and form a coupled quantum well system. On the right hand, the wave functions are decaying to zero inside the barrier material and the two quantum wells are clearly separated.
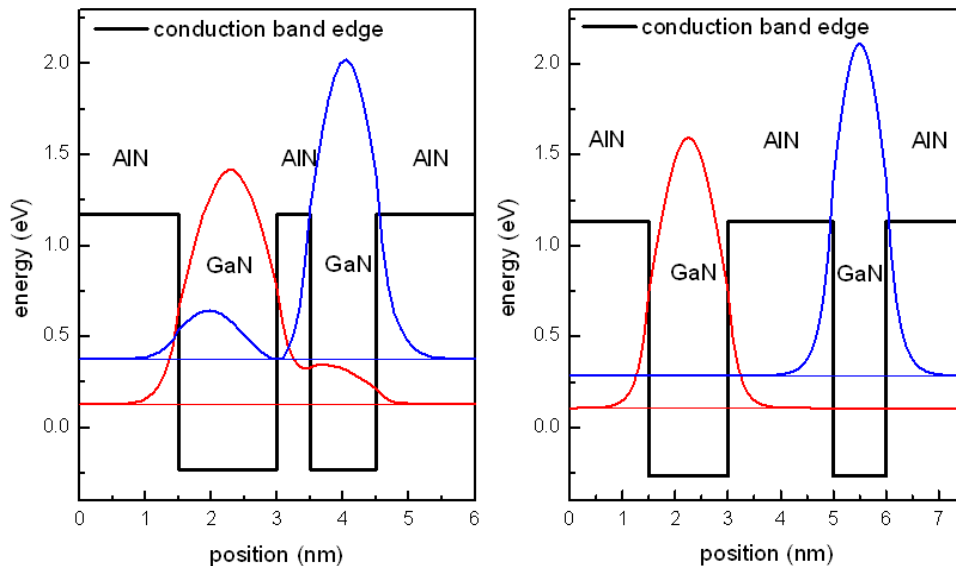
Fig. 5: Conduction band profile of two GaN QWs separated by a 0.5 nm AlN barrier (left hand side) and a 2 nm AlN barrier (right hand side). The conduction band edge in the QW region is below zero due to n-type doping in the order of 1e18cm^{-3}.

2.1.1 Intersubband Transitions

Besides the interband transition in a quantum well there are other possible transitions. "Intersubband transitions describe optical transitions between quasi-two-dimensional electronic states in semiconductors subband, which are formed due to the confinement of the electron wave function in one dimension. The formation of such low-dimensional electronic systems has been one of the major topics of semiconductor physics in the last three decades (Ando et al 1982 [11]), and in this context, the term band-structure engineering was coined. This development has been mainly triggered by epitaxial crystal growth techniques such as molecular beam epitaxy, which provides atomic-layer control of layer thickness."[12] If for example the electron ground state e1 is occupied a transition from e1 to an excited electron state e2 can occur. This process and the inverse transition are called intersubband transition (ISBT).

First I shortly want to summarize the theoretical background of absorption in a QW aligned along z-direction. This theory is perfectly described in [10] so I will cite certain passages in the following. The photon-electron interaction can be classically described using electrodynamics as an energy transfer of the electric field of the light to the electron or more general to the sample illuminated and can be calculated using the fourth Maxwell equation. After a few calculations the power P dissipated in a volume Ω is estimated to:

$$P = 2\sigma_1 \Omega E_0^2 \tag{2.1}$$

where σ_1 is the conductivity and E_0 is the amplitude of the electric field wave.

Using Fermi's golden rule a quantum mechanical expression for the overall rate of absorption of energy (the single steps can be found in [10]) can be calculated:

$$P = \frac{2\pi}{\hbar}\hbar\omega \left(\frac{eE_0}{m_0\omega}\right)^2 2\sum_{i,j}|\langle j|\boldsymbol{e}\cdot\hat{\boldsymbol{p}}|i\rangle|^2 [f(E_i) - f(E_j)]\delta(E_j - E_i - \hbar\omega) \tag{2.2}$$

$\hat{\boldsymbol{p}}$ is the momentum operator, $\boldsymbol{e}$ the vector of the electric field, $f(E_i)$ is the Fermi function of the energy state E_i and ω the frequency of the absorbed photon.

A comparison with equation (2.1) shows that the general formula for the real part of the conductivity σ_1 can be calculated as follows:

$$\sigma_1(\omega) = \frac{\pi e^2}{m_0^2 \omega} \frac{2}{\Omega} \sum_{i,j} |\langle j|e \cdot \hat{\boldsymbol{p}}|i\rangle|^2 [f(E_i) - f(E_j)]\delta(E_j - E_i \tag{2.3}$$
$$- \hbar\omega)$$

Now I want to show the calculation of bound states in a low dimensional system like a QW. The starting point to calculate the quantized states in a QW structure is the three dimensional time-independent Schrödinger equation:

$$\left[-\frac{\hbar^2}{2m}\nabla^2 + V(\boldsymbol{R})\right]\psi(\boldsymbol{R}) = E\psi(\boldsymbol{R}) \tag{2.4}$$

$V(\boldsymbol{R})$ is a general potential and $\psi(\boldsymbol{R})$ is a wave function. For a quantum well structure that potential energy depends only on the coordinate in which the QW is aligned along (here z), a purely one-dimensional Schrödinger equation in z-direction can be set up. A detailed description of the calculations can be found in [10].

$$\left[-\frac{\hbar^2}{2m}\frac{d^2}{dz^2} + V(z)\right]u(z) = \varepsilon\,u(z) \tag{2.5}$$

with
$$\varepsilon = E - \frac{\hbar^2 k_x^2}{2m} - \frac{\hbar^2 k_y^2}{2m} \tag{2.6}$$

ε is only a substitution for the energy as shown in equation (2.6) and $u(z)$ is an unknown function.

The solution for the three-dimensional problem as shown in equation (2.5) is given by the following two equations:

$$\psi_{k_x k_y n}(x, y, z) = exp(ik_x)exp(ik_y)u_n(z) \tag{2.7}$$

$$E_n(k_x k_y) = \varepsilon_n + \frac{\hbar^2 k_x^2}{2m} + \frac{\hbar^2 k_y^2}{2m} \tag{2.8}$$

Three different quantum numbers (k_x,k_y,n) are needed to label the states which is a consequence of the three spatial dimensions of the problem. In the next step, I want to shorten equations (2.7) and (2.8) by defining two-dimensional vectors for motion in the xy-plane:

$$r = (x, y) \tag{2.9}$$

$$k = (k_x, k_y) \tag{2.10}$$

$$\psi_{k,n}(r, z) = exp(ik \cdot r)u_n(z) \tag{2.11}$$

$$E_n(k) = \varepsilon_n + \frac{\hbar^2 k^2}{2m} \tag{2.12}$$

For the description of intersubband transitions, I want to concentrate only on the conduction band. From equations (2.11) (2.12) follows that localized states can be described as a product of a bound state in z-direction and a transverse plane wave:

$$\psi_{ik}(R) = A^{-1/2}\phi_i(z)exp(ik \cdot r) \tag{2.13}$$

$$E_i(k) = \varepsilon_i + \frac{\hbar^2 k^2}{2m} \tag{2.14}$$

A is the area of the QW. If the thickness of the sample is L (not the QW thickness) in growth direction (z) the volume can be defined as $\Omega{=}AL$. Each bound state i quantized along z-direction contributes to an energetic subband. The matrix element between two bound states is given by:

$$\langle jk'|e \cdot \hat{p}|ik\rangle \tag{2.15}$$

The form of the matrix element depends on the polarization of the light, or in other words the orientation of the electric field vector e.

If $e = (1,0,0)$ the electric field is parallel to the x-direction in the plane of the QW. The propagation direction of the light is then y- (in the plane of the QW) or z-direction (normal to it). In this case $e\hat{p} = -i\hbar \ \partial/\partial x$ and

$$(e \cdot \hat{p})\psi_{ik}(R) = \hbar k_x \psi_{ik}(R) \tag{2.16}$$

because the momentum operator affects only the plane wave in $\psi_{ik}(R)$.

$$\langle jk'|e \cdot \hat{p}|ik\rangle = \hbar k_x \langle jk'|ik\rangle = 0 \tag{2.17}$$

Then the integral is over the product of two states and vanishes by orthogonality. No light with this polarization vector can be absorbed in a QW. The same result is obtained for e along y-direction due to the same reason. A consequence of these results is that no light that propagates normal to the growth axis can be absorbed which is normally the case in a lot of experimental methods.

Now I want to show the case of the electric field normal to the growth axis $\left(e = (0,0,1)\right)$. In this case light has to come from the side of the sample and propagates in plane of the QW. Then the product

$$e \cdot \widehat{p} = -i\hbar \frac{\partial}{\partial z} \qquad (2.18)$$

only affects the wave function of the bound state and we obtain

$$\langle jk|e \cdot \widehat{p}|ik\rangle = \frac{1}{A}\int dz \int d^2 r \phi_j^*(z)e^{i(k-k')\cdot r}\hat{p}_z\phi_i(z) \qquad (2.19)$$

The second integral over r gives A if $k = k'$ and zero otherwise, so the two-dimensional wave vector is conserved. Thus, optical transitions are vertical in k-space. This is shown in Fig. 6. The remaining matrix element can be written as $\langle j|\hat{p}_z|i\rangle$. Putting this matrix element and the energy in equation (2.12) into the equation for general conductivity, we end up with equation (2.20):

$$\sigma_1(\omega) = \frac{\pi e^2}{m^2\omega}\frac{2}{\Omega}\sum_{i,j,k}|\langle j|\hat{p}_z|i\rangle|^2\{f[E_i(k)] - f[E_j(k)]\}$$
$$\times \delta[E_j(k) - E_i(k) - \hbar\omega] \qquad (2.20)$$

This equation can be reduced to a shorter expression following the steps below:

i.   The wave vector k cancels from the δ-function, because $E_j(k) - E_i(k) = \varepsilon_j - \varepsilon_i$, assuming an ideal system where the mass is the same for each subband. To simplify the formulas put $\hbar\omega_{ji} = \varepsilon_j - \varepsilon_i$, so the δ-function becomes $(1/\hbar)\delta(\omega - \omega_{ji})$.

ii. The wave vector k now appears only in the sums over the occupation functions. Each sum of the form $(2/A)\sum_k f[E_j(k)]$ counts the total density

of electrons with both spins occupying the subband and can be denoted by n_j.

iii. Take the frequency ω from the prefactor inside the summation. The δ-function means that each term contributes only if $\omega = \omega_{ji}$, so ω can be replaced by ω_{ji} wihout changing the value.

iv. Instead of the matrix elements themselves, introduce dimensionless *oscillator strengths* defined by

$$f_{ij} = \frac{2}{m\hbar\omega_{ij}} |\langle j|\hat{p}_z|i\rangle|^2 = \frac{2m\omega_{ij}}{\hbar} |\langle j|z|i\rangle|^2 \qquad (2.21)$$

The second form of the oscillator strength with a matrix element of z rather than $\hat{p}_z$ follows from a little trickery with operators. The diagonal oscillator strength is best excluded from the summation to ensure that transitions from a state to itself are omitted [10].

Applying the above manipulations, the simple formula below is obtained.

$$\sigma_1(\omega) = \frac{\pi e^2}{2mL} \sum_{\substack{i,j \\ j \neq i}} f_{ij}(n_i - n_j)\delta(\omega - \omega_{ji}) \qquad (2.22)$$

Absorption can only occur for frequencies matching the energy separation of bound states in the QW appearing as discrete lines in the spectrum. As I mentioned before, only vertical transitions in k-space are allowed, therefore a difference in the effective mass in the subbands results in a broadening of the discrete line. The factor of $1/L$, where L is the thickness of the quantum well, has to be replaced by the lattice period for multi-quantum-wells. Its influence becomes smaller for thicker well widths. Absorption measurements on cubic AlN/GaN superlattices can be seen in Fig. 31. The strength of an intersubband transition depends on the occupation of the lower subband and on the wave function of the localized state and thereby the oscillator strength. The occupation which corresponds to the f_{ij} can for example be manipulated by changing the doping concentration.

Last but not least I want to evaluate the matrix element

$$\langle j|\hat{p}_z|i\rangle = -i\hbar \int \phi_j^*(z)\frac{d}{dz}\phi_i(z)dz$$

(2.23)

One important result follows from the symmetry of the QW. It is known that for a symmetric QW the wave functions are either even or odd in z. The derivative d/dz changes the parity meaning that the matrix element is only non-zero if one state is even and the other odd and this gives us the selection rule for intersubband transitions (Δn=1, 3,…). Only these transitions can be observed in an optical spectrum. A schematic of the possible transitions between bound states in a QW is shown in
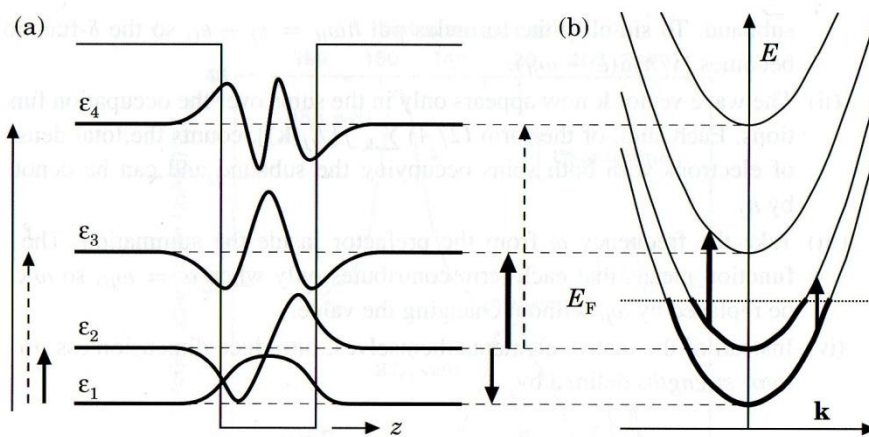
Fig. 6: Absorption by transitions between states in a quantum well. (a) Wave functions along z with energy levels. The thicknesses of the arrows are rough indications of the oscillator strength of the transitions, with broken lines signifying forbidden transitions. (b) Band structure in the transverse k-plane showing the vertical nature of the allowed transitions which must go from filled to empty state [10].

As well as for interband transitions the selection rules can be weakened or even be ignored if the inversion symmetry is broken with respect to the QW center [12]. This can be done intentionally by growing asymmetric coupled quantum wells or unintentionally by layer thickness fluctuations. Precondition for this relaxation of selection rules is the coupling between the QWs. Light absorption is furthermore only possible for electromagnetic waves with a wave vector parallel to the direction where the confinement takes place. In our case it is the growth direction of a sample. For the other directions the dipole matrix element equals zero and therefore no absorption occurs. An allowed light absorption is shown in Fig. 7.
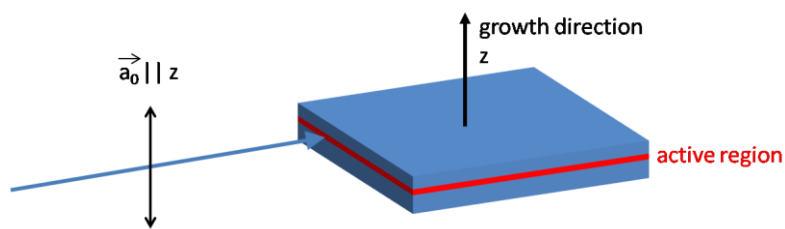
Fig. 7: Allowed intersubband absorption of light with a wave vector parallel to the growth direction.

As well as for the IBT the transition energy of an ISBT can be varied by the thickness of the quantum well and the height of the barrier.

2.2 III-Nitrides

Since in the 1970s group III-nitrides were considered as good candidates for optoelectronic device applications, a lot of research and development has been done. Forming alloys of Aluminum Nitride, Gallium Nitride and Indium Nitride the band gap of the material can be tuned from the ultra violet over the whole visible spectrum making it interesting for solid state lighting. Today, group III-nitrides are state-of-the-art materials for a diversity of optoelectronic devices like light emitting diodes, laser diodes or field effect transistors. Especially the growing market of solid state lighting has pushed the development of III-nitrides over the last two decades.

III-nitrides crystallize either in the stable hexagonal wurtzite structure or in the metastable cubic structure. The hexagonal nitrides are mainly characterized by the asymmetric charge distribution resulting in strong internal spontaneous and piezoelectric fields along the c-axis. The wurtzite structure is shown schematically in Fig. 8 using the example of gallium nitride where the green spheres represent gallium atoms and blue spheres represent nitrogen atoms.
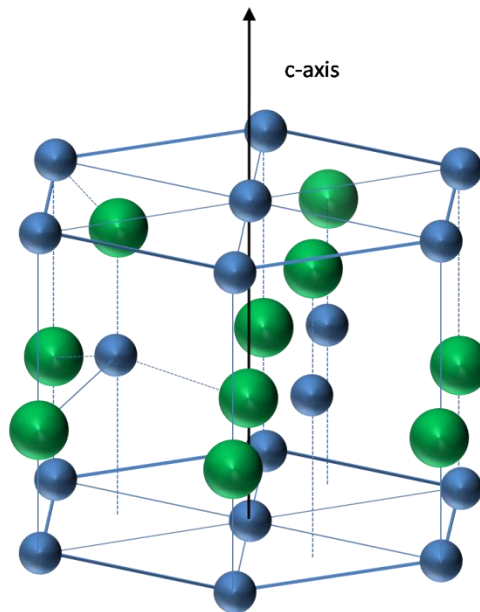
Fig. 8: Wurtzite crystal structure using the example of gallium nitride. Blue spheres represent nitrogen atoms and green spheres represent gallium atoms.

The internal fields have to be considered especially in hetero-structures or QWs where the energetic position of localized states is strongly affected. Due to the electric field, the conduction and valence band edges are bent so that the transition energy of a QW can become independent of the thickness due to a confinement of carriers in a triangular potential which does not change with the thickness of the QW. In Fig. 9 a

hexagonal GaN QW in AlN confinement layers is shown exemplarily. Using nextnano³ [13, 14] I have calculated the conduction and valence band edges which are plotted versus the growth direction. The confinement in the triangular potential and the separation of electron- and hole-wave function is clearly shown.
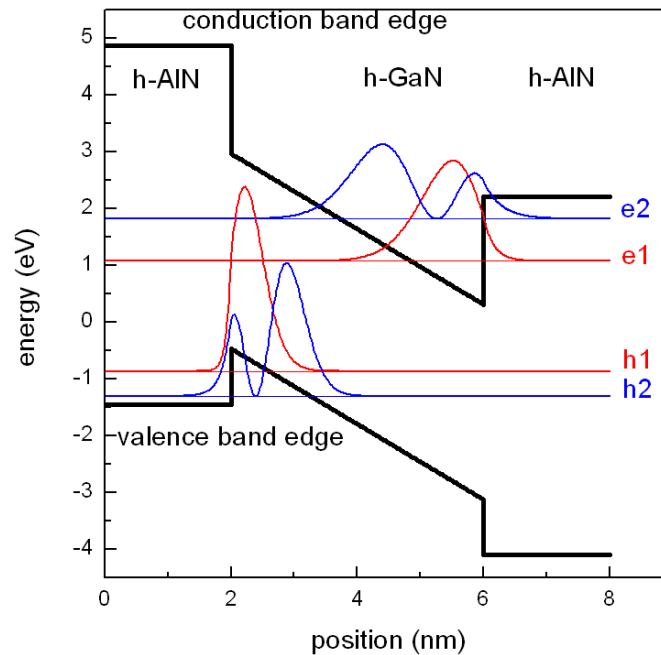
Fig. 9: Calculated band structure for a 4 nm thick GaN QW with AlN barriers. Strong bending of the band edges due to internal fields leads to a spatial separation of electron and hole wave functions.

Furthermore, this triangular potential is undesirable due to the resulting spatial separation of electrons and holes which leads to reduced transition probabilities. The lack of spatial overlap of the wave functions therefore limits the efficiency of optical devices like LEDs and lasers. The growth of non-polar and semi-polar nitrides has found increasing interest in the past years to avoid these strong internal fields. In these non-polar (semi-polar) nitrides, the c-axis is orthogonal (inclined) to the growth direction eliminating the field effects in the growth direction. The absence of these internal fields leads to an increased transition probability and therefore, to enhanced luminescence intensity and reduced shift in emission wavelength in LEDs. However, the electrical, optical, and structural properties show strong lateral anisotropy since the polarization field is now in the plane of growth. Furthermore, as a result of the large anisotropic biaxial stress, relaxation and cracking of AlGaN in one direction is observed.

An alternative way to fabricate group-III nitrides without spontaneous polarization fields is the growth of meta-stable real non-polar cubic (c) group-III nitrides [1]. The zinc-blende crystal structure of cubic GaN is shown schematically in Fig. 10. Zinc-blende GaN, InN, and AlN epilayers and just recently, free-standing GaN substrates have been

successfully synthesized using plasma assisted molecular beam epitaxy (PA-MBE) [1], [2]. Especially, the determination of optimal growth conditions for non-polar c-GaN [3] and c-AlN [4] has pushed the development of electronic and optoelectronic devices, such as hetero-junction field-effect transistors [6], resonant tunneling diodes [7], and QWIPs [8] based on zinc-blende group-III nitrides. Furthermore, the tunability of ISBTs from mid- to far-infrared regions in cubic AlN/GaN SLs has been shown.
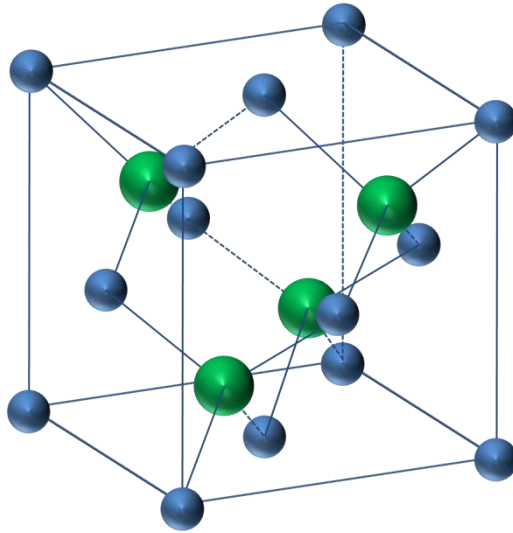
Fig. 10: Zinc-blende crystal structure of cubic GaN. Gallium atoms are represented by green spheres and nitrogen atoms by blue spheres.

2.2.1   Growth of Cubic AlN and GaN

As mentioned above, group-III nitrides crystallize either in the stable hexagonal phase or the meta-stable cubic phase. In this chapter, I want to summarize the optimal growth conditions for the cubic phase.

All samples introduced in my thesis are fabricated using PA-MBE. The optimal substrate for MBE growth of cubic nitrides has been shown to be the cubic phase of silicon carbide (3C-SiC) with a lattice constant of $a_{3C\text{-}SiC}$ = 4.36 Å, resulting in a lattice mismatch of 3.5 % in the case of c-GaN and only 0.5 % in the case of c-AlN. Research in growth techniques over the last ten years has shown that the best crystalline quality for cubic GaN is grown at a substrate temperature of 720 °C and coverage of the substrate surface by one monolayer gallium [3]. Both parameters can be adjusted using in situ reflection high energy electron diffraction (RHEED). The substrate temperature is directly connected to the gallium adsorption coefficient and can be tested by measuring the adsorption- and desorption times at a certain gallium flux. The surface coverage with one monolayer gallium during growth can be observed by the surface reconstruction of the growing GaN surface or by RHEED intensity time scans. Under metal rich conditions the GaN surface shows no reconstruction during growth. Analyzing RHEED intensity, it is possible to see the coverage with one monolayer gallium by a characteristic kink. If the intensity rises to this characteristic kink during growth the surface is covered with on monolayer gallium. The adjustment of the optimal growth conditions can be found in [3] in detail. Going from these metal rich conditions to stoichiometric or even nitrogen rich conditions the rms roughness as well as the dislocation density increases [3]. Furthermore, it has been shown in [4] that it is possible to grow atomically smooth c-AlN on 3C-SiC.

2.3 Experimental Methods

In this chapter I will describe the experimental methods used to characterize the MBE grown semiconductor layers. The samples are investigated with regard to their structural properties by high resolution X-ray diffraction (HRXRD) and transmission electron microscopy (TEM). Furthermore these two methods are used to obtain layer thicknesses of superlattices and multi-quantum-wells. Layer thickness fluctuations could be shown by TEM. Besides the structural characterization optical measurements like photoluminescence spectroscopy and infrared absorption are performed. From the optical characterization transition energies are obtained which can be compared to values from model calculations.

2.3.1 High Resolution X-Ray Diffraction

In semiconductor science HRXRD is a standard method of non-destructive ex situ characterization of epitaxial layers, hetero-structures and superlattice systems. From the intensity distribution information about the composition and crystalline quality of epitaxial layers, their thickness, and strain relaxation can be obtained. X-ray diffraction of a single crystal can be described by the Bragg equation (Eq. (2.24)) [15]:

$$\lambda = 2\, d_{hkl} \sin \omega \qquad (2.24)$$

The triplet (hkl) represents the Miller indices and d_{hkl} is given by Eq. (2.25)

$$d_{hkl} = \frac{a_0}{\sqrt{h^2 + k^2 + l^2}} \qquad (2.25)$$

where d_{hkl} represents the distance between the lattice planes, a_0 is the lattice constant of the crystal under research, λ is the wavelength of the X-rays (for my measurements the Cu $K_{\alpha 1}$ line at 1.54056 Å is used) and ω is the incident angle of the X-ray beam. A more detailed description of X-ray diffraction can be found in [16].

X-ray diffraction is usually described in reciprocal space. The reciprocal lattice of a crystal is formed by the terminal points of reciprocal repetition vectors $\overrightarrow{b_1}$, $\overrightarrow{b_2}$, and $\overrightarrow{b_3}$.

The relation between the reciprocal repetition vectors and the crystal lattice vectors $\vec{a_1}$, $\vec{a_2}$, and $\vec{a_3}$ is given by Eq.(2.26).

$$\vec{b_i} = 2\pi \; \frac{\vec{a_j} \times \vec{a_k}}{\vec{a_1} \cdot (\vec{a_2} \times \vec{a_3})}$$

(2.26)

with i,j,k cycl.

In reciprocal space the Miller indices are described by the reciprocal lattice vector $\overrightarrow{G_{hkl}}$ which is given by Eq. (2.27):

$$\overrightarrow{G_{hkl}} = h \cdot \vec{b_1} + k \cdot \vec{b_2} + l \cdot \vec{b_3}$$

(2.27)

The condition of diffraction given in Eq. (2.24) by the lattice plane (hkl) can be transferred into reciprocal space by Eq. (2.28):

$$\vec{Q} = \overrightarrow{G_{hkl}}$$

(2.28)

$\vec{Q}$ is the scattering vector defined as $\vec{Q} = \vec{k_i} - \vec{k_d}$, where $\vec{k_i}$ and $\vec{k_d}$ are the wave vectors of incident and diffracted waves as indicated in Fig. 11.
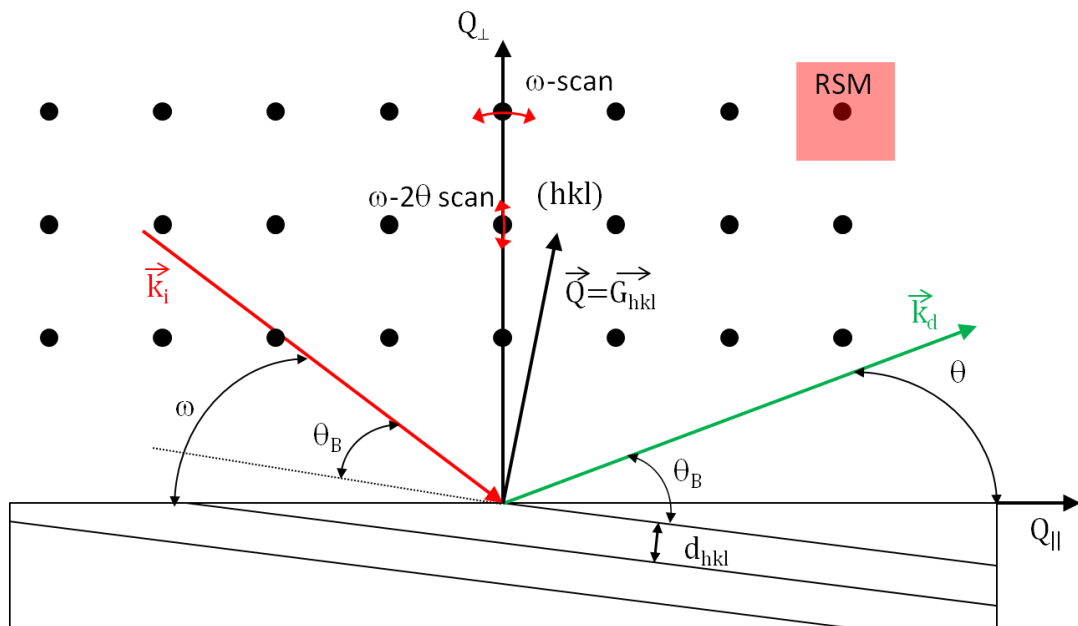
Fig. 11: Sketch of the diffraction geometry. The Bragg condition for the lattice plane (hkl) is fulfilled if the scattering vector Q ends at a reciprocal lattice point (hkl).

In reciprocal space the diffraction plane is represented as a reciprocal lattice point and the diffraction geometry defined by the incident and by the detection angles is represented by the scattering vector. When the scattering vector ends at a reciprocal lattice point (hkl) the Bragg condition is fulfilled. Scattered X-ray intensity around a reciprocal lattice point is strongly influenced by the structural properties of the crystalline material, which makes HRXRD a powerful tool in structural characterization of epitaxial layers or layer systems. A detailed analysis of diffracted intensity distribution around certain reciprocal lattice points allows analyzing different crystal properties. Three types of measurements are performed, which are ω-2θ scans, ω scans and two dimensional intensity distribution mapping in the reciprocal space, the so called reciprocal space maps (RSM).

In ω-scans the detector angle stays constant while the angle of incidence is varied by rocking the sample. Hence, this measurement is also called rocking curve. The scattering vector in reciprocal space is moved along the $Q_{||}$ direction as depicted in Fig. 11. The intensity distribution as a function of the incident angle contains information about the crystalline quality of the sample, more precisely the full width at half maximum (FWHM). A perfect crystal would give a sharp point in reciprocal space (see Fig. 11). If the sample consists of many small mosaic crystals which are tilted towards each other this lattice point is broadened in the $Q_{||}$ direction. Due to the tilt between the crystals the Bragg condition (Eq. (2.24)) is fulfilled for many different angles ω. For this measurement the detector must not be narrowed by a detection window, because this would decrease the measured FWHM by cutting off intensity. Rocking curves are performed using an open detector.

The ω-2θ scan is performed varying the angle of incidence ω and the detection angle 2θ in such a way that 2θ always is double the angle of incidence. In reciprocal space this is related to a movement along the $Q_{\perp}$ axis. This measurement is used to investigate e.g. material composition, the lattice constant, and thickness of thin layers or the lattice period of superlattices. The periodic structure of a superlattice results in oscillations of intensity as a function of 2θ depending on the widths of the superlattice layers.

A combination of ω and ω-2θ scans can be used to perform a two-dimensional intensity mapping of the reciprocal space. The whole area around a reciprocal lattice point is scanned as denoted in Fig. 11. A RSM is especially suitable for strain investigation in hetero epitaxy or the chemical composition of material alloys.

All HRXRD data presented in this work are performed using a Panalytical X'Pert diffractometer. For diffraction the copper $K_{\alpha 1}$ line with a wavelength of 1.54056 Å was used which was separated from the X-ray spectrum by a hybrid monochromator. The hybrid monochromator consists of a parallelizing mirror and a 4 bounce germanium (220) crystal monochromator which blocks the $K_{\alpha 2}$ line and reaches a beam divergence of $\Delta\theta$=47 arcsec. The sample is mounted on an Euler-cradle and can be manipulated in six axes. For detection of the diffracted beam the X'Celerator consisting of a diode array which allows fast measurements is used. A sketch of the diffractometer configuration is shown in Fig. 12.
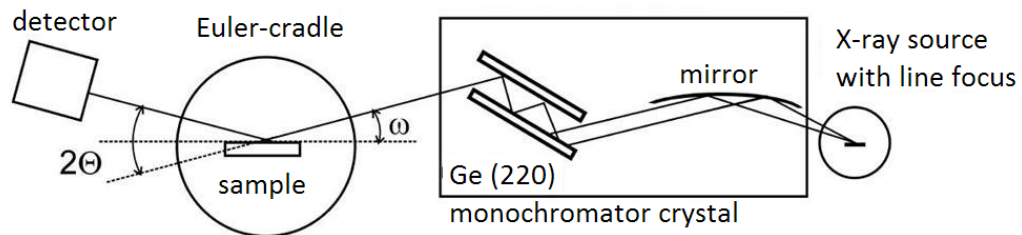
Fig. 12: Configuration of the X'Pert HRXRD diffractometer with X-ray source, hybrid monochromator, sample mounted on an Euler-cradle and the X'Celerator detector.

2.3.2   Transmission Electron Microscopy

Transmission electron microscopy (TEM) is a very powerful tool for the structural analysis of semiconductor samples. Similar to a scanning electron microscope (SEM) an electron beam is generated using a LaB_6 or a tungsten hairpin filament emitting electrons which are accelerated and focused on a sample using electron optics. In order to protect the filament from fusing and to avoid scattering of electrons with gas particles, the system has to be under high or even ultra high vacuum. Working pressures for TEM are in the order of 10^{-7} mbar or even lower. Typically a TEM consists of three different types of electron lenses (condenser, objective and projector lenses). The condenser lenses are used to form the primary electron beam. The objective lenses focus the transmitted beam, whilst the projector lenses expand the electron beam onto the optics part containing a fluorescence screen or a CCD imaging system. Typical acceleration voltages are in the range of 80 kV-300 kV. Depending on the specimen under study and the calibration of the electron optics, it is possible to obtain atomic size resolution. More detailed information about TEM can be found in [17]. A schematic drawing of a TEM system is shown in Fig. 13. The electron beam is focused on the sample. The transmitted beam is then displayed on a fluorescence screen where it can be observed using binoculars or an image can be recorded using a photo plate.
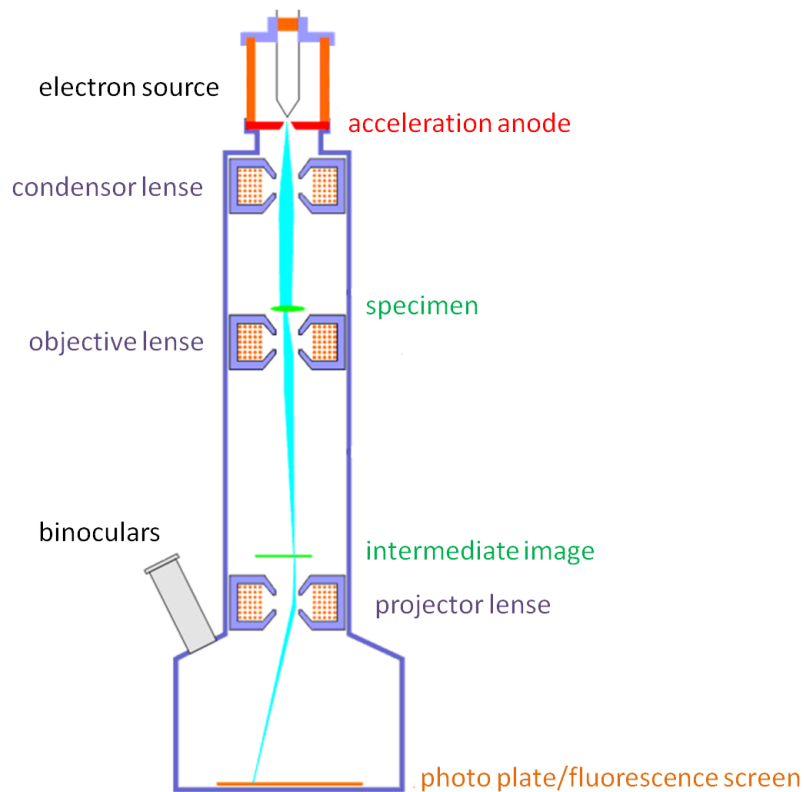
Fig. 13: Schematic design of a TEM.

The contrast of the TEM image depends on the operation mode. In this work, I will only shortly explain the used imaging method, the bright field imaging mode. Detailed information on operating methods and imaging of TEM can be found elsewhere [17]. The bright field image is formed by the direct beam electrons. To form the bright field image an objective aperture has to be inserted to select only the direct beam electrons (see Fig. 14). In a bright field image the contrast is related to absorption of electrons in the sample meaning that thicker regions or regions containing atoms with higher atomic number appear dark, while thin regions or light atoms appear bright. In this work GaN will appear dark whilst AlN will appear bright due to the difference in atomic weight between Ga (69.72 u) and Al (26.98 u). If instead scattered electrons are chosen to form the image the direct beam has to be excluded. The resulting image is called dark field image. Apart from the bright field and dark field imaging mode there are several other methods like diffraction contrast, electron energy loss spectroscopy or phase contrast imaging.
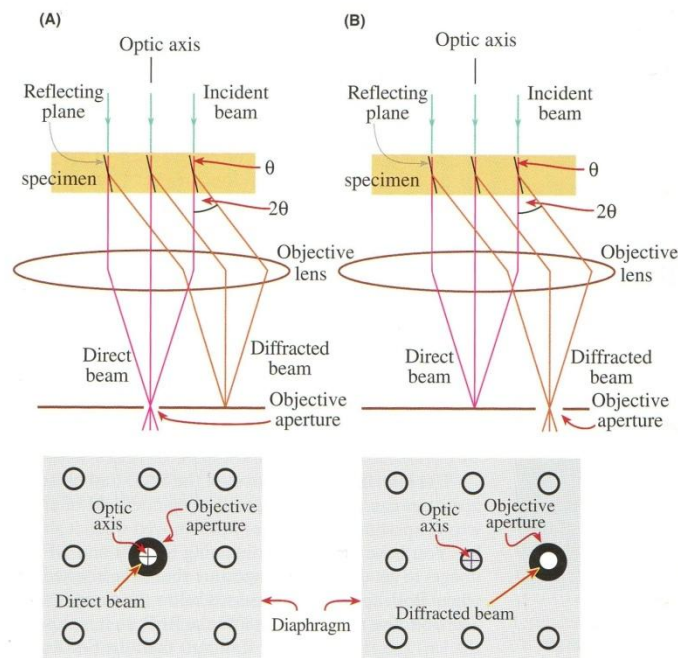
Fig. 14: Schematic position of an objective aperture to form a bright field image (A) or a dark field image (B) [17].

2.3.3 Photoluminescence Spectroscopy

Dealing with optoelectronic devices and materials it is essential to investigate the optical properties of a semiconductor. One way of optical characterization of a semiconductor is photoluminescence spectroscopy (PL). Luminescence spectroscopy in general is the energetic analysis of electromagnetic radiation emitted by a sample, in our case a semiconductor. To enable a semiconductor to emit light, electron hole pairs have to be generated which can recombine under emission of a photon. Hence, the electron has to be lifted from the valence band to the conduction band leaving a hole behind. Thus, the energy of the electromagnetic radiation is near the band gap energy of the semiconductor. This emission can be induced by several excitation sources. The limitation is that the energy of the excitation source has to be larger than the gap energy of the sample. For PL an optical excitation source e.g. a laser is used. Furthermore electrons in a scanning electron microscope can be used to generate electron hole pairs. This method is called cathodoluminescence spectroscopy (CL). CL is reasonable for materials with large band gaps like AlN, because the energy of the electrons is much larger than the band gap energy and is in the order of several keV.

In PL the sample is illuminated by laser light. The light generates electron hole pairs. After excitation the semiconductor is in a non-equilibrium state. To achieve thermal equilibrium the electron hole pairs have to recombine which in the case of a semiconductor may result in light emission. An excited electron has manifold ways to recombine which can be observed in PL. The main transitions I want to focus on are interband transition (IBT), free exciton transition (X), bound exciton transition (D^0, X /A^0, X) and donor acceptor transition (D^0, A^0). A schematic sketch of the possible transitions is shown in Fig. 15.
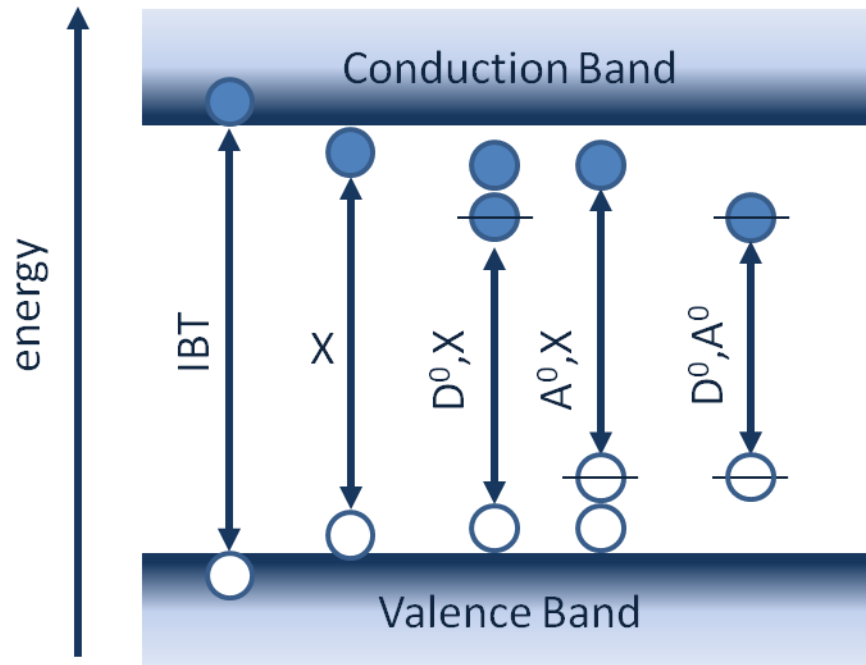
Fig. 15: Schematic diagram of possible recombination processes in a bulk semiconductor.

For PL spectroscopy I use a HeCd gas laser emitting at 325 nm with a maximum power of 35 mW. In the excitation path the laser passes a plasma filter eliminating plasma lines. The laser light is focused by a dielectric mirror onto the sample which is mounted in a closed cycle He cryostat reaching a minimum temperature of 13 K. The emitted light is analyzed by a Spec 270m monochromator in combination with a GaAs photomultiplier and a Hamamatsu C3866 photon counting unit. The emission spectrum is recorded by a PC. The maximum resolution of this setup is around 2 meV. A sketch of the PL setup is shown in Fig. 16.

For cathodoluminescence spectroscopy a ZEISS DSM 950 scanning electron microscope equipped with an Oxford Instruments CL302 system and a CF301 helium cooled cryostat is used. The setup reaches a minimum temperature of approximately 100 K. In this work only room temperature CL measurements are performed. The emitted light is collected by an elliptical half space collimator mirror and then coupled into a 0.15 m Princeton Instruments grating monochromator connected to a Peltier cooled 1P28 photomultiplier and a Hamamatsu C3866 photon counter. A schematic drawing of the CL setup is shown in Fig. 17.
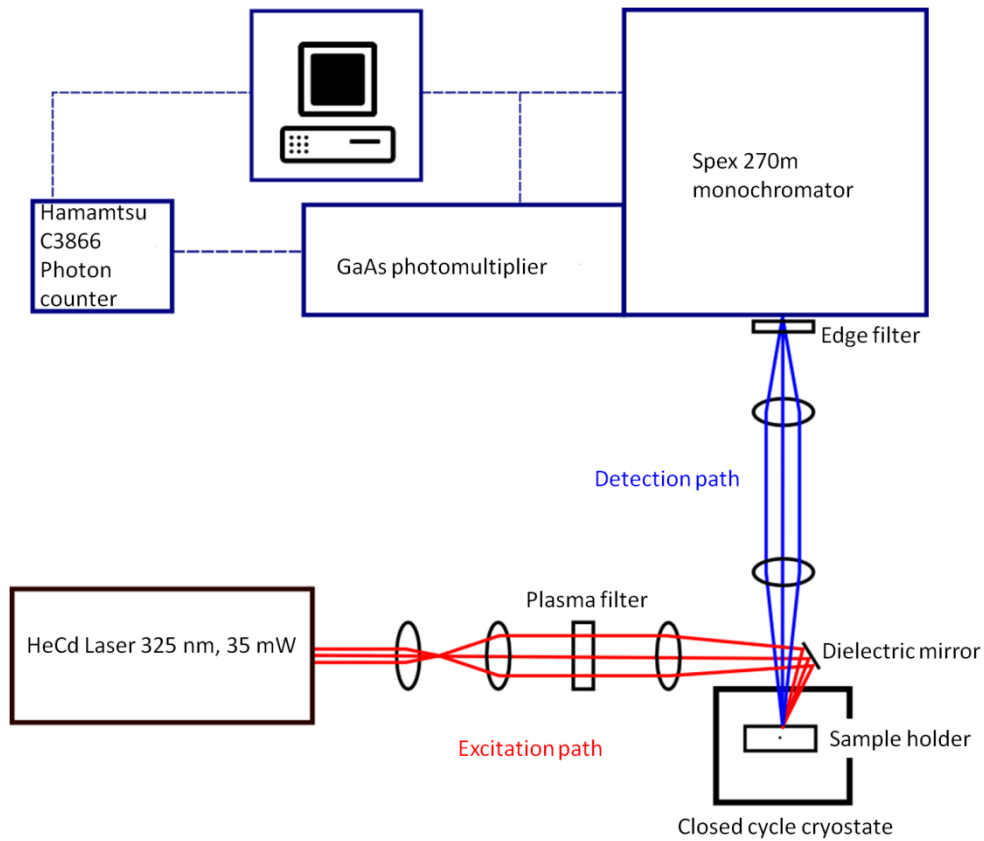
Fig. 16: Schematic drawing of the setup used for PL spectroscopy. For excitation a HeCd laser emitting at 325 nm is used. The sample luminescence is analyzed by a Spex 270m monchromator connected to a GaAs photomultiplier and a Hamamatsu photon counter. The luminescence spectrum is recorded by a PC.
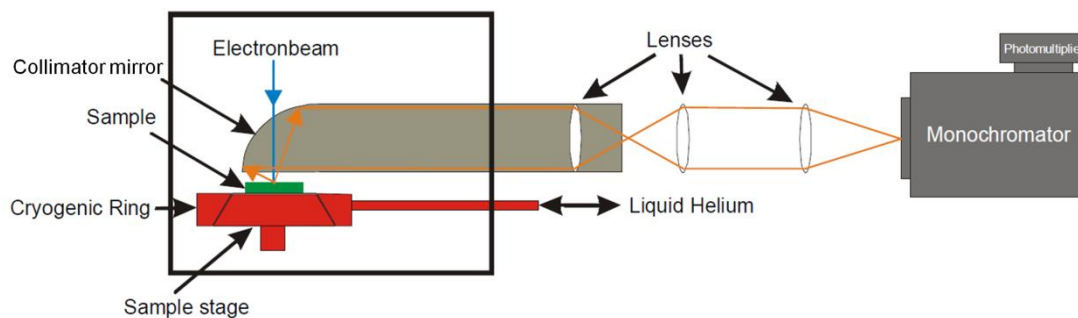
Fig. 17: Schematic drawing of the setup used for CL spectroscopy. The CL system is based on an Oxford Instruments CL302 light collector and CF helium cooling cryostat is installed in a Zeiss DSM 950 scanning electron microscope. The emitted light is collected by an elliptical half space collimator mirror and then coupled into a 0.15 m Princeton Instruments grating monochromator connected to a peltier cooled 1P28 photomultiplier and a Hamamatsu C3866 photon counter [18].

2.3.4 Infrared Absorption Spectroscopy

A very common way to measure infrared absorption of a sample is to use a Fourier transform infrared spectrometer (FTIR). In general, absorption spectroscopy is performed to get information about how much radiation is absorbed by a sample at each wavelength. One way to do this is to shine monochromatic light onto the sample and measure how much of the intensity is transmitted through the sample. This has to be repeated for each wavelength to obtain a whole spectrum. The great benefit of a FTIR is that data over a wide spectral range can be collected simultaneously. For excitation, a broadband infrared source containing the whole spectrum that has to be measured is used. The emitted light passes a Michelson interferometer before illuminating the sample. A schematic drawing of a FTIR is given in Fig. 18.
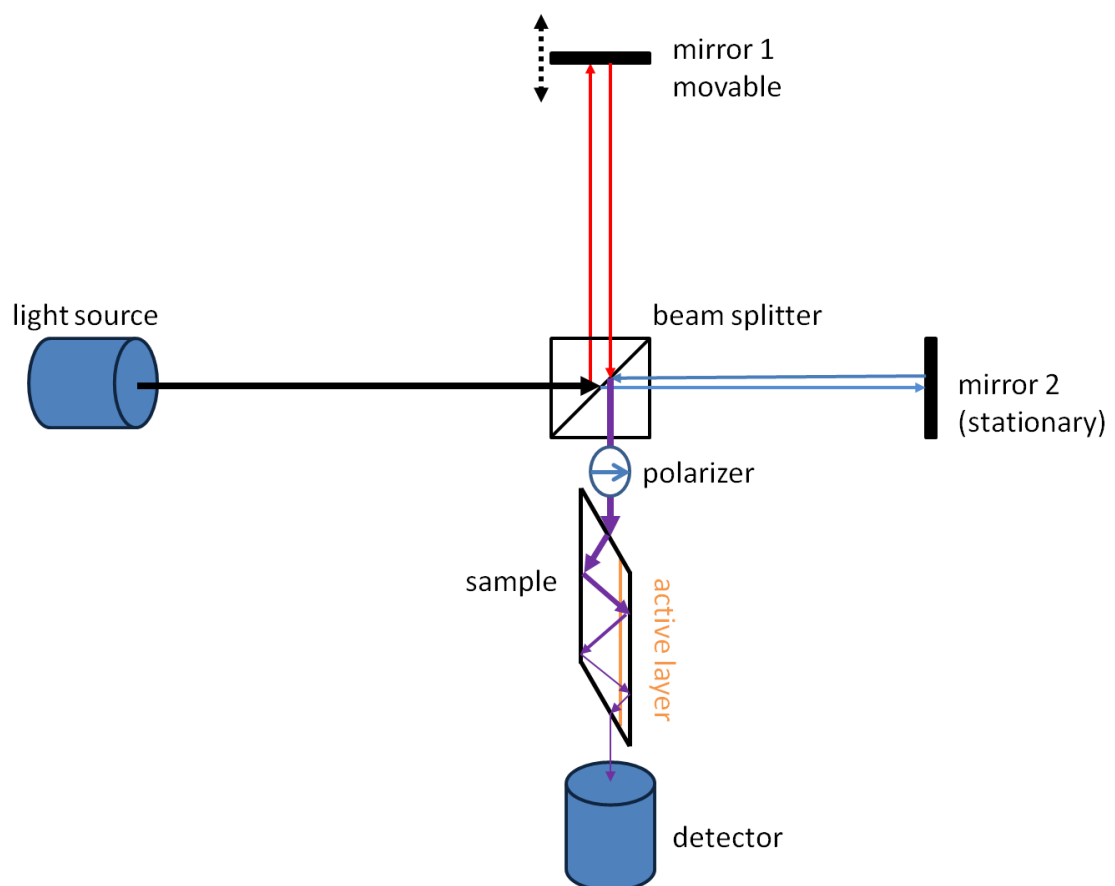
Fig. 18: Schematic drawing of the experimental setup for infrared absorption measurements.

The Michelson interferometer consists of a beam splitter and two mirrors. One mirror is fixed while the other can be moved. Depending on the position of the movable mirror, different path lengths for the two light beams behind the beam splitter can be adjusted resulting in different interference of the two beams. By moving the mirror over

a certain length an interferogram can be recorded. This interferogram is the mathematical equivalent of the spectrum and by Fourier transformation of the intensity of the interfering beam the absorption depending on the wavelength can be calculated. The Fourier transformation is eponymous for this experimental method. As mentioned in 2.1.1 only certain polarizations cause intersubband absorption. That is why our samples have to be processed into waveguides with 30° facets to allow the radiation to pass the active layer multiple times increasing the absorption. To perform polarization dependent measurements an additional polarizer has to be placed before the sample. This polarizer is used to measure the extinction for the case of TE- or TM-polarization.

2.4 Model Calculations

In this chapter I will introduce the different tools used for model calculations. For a better understanding of the experimental results calculations have to be performed and the theoretical values of layer thicknesses or transition energies have to be compared to measured values. In the following I present two tools I have used for theoretical calculations. The first tool is nextnano³ [14], which is used for transition energy calculations as well as I-V-characteristics of resonant tunneling devices. The second tool is MadMax [19] (massively accelerated dynamical multilayer analysis by X-ray diffraction) and is used for the calculation of X-ray diffraction profiles. From the calculated diffraction profiles strain conditions and layer thicknesses in SLs or MQWs can be obtained.

2.4.1 nextnano³

nextnano³ is a free of charge software for calculation of the electronic structure of many semiconductor devices like hetero-structures, quantum wells and nanostructures in one dimension (1D), two dimensions (2D) and even three dimensions (3D). The calculation of the electronic structure is done quantum mechanically. Furthermore, devices under bias can be simulated and even current densities can be calculated using a semi-classical concept of local Fermi levels calculated self-consistently. The equations to be solved are the Schrödinger-, Poisson- and the current continuity equation for electrons and holes.

For my work, I have only used one dimensional band structure and transition energy calculations based upon an effective mass model. Furthermore, I have performed current density calculations in resonant tunneling structures using the constant block reduction method (CBR) [20]. The set of material constants used for model calculations together with two exemplary input files for transition energy calculations as well as constant block reduction (CBR) I-V-characteristic calculations can be found in the appendix (6.1). In order to show how the program works, I will recapitulate results of two open-access input files downloaded from the nextnano³ homepage. For the calculations of my structures I have used these input files as a starting point and changed the parameters step by step. Fig. 19 shows the calculated band structure of a 10 nm GaN QW embedded in 20 nm $Al_{0.35}Ga_{0.65}N$ barriers. The input file these calculations are based on is called "1D_simple_GaAs_QW" and is accessible on the nextnano homepage (www.nextnano.de). The only changes I made in the input file are to replace GaAs by GaN and AlGaAs by AlGaN. Besides the conduction band edge (black

line), the squared wave functions of six electron states (e1-e6) are plotted. Five of the calculated states are localized in the QW region while the sixth state is slightly above the barrier conduction band edge and therefore not localized, that is why the e6 wave function is extended over the whole structure. The energy scale is referenced to the position of the Fermi energy which is located at 0 eV for undoped structures. From the energetic positions of the localized states intersubband transition energies can be calculated. Furthermore, nextnano³ can be used to calculate the transition probabilities and transition matrix elements.
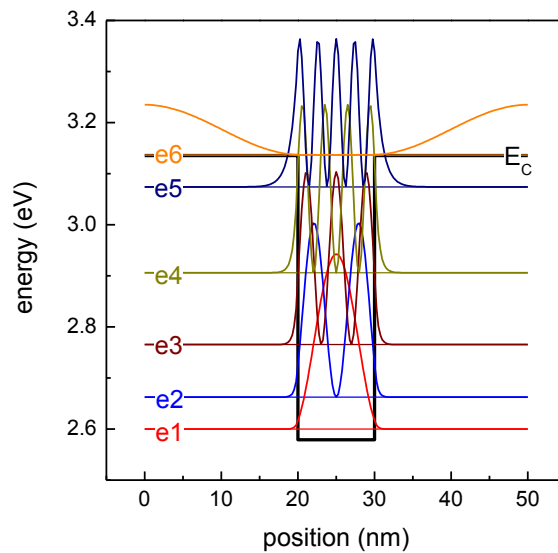
Fig. 19: Calculated conduction band structure of a 10 nm GaN QW embedded in 20 nm Al$_{0.35}$Ga$_{0.65}$N barriers. Five localized states (e1-e5) and one continuum state e6 is found.

Fig. 20 shows the calculated conduction band edge of an Al$_{0.3}$Ga$_{0.7}$N/GaN resonant tunneling structure with the energy resolved density of electrons in this structure for three different bias voltages. Part (a) of the diagram shows the unbiased structure, where the electron density is mostly localized in the doped GaN emitter and collector region next to the ohmic contacts. Part (b) of Fig. 20 shows the structure under resonance conditions. The band edge is bent strongly enough for the Fermi level being resonant with the localized state in the double barrier region resulting in a very high electron density in the QW. This is the point where the negative differential resistance occurs, because the electrons have a high probability of tunneling through the second barrier and can be collected at the second contact. If the bias is further increased this resonance vanishes and the electron density in the QW drops again. Using nextnano³ it is possible to calculate the current through such a resonant tunneling structure for each bias step. Fig. 21 shows the calculated current density versus applied bias voltage. A clear negative differential resistance can be observed consistent to the calculated

electron density. The used input file for these calculations can also be found on the nextnano homepage and is called "1D_RTD_CBR_I-V". Results of these calculations and a further detailed description of the constant block reduction (CBR) method can also be found in [20]. Again I replaced the GaAs by GaN, AlGaAs by AlGaN and I changed the thickness of the barriers from 3 nm to 2 nm.
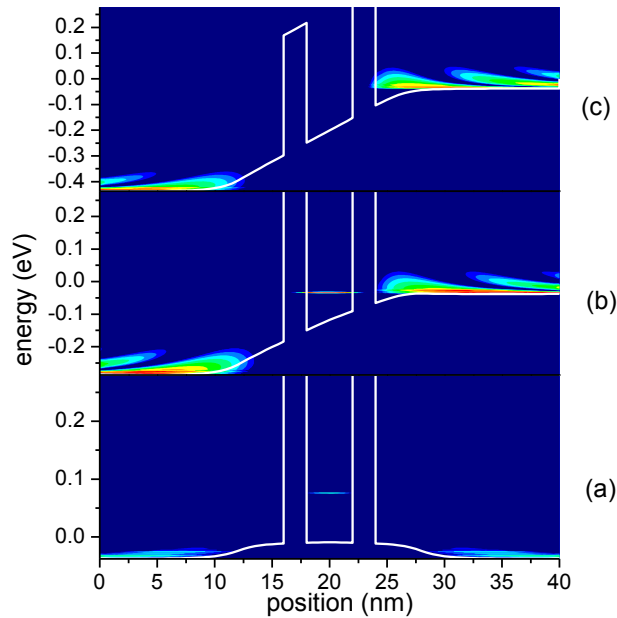
Fig. 20: Calculated conduction band structure of a GaN/Al$_{0.3}$Ga$_{0.7}$N resonant tunneling diode without bias (a) in resonance (b) and off resonance (c) with calculated electron density.
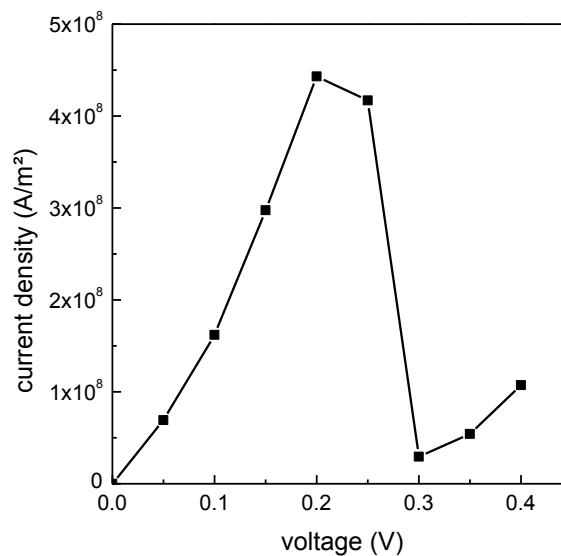
Fig. 21: Calculated current density versus bias voltage for the GaN/Al$_{0.3}$Ga$_{0.7}$N RTD structure. Clear NDR is observed around 0.25 V.

2.4.2 MadMax (Massively Accelerated Dynamical Multilayer Analysis by X-ray Diffraction)

MadMax [19] is a tool to calculate HRXRD diffraction profiles of multilayer systems. It is designed especially for III-V semiconductors and has actually implemented parameters for cubic nitrides. It can only be used to simulate diffraction profiles in co-planar diffraction geometry which is adequate for my diffraction measurements. MadMax can be used for arbitrary orientations as well as arbitrary reflections. Using the structure editor it is very easy to define even complicated superlattice structures. The materials can be selected in a drag down menu and for each layer individual thickness and strain can be defined.

In my work, I will only focus on [0 0 1] oriented substrates and the reflections (0 0 2) and (1 1 3). The substrate I am using for AlN/GaN growth (3C-SiC) is not yet implemented in the database of MadMax. Therefore a custom substrate has to be defined. I chose a substrate with zinc-blende crystal structure (GaAs) and defined a new lattice constant (0.43568 nm). Using this little trick produces appropriate results. In Fig. 22 the diffraction profile of a 600 nm thick GaN layer on 3C-SiC is shown. The black line shows experimental data while the other three lines show calculated data. For better comparability the experimental data is shifted so that the substrate peaks superpose each other. The difference between the calculated curves is due to different strain of the GaN layer. Although the GaN relaxes in the first few nanometers of growth some residual strain of the layer can be observed. The blue curve shows the diffraction profile of a fully relaxed layer, while the green and red curve are calculated assuming some residual strain in the order of 10 %. If fully relaxed means a relaxation of 1 green represents a value of 0.9 and red of 1.1 where 0.9 means compressive strain and 1.1 means tensile strain. The explanation of this result is that the GaN layer is under this residual strain because of different thermal expansion coefficients of GaN and SiC which lead to this residual strain after cooling down the sample from growth temperature. This effect can especially be observed in thick GaN layers.
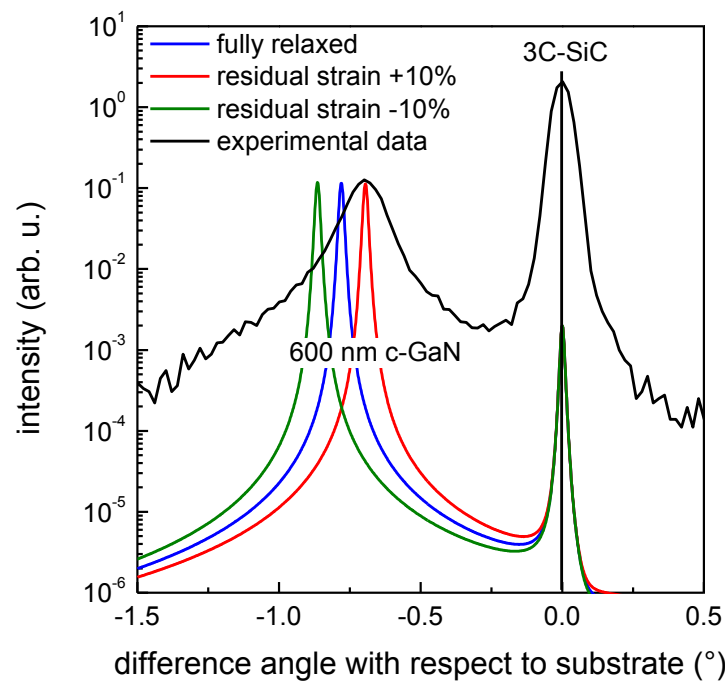
Fig. 22: Calculated HRXRD ω-2θ diffraction profile of the (002) reflection of 600 nm cubic GaN on 3C-SiC (001) for three different relaxation states in comparison to an experimental result. Angular position of measured data was shifted for the substrate peak to be at 0°.

In the following I want to show some results of different superlattices and how certain changes of the parameters influence the results. First, I want to show that is not only possible to obtain the lattice period of a SL structure by comparison of the experimental and calculated data, but also the thicknesses of the single layers. In Fig. 23 the calculated diffraction profiles of two different AlN/GaN SLs on 3C-SiC are plotted. Both SLs have the same SL period of 4 nm while the thicknesses of the single layers are slightly different. The difference in layer thickness is in the order of one monolayer (ML) (0.2 nm). Although the thickness variation is very low, a clear shift of the SL satellites is observed. Due to the constant lattice period the distance between the SL satellites remains constant. But all satellites are slightly shifted towards the substrate peak for the thicker AlN layer. AlN has a lattice constant very close to 3C-SiC that is why the SL satellites of the sample with a larger amount of AlN are shifted towards the theoretical lattice constant of AlN and thereby towards the substrate peak (see black line).

With the next diagram I want to show the effect of strain on the positions of the superlattice satellites. Fig. 24 shows the calculated ω-2θ diffraction profiles of two AlN/GaN superlattices on a 50 nm GaN buffer layer. The SL consists of 40 periods of 2.1 nm GaN and 1.5 nm AlN layers. The black curve shows the SL structure for fully relaxed GaN and fully strained AlN layers, which is often the situation in SLs grown on a

GaN buffer if the AlN volume fraction is much lower than GaN. If the AlN volume fraction is comparable to the amount of GaN, the superlattice starts to form its own equilibrium lattice constant. The red curve shows the case when both layers are 50% strained by the other layer. The substrate peak and the GaN buffer layer peak are still at exactly the same position while the SL peaks are strongly shifted.
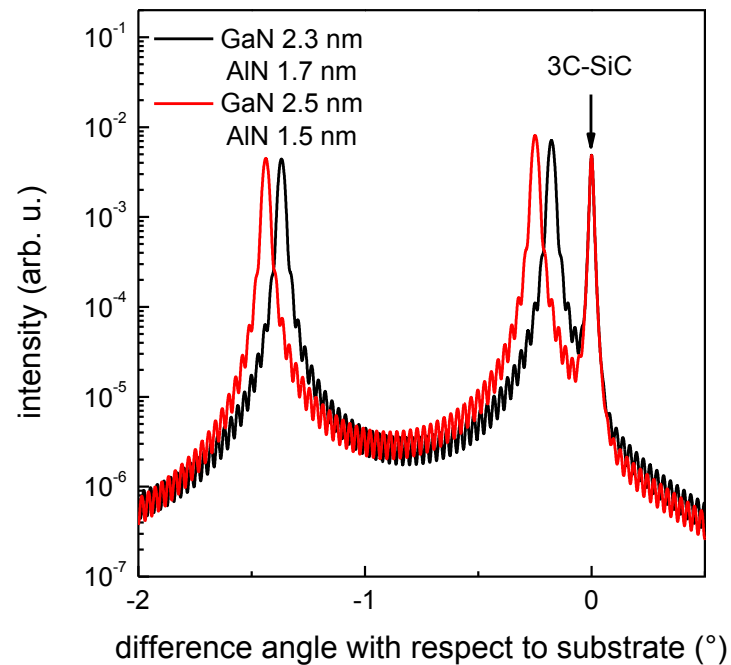
Fig. 23: Calculated ω-2θ diffraction pattern of (002) reflection of two different AlN/GaN superlattices with different layer thicknesses but equal lattice period.
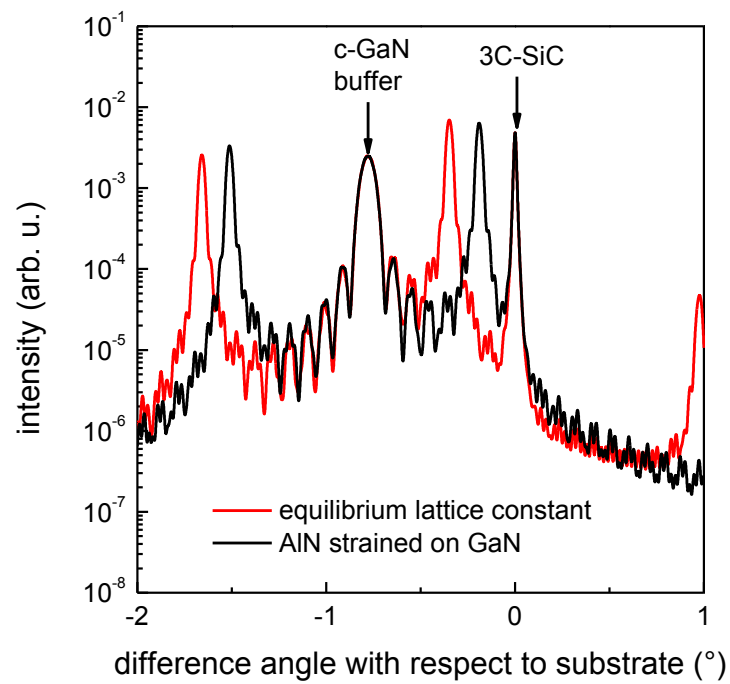
Fig. 24: Calculated ω-2θ diffraction pattern of (002) reflection of two different AlN/GaN superlattices with different state of relaxation. Black line shows diffraction pattern of a SL with GaN fully relaxed and AlN fully strained on GaN. Red line shows results for a SL forming an equilibrium lattice constant with GaN and AlN 50% relaxed.

In conclusion MadMax allows a very exact determination of the layer thicknesses and the strain conditions in a SL system. A good example for such a simulation can be seen in Fig. 29.

43

3 Device Applications for Cubic AlN/GaN Multi-Quantum-Wells and Superlattices

3.1 Quantum Well Infrared Photodetectors

A quantum well infrared photodetector (QWIP) is an optoelectronic device based on intersubband transitions in QWs or SLs. Depending on the band offset between barrier and QW material, the ISBT energy can be adjusted over a large spectral range. The radiation, that shall be detected, is absorbed in the QW lifting an electron from the occupied ground state (e1) to an excited state (e2). If the device is operated under a small bias, the excited electron is able to tunnel through the triangular potential barrier and can be detected as a small photocurrent at the collector. The schematic of this process is shown in Fig. 25. Due to the large band offset between cubic AlN and GaN this material is very interesting for this kind of application. The large band offset offers a tunability of the ISBT energy over a large spectral range covering the telecommunication range (1.55 μm) as well as the THz region. Furthermore, the relaxation time in Al(Ga)N/GaN is predicted to be 100 fs at 1.55 μm [21, 22], which is one order of magnitude shorter than in InGaAs MQWs [23]. Up to now a lot of research has been done towards QWIPs based on AlN/GaN superlattices [8, 24]. Intersubband absorption as well as photoresponse of AlN/GaN superlattices has been shown on free-standing 3C-SiC substrates [24] and on 3C-SiC on Si substrates [25]. The tunability of the transition energy from the near infrared to the THz region has been demonstrated as well [9].
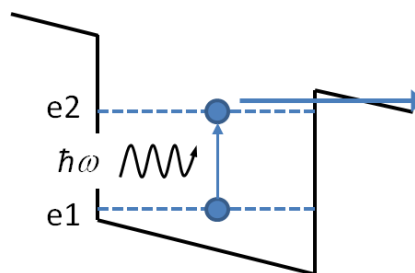
Fig. 25: Schematic conduction band profile of a QW under small bias voltage. Radiation is absorbed exciting an electron from ground state e1 to excited state e2 where it can tunnel through the thin barrier.

3.2 Resonant Tunneling Diodes

"The Resonant Tunnelling Diode (RTD), which utilises the electron-wave resonance occurring in double potential barriers, emerged as a pioneering device in this field in the middle of the 1970s. The idea of resonant tunnelling (RT) was first proposed by Tsu and Esaki in 1973 [26], shortly after Molecular Beam Epitaxy appeared in the research field of compound semiconductor crystal growth."[27]

As mentioned in the citation above, resonant tunnelling was proposed in 1973 and it has been shown in AlGaAs/GaAs by Chang, Esaki, and Tsu in 1974 [28]. In general the structure needed for resonant tunnelling experiments is not very complicated and can easily be realized using MBE. The starting point is an electron injection layer like a highly n-doped semiconductor with the Fermi level above the conduction band edge. The double barrier structure is formed by a QW embedded in two layers of a semiconductor with a larger band gap. The double barrier structure is followed by an electron collector layer (again a highly n-doped semiconductor). A schematic of such a RTD structure is given in Fig. 26. In our material system this can be realized by a GaN QW embedded in AlN or AlGaN barrier layers.
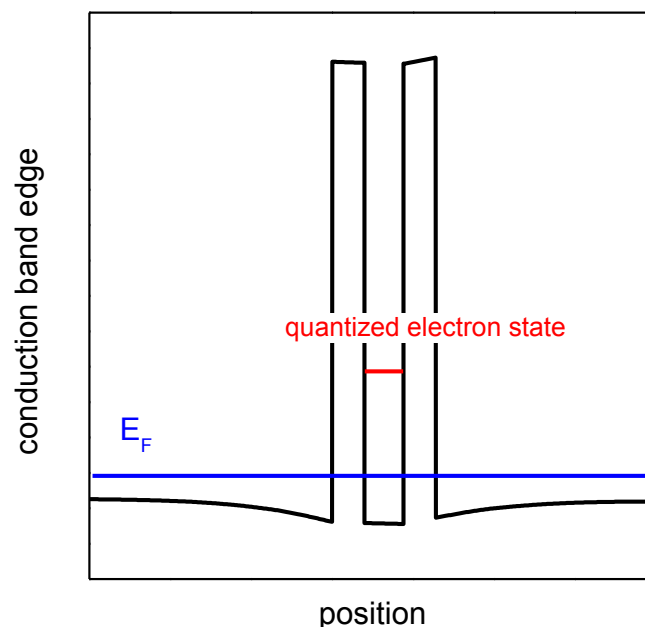
Fig. 26: Schematic of the band diagram of a RTD structure. The Fermi level is above the conduction band edge due to n-type doping but still below the quantized electron state.

By applying a bias voltage to this double barrier structure, the Fermi level can be brought into resonance with the quantized state by band bending. In this case, resonant

tunnelling occurs and the electrons can pass the barriers without appreciable resistance. The conduction band profile for four different bias states is shown in Fig. 27. The picture is taken from [27]. Part (a) shows the unbiased structure, (b) shows the structure at the threshold voltage where the Fermi level reaches the quantized state energy, (c) shows the resonance area while in (d) the off resonance state is shown.
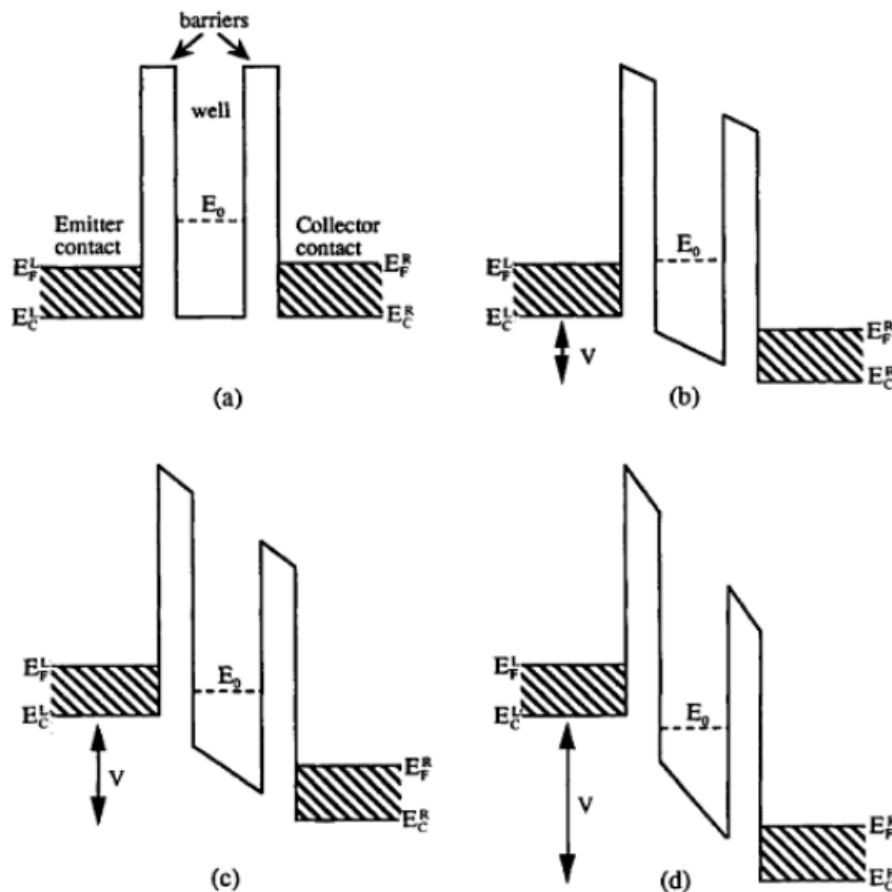
Fig. 27: "Conduction band profiles of a double barrier resonant tunneling diode at four different bias states: (a) zero bias, (b) threshold bias, (c) resonance, and (d) off resonance. Hatched regions represent the Fermi Sea in the emitter and collector layers. E_F^L and E_F^R are the local Fermi energies in the emitter and collector, and E_C^L and E_C^R are the energies of the conduction band edge in the emitter and collector."[27]

This can be seen in the I-V-characteristic of the device as a negative differential resistance. Resonant tunnelling is of great interest for two different research fields, it is an interesting feature for quantum transport physics as well as for device applications. In the case of my work I am interested in the current transport through thin barriers of Al(Ga)N as a milestone for future device applications and not the application of an RTD in general.

3.3 Quantum Fountain Lasers

In an optically pumped laser like a quantum fountain laser (QFL) selective optical excitation is used to promote electrons from the ground state to an excited state of the active QWs [29]. The operation of an optically pumped laser relies on the radiative transition of electrons between bound states of asymmetric coupled quantum wells (ACQW). The calculated conduction band profile of an appropriate ACQW system of cubic III-nitrides is shown in Fig. 28. Population of the ground state e1 can be achieved by Si-doping. The optical pumping takes place from state e1 to the second excited state e3 while emission occurs from e3 to the second excited state e2 (transitions indicated by arrows in Fig. 28). To achieve population inversion between e3 and e2 the lifetime of electrons in state e2 has to be shorter than the scattering time between e3 and e2 [30]. Fast depopulation of e2 state can be achieved by resonant phonon scattering if the e1-e2 energy separation is adjusted to be exactly the LO phonon energy (92 meV in c-GaN [31]). In chapter 4.4 I will present first experimental results on the growth and characterization of cubic III-nitride ACQWs showing the potential of III-nitrides for future optically pumped laser devices.
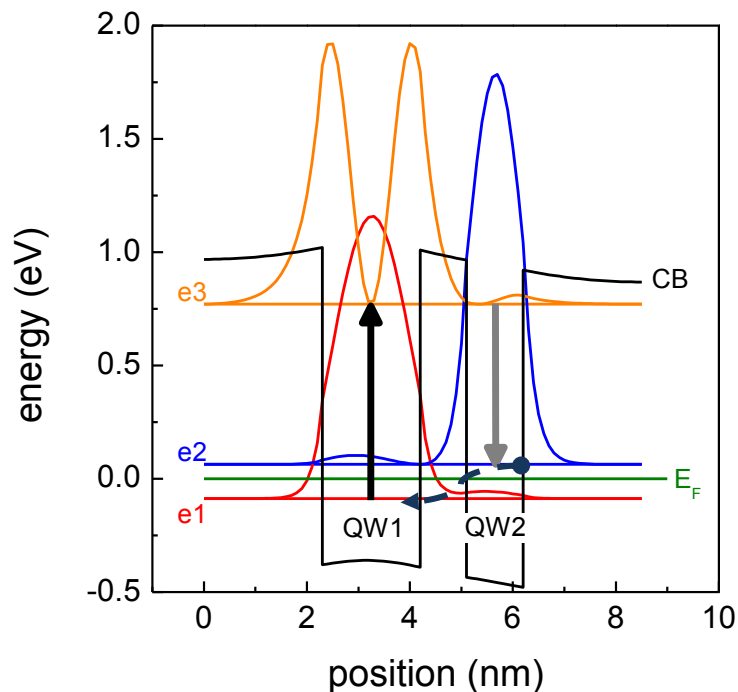
Fig. 28: Calculated conduction band edge for a pair of asymmetric coupled quantum wells (black line) and quantized states including squared wave functions. Absorption is indicated by the black and emission by the gray arrow. The phonon assisted depopulation is indicated by the dashed blue arrow.

4 Experimental Results

4.1 Tunability of Intersubband Transition Energy

In this chapter I will outline the possibilities of tuning the ISBT energy of III-nitride superlattice systems. Due to the large band offset between GaN and AlN this material system is suitable for applications in the near infrared and telecommunication range, but can as well be tuned to much lower ISBT energies by increasing the QW thickness. Moreover, by lowering the barrier height it can be tuned to the far infrared or THz spectral range. The barrier height can be decreased by fabricating ternary alloys of AlGaN with low Al content. During this work I achieved the largest ISBT energy as well as the lowest ISBT energy measured in III-nitrides up to now. The absorption wavelength is tuned from 1.4 μm (0.9 eV) to 63 μm (0.02 eV or 4.8 THz) [9].

First, I want to show some results on ISBT absorption in the near infrared range which is especially interesting for optical telecommunication due to the damping minima of glass fibers around 0.8 eV and corresponding 1.55 μm wavelength. The samples I want to present in this part consist of cubic AlN/GaN superlattices. The GaN QW thickness as well as the AlN barrier thickness is varied to shift the ISBT energy. Two series of samples were fabricated. Samples of series A consist of 40 period SLs. The AlN barrier thickness was 3.0 nm, and GaN QW thickness was varied from 1.8 to 5.0 nm. The cap layer was 7 nm thick. The growth was controlled by in situ reflection high energy electron diffraction (RHEED). The GaN layers were grown below one monolayer (ML) Ga coverage, which was found to be the optimal growth condition for cubic GaN, while the AlN layers were grown under N-rich conditions. The growth of the superlattice was interrupted after each layer to evaporate excess metal from the surface. The thicknesses of the AlN layers were controlled by RHEED-intensity oscillations while the GaN growth rate was estimated from AlGaN growth oscillations and thickness measurements on the reference sample. The growth rates for AlN and GaN were 0.19 and 0.18 ML/s, respectively. The QWs are n-doped with Si in order to populate the ground electronic state. The QW thickness is varied in order to tune the ISB fundamental e1–e2 transition energy.

4.1.1 Structural Properties

The QW and barrier thicknesses and the doping level are summarized in Table 1. The structural quality of the Al(Ga)N/GaN superlattices was assessed by X-ray diffraction. From the positions of additional satellites in the ω-2θ scans of the symmetrical (002) reflection, the lattice period of the superlattice structures was inferred. In addition, simulations for the X-ray measurements were performed using a dynamical scattering theory [19]. Using X-ray simulations, not only the lattice parameter, but also the thicknesses of the individual layers can be determined. Good agreement between experimental and calculated data can be achieved only by assuming the correct thicknesses for the QW and barrier layers. Fig. 29 shows an example of a ω-2θ scan of sample A2 with the related simulation. Good agreement between experiment and simulation is found for 3.1 nm GaN and 3 nm AlN considering a partial relaxation of AlN (about 20 %). In summary, the layer thicknesses deduced from X-ray diffraction for all samples are in good agreement with the nominal ones. The calculated diffraction profile is much narrower than the experimental one, because there is no broadening due to defects or mosaic crystals included in the calculation.

Table 1: Structural properties of the superlattices obtained from HRXRD measurements and simulations.

Sample	d_{GaN} (nm)	$d_{barrier}$ (nm)	Al-Content (%)
A1	5.0	3.0	100
A2	3.0	3.0	100
A3	1.8	3.0	100
B	12	15	5
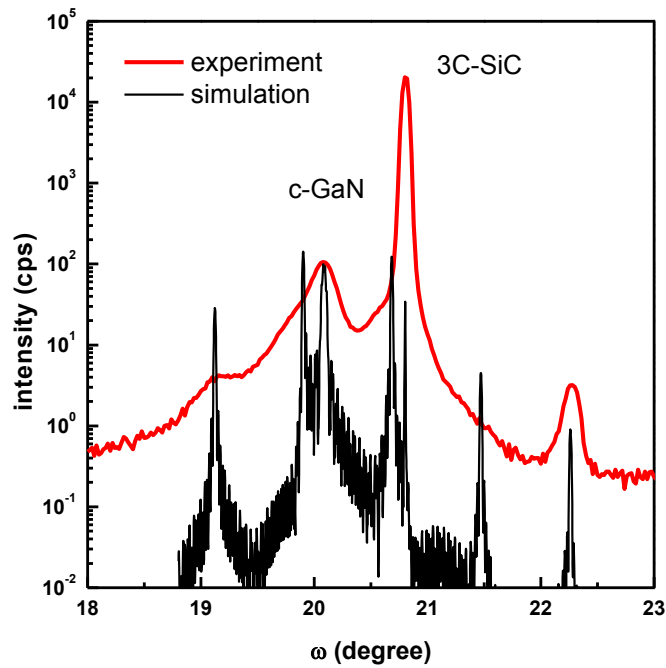
Fig. 29: Experimental data of an ω-2θ scan on sample A2 (red curve) compared to a simulated intensity distribution of a AlN/GaN superlattice (black curve). Clear compliance in the position of the SL satellites with experimental data is found.

In addition, the strain in the superlattice samples was investigated by reciprocal space maps of the asymmetrical (113) reflection. For samples A1, A2, and A3 I find that the AlN layers are not fully strained on GaN. From the position of the superlattice reflections I conclude that the superlattice structure has formed an average lattice constant between GaN and AlN, meaning that the AlN layers are partially relaxed while the GaN is partially strained. In Fig. 30 the (113) RSM of sample A2 is shown. Besides the experimental data (grey contours) the theoretical positions of cubic GaN, relaxed cubic AlN and cubic AlN strained on cubic GaN are marked with red squares. The experimental value of $q_{||}$ of the SL satellites (SL -1 and SL +1) is between the theoretical values of c-GaN and c-AlN, which is an indicator for the strain status of the layers as mentioned above.
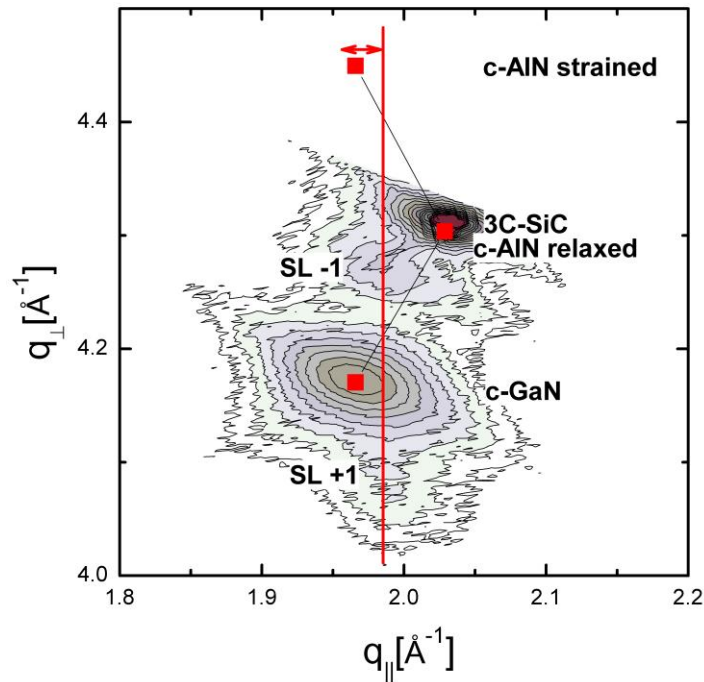
Fig. 30: Typical reciprocal space map of the (113) reflection for sample A2. A clear difference in relaxation is found. Partial relaxation is found for series B highlighted by the arrow. SL satellites are slightly shifted towards relaxed AlN position.

4.1.2 Infrared Spectral Range

All infrared absorption measurements were performed in cooperation with the group of Prof. Julien at the university Paris-Sud. For ISB absorption measurements, the samples are polished in multipass waveguide geometry with parallel facets tilted by 30° with respect to the substrate plane. The 30° angle is chosen in order to avoid the total internal reflection on the Si/SiC interface ($\theta_{critical} \sim 48°$) and to maximize the interaction of the electromagnetic field with the dipole of the ISB transition (which is oriented along the growth axis). The sample length corresponds to ~14 passes through the active region. Infrared absorption measurements are performed at room temperature using a Fourier transform infrared spectrometer. A typical transmission spectrum for TM- (p-) and TE- (s-) polarized light is shown in the inset of Fig. 31. The spectrum is normalized by the transmission of a reference sample (600-nm-thick cubic GaN epilayer on SiC on silicon). The oscillations observed in the spectrum arise from Fabry-Perot interferences in the 10-µm-thick SiC layer. The high-energy cutoff corresponds to the absorption of the Si substrate whereas the low-energy transmission drop at 0.21 eV corresponds to the two-phonon absorption of the SiC template [32]. Absorption peaked at 0.46 eV is observed for TM-polarized light. The TM polarization is a signature of an ISB resonance. Fig. 31 displays the ISB absorption spectra of samples A1, A2, and A3 together with the

corresponding Gaussian fits. The spectra are corrected for the baseline and normalized by the number of passes through the active region. The absorptions are peaked at λ=4.1, 2.7, and 1.4 μm for samples A1, A2, and A3, respectively. The broadening of the ISB absorption in the present cubic QW samples is larger than the values typically observed in their hexagonal counterparts. For example, for sample A1 the full width at half maximum (FWHM) is 0.17 eV, which is slightly higher than the typical broadening observed for hexagonal AlN/GaN QWs with absorption in the same spectral range (typically FWHM = 0.06 – 0.1 eV in doped QWs [33, 34] and 0.04 eV in undoped samples [35]). It should also be noted that for cubic QWs the ISB absorption resonance can be well fitted by a Gaussian function contrary to the wurtzite QWs where the absorption follows a Lorentzian or multi-Lorentzian shape [34]. This suggests that the broadening of the ISB transitions in cubic QWs originates from thickness fluctuations and interface roughness, as is the case for GaAs/AlGaAs QWs [36].
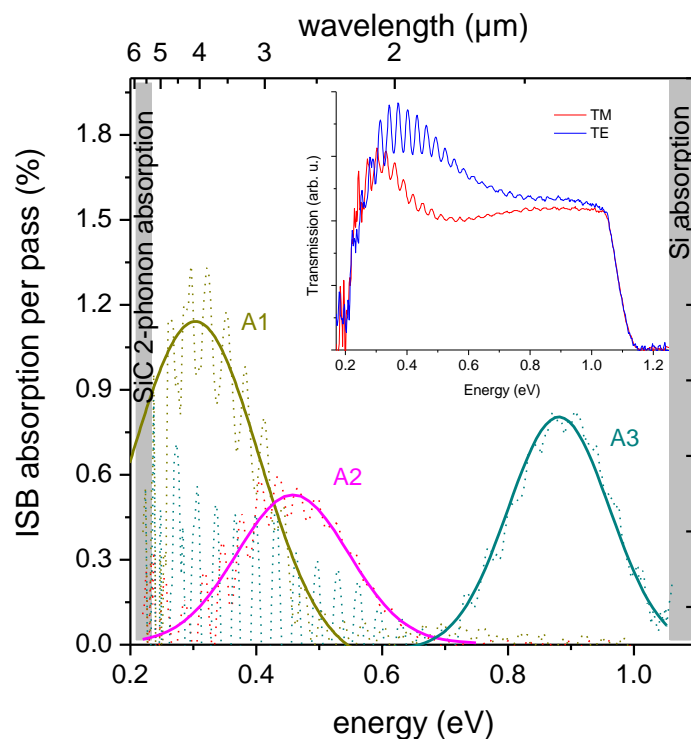
Fig. 31: Intersubband absorption as function of energy for series A. Experimental data is fitted by a Gaussian function. The transition energy is tuned from 0.88 eV to 0.3 eV. The inset shows an exemplary transmission spectrum for TE and TM polarized light. Clear polarization dependent absorption is found.

4.1.3 Terahertz Spectral Range

The transmission measurements in the THz spectral region were performed at a temperature of 4.7 K in a Bruker Fourier transform infrared spectrometer equipped with a glow-bar source and a liquid-helium-cooled Si bolometer. The sample was cut into two pieces of the same length. Both pieces, after polishing the facets at a 30° angle, were placed face to face under mechanical pressure and mounted on the cold finger of a liquid-helium-cooled cryostat. This configuration allows enhancing the light transmission by doubling the surface of the input facet. Moreover, it is known that the transverse electric field is weak in the λ/n vicinity of the semiconductor-air interface (where λ is the wavelength and n is the semiconductor refractive index) because of the zero transverse electric-field boundary condition for TM-polarized light [5]. Therefore, the standard multipass waveguide configuration used for the near-infrared measurements is not optimal for the far-infrared spectral range for which λ/n is very large as compared to the active region thickness. On the contrary, placing the active QWs face to face provides a good coupling of the TM polarized THz radiation with the ISB transitions. Two pieces of a 600-nm-thick cubic GaN epilayer on a SiC-on-silicon (001) template with approximately the same length placed face to face were used as a reference. Fig. 32 shows the transmission spectrum of sample B for TM- and TE-polarized light. The transmission of the sample has been normalized to 1 at low energies. Sample B exhibits an absorption peaked around 20 meV (5 THz) only for TM-polarized light, which is a clear signature of its ISBT origin. The three polarization independent absorption resonances between 30 and 40 meV are related to the SiC-on-Si substrate. They appear only at low temperatures and can be tentatively attributed to impurity absorption in SiC (shallow nitrogen donor absorption [37]). The FWHM of the ISB absorption is 9 meV, which corresponds to a relative broadening factor λ/λ of 45%. This rather large broadening could be attributed to the fluctuation of the QW thickness and to the electron-impurity and electron-electron scattering.
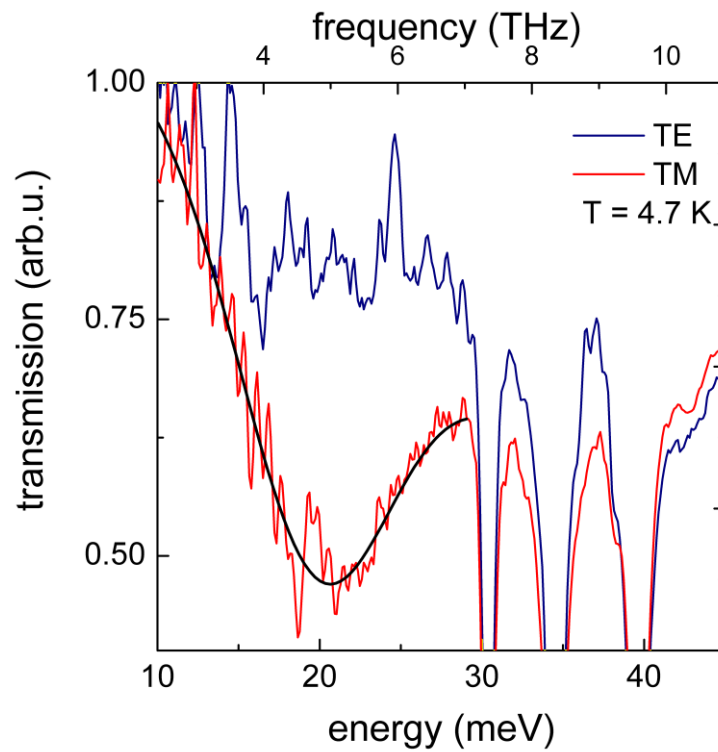
Fig. 32: Low temperature transmission as a function of energy for sample B. Clear absorption for TM-polarized light around 20 meV corresponding to a frequency of 4.8 THz.

4.1.4 Conclusions

In conclusion, an experimental study of the ISB transitions in Al(Ga)N/GaN cubic quantum wells has been performed. The ISB absorption wavelength could be tuned from 1.4 µm (telecommunication range) to 63 µm (THz frequency range). To the best of my knowledge, these values correspond, respectively, to the shortest and the longest ISB wavelength achieved to date in this material system. The observation of the ISB absorption at THz frequencies in GaN/Al$_{0.05}$Ga$_{0.95}$N QWs opens prospects for the future development of quantum cascade lasers in this material system.

56

4.2 Band Offset in AlN/GaN Superlattices

In the following, I will describe how I investigated the band-offset in AlN/GaN superlattices by intersubband and interband spectroscopy. Experimental results will be compared to model calculations and *ab-initio* calculations. The *ab-initio* calculations were performed in cooperation with the theoretical physics group of Prof. W.G. Schmidt in Paderborn. On the one hand, the conduction band offset (CBO) is determined from the comparison of the measured transition energies with model calculations within the effective mass approximation. On the other hand, the valence band offset (VBO) and the CBO are accurately simulated by calculating many-body corrections within the GW approximation on top of hybrid-functional density functional theory calculations. Thus, a CBO of (1.4 ± 0.1) eV and a VBO of (0.5 ± 0.1) eV is obtained as a result of both approaches.

One of the most crucial parameters that determines the physics in heterostructures and is needed for the optimization and design of optoelectronic devices, based on, e.g., quantum wells, is the electronic band alignment at the interface between two semiconductors. More precisely, I am interested in the valence and conduction band offsets, which reflect how the band-gap difference of the involved semiconductor materials is portioned between the discontinuities of the occupied and unoccupied energy bands. Due to their technological importance, the band offsets between various semiconductor alloys have been subject to extensive experimental and computational studies. Today, group III-nitrides are the material of choice for manifold device applications like light emitting diodes (LED), laser diodes or field-effect transistors. Based on the large band discontinuity between AlN, GaN and InN, novel nitride-devices based on intersubband transitions (ISBT), like quantum well infrared photodetectors (QWIPs) or quantum cascade lasers (QCLs) operating at telecommunication wavelengths are proposed [38]. State of the art group III-nitrides crystallize in the stable wurtzite structure. This hexagonal phase is characterized by strong internal piezoelectric and pyroelectric fields along the c-axis which are undesirable for many optoelectronic applications. In multi-quantum-wells or superlattices these internal fields complicate the design and limit the tunability of intersubband transition energies. In polar group III-nitride quantum wells (QW), the transition energy is observed to be almost independent of the well width for thick wells due to the confinement of carriers in a triangular potential caused by the internal field. The growth of non-polar and semi-polar nitrides has found increasing interest in the last years to avoid these strong internal fields. In these non-polar (semi-polar) nitrides the c-axis is orthogonal (inclined) to the

growth direction, thus eliminating the field effects in growth direction. The absence of these internal fields leads to an increased transition probability and therefore to enhanced luminescence intensity and reduced shift in emission wavelength in LEDs. However, the electrical, optical and structural properties show strong lateral anisotropy since the polarization field is now in the plane of growth. Furthermore, due to the large anisotropic biaxial stress relaxation and cracking of AlGaN in one direction is observed. An alternative way to fabricate group III-nitrides without spontaneous polarization fields is the growth of meta-stable non-polar cubic group III-nitrides. Zinc-blende GaN, InN and AlN epilayers and, just recently, free standing GaN substrates have been successfully synthesized using plasma assisted molecular beam epitaxy (PA-MBE) [1, 2]. Especially the determination of optimal growth conditions for non-polar cubic GaN [3] and AlN [4] has pushed the development of electronic and optoelectronic devices like hetero-junction field effect transistors [6], resonant tunneling diodes [7] and quantum well infrared photodetectors [8] based on zinc-blende group III-nitrides. Furthermore, the tunability of intersubband transitions from the mid to the far infrared region in cubic AlN/GaN superlattices has been shown [9]. As far as I know, the band offset has not been measured for the cubic AlN/GaN system up to now. Intersubband transitions give direct access to the conduction band offset. The ISBT energy for a fixed quantum well structure depends only on the barrier height or the conduction band offset between well and barrier material. Hence, the conduction band offset can be used as a fitting parameter in model calculations of intersubband transition energies based on an effective mass model.

The samples presented here were grown by plasma-assisted molecular beam epitaxy (MBE) on 10 μm thick 3C-SiC substrates on top of Si (100) (NovaSiC). Two series of samples were fabricated. Samples of series A consist of a 100 nm c-GaN buffer followed by a 40 period AlN/GaN superlattice (SL). The active region is capped by a 7 nm GaN layer. The AlN barrier thickness was 3.0 nm and GaN QW thickness was varied from 1.8 nm to 5.0 nm. Another series of samples (series C) consists of 100 nm c-GaN buffer followed by a 20-period AlN/GaN SL. The active region is capped by a 100 nm GaN layer. The AlN thickness varied between 1.3 nm and 1.7 nm, and the GaN QW thickness varied between 2.0 and 2.5 nm. Growth rates of the different layers were observed in-situ by reflection high energy electron diffraction (RHEED) intensity oscillations. The strain of the samples was determined using high resolution X-ray diffraction (HRXRD).The thicknesses of the single layers were verified by simulations of HRXRD data based on dynamical scattering theory (MadMax) [19]. Intersubband spectroscopy is performed with a Fourier transform infrared spectrometer (FTIR). Two opposite facets of the

samples were optically polished at an angle of 30° in order to allow multiple passes in the active layers when irradiating the input facet at normal incidence. Interband spectroscopy is performed using a HeCd laser (325 nm) as excitation source. A Spex 270m monochromator combined with a GaAs photomultiplier and a Hamamatsu C3866 photon counter was used to detect emitted light from the superlattice samples.

4.2.1 Structural Properties

In the following paragraphs the results of structural and optical characterizations and model calculations are summarized. The structural properties are characterized in the first subsection. In the second subsection the results of intersubband- and interband spectroscopy are depicted. A detailed description of the model calculation results is given in the third subsection. The HRXRD reciprocal space maps (RSM) of the asymmetric (113) reflection of samples C3 (left) and A2 (right) were already shown in Fig. 30. Both RSMs reveal two superlattice satellites, the reflections of the substrate and the buffer- and cap layer. As can be seen in the left side diagram the superlattice satellites have the same $q_{||}$ as the c-GaN. I conclude that the superlattices are pseudomorphically grown on the c-GaN buffer for series C resulting in strained AlN barriers. The AlN layers are tensile strained to the GaN buffer due to the smaller lattice parameter of AlN with respect to GaN. As a result of the tensile strain, a reduction of the band gap energy of the AlN of about 0.2 eV to 5.1 eV (see equation (4.1)) is found. The right diagram shows that the superlattice satellites do not have the same $q_{||}$ as the c-GaN. Thus I conclude that the SL is partially relaxed (max. 30 %) due to the higher total volume fraction of AlN for series A. This partial relaxation results in an additional modification of the band gap energies of quantum well and barrier. The modified band gaps are 3.23 eV for GaN and 5.15 eV for AlN. These small modifications result in a change in ISB transition energy, for example less than 10 meV for sample A3 and are therefore neglected for further considerations. The structural properties of the samples are summarized in Table 2.
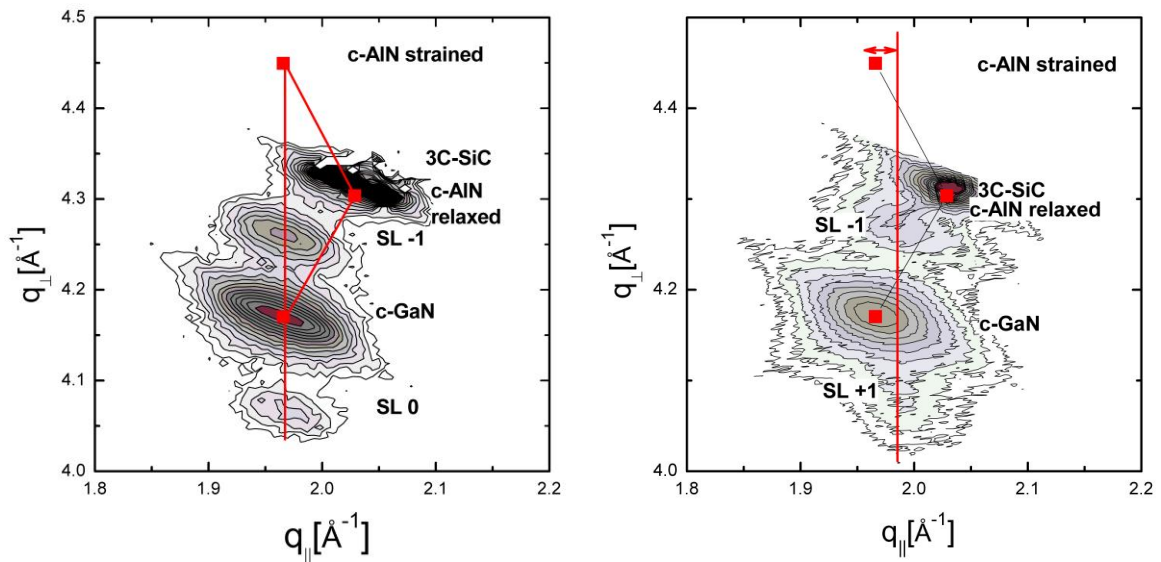
Fig. 33: Typical reciprocal space maps of the (113) reflection for sample C3 (left hand) and A2 (right hand). A clear difference in relaxation is found. Series A SL is fully strained on the GaN buffer while a partial relaxation is found for series A highlighted by the arrow. SL satellites are slightly shifted towards relaxed AlN position.

Table 2: Structural properties of the superlattices obtained from HRXRD measurements and simulations.

Sample	d_{GaN} (nm)	d_{AlN} (nm)
A1	5.0	3.0
A2	3.0	3.0
A3	1.8	3.0
C1	2.0	1.3
C2	2.2	1.3
C3	2.5	1.7

4.2.2 Optical Properties

Fig. 34 shows normalized intersubband absorption spectra of all samples under TM-polarized light. The spectra are fitted by Gaussian functions. The absorption spectra for series C are taken from [65]. Most of the spectra show oscillations from Fabry-Perot interferences in the 10 μm thick 3C-SiC layer. The absence of these oscillations for samples C1 and C3 is explained by larger interface roughness between 3C-SiC and Si. As shown in Fig. 34, all samples exhibit intersubband absorption with peak energy in the range 0.3 to 0.9 eV. Furthermore the absorption spectra of series A show a smaller full width at half maximum (FWHM) than series C. This may be explained by the thicker AlN barriers. AlN shows a tendency to smaller roughness and smooth interfaces [4].
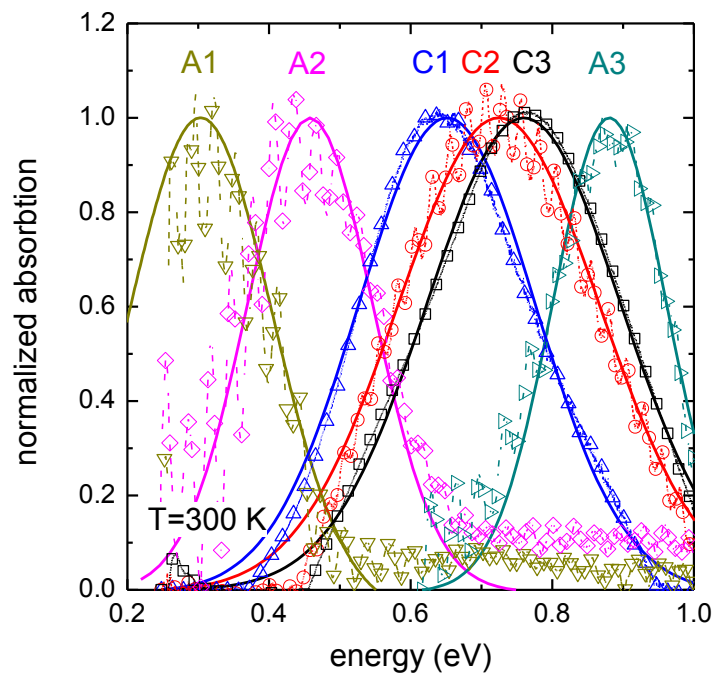
Fig. 34: Normalized room temperature intersubband absorption spectra (symbols) fitted with Gaussian functions (lines).

The measured photoluminescence spectra of our samples are plotted in Fig. 35. From these spectra transition energies of interband transitions from the lowest conduction band level to the highest valence band level are obtained. The FWHM of the PL lines is increasing with increasing PL transition energy, since the effect of monolayer thickness fluctuations is increasing with decreasing well width.
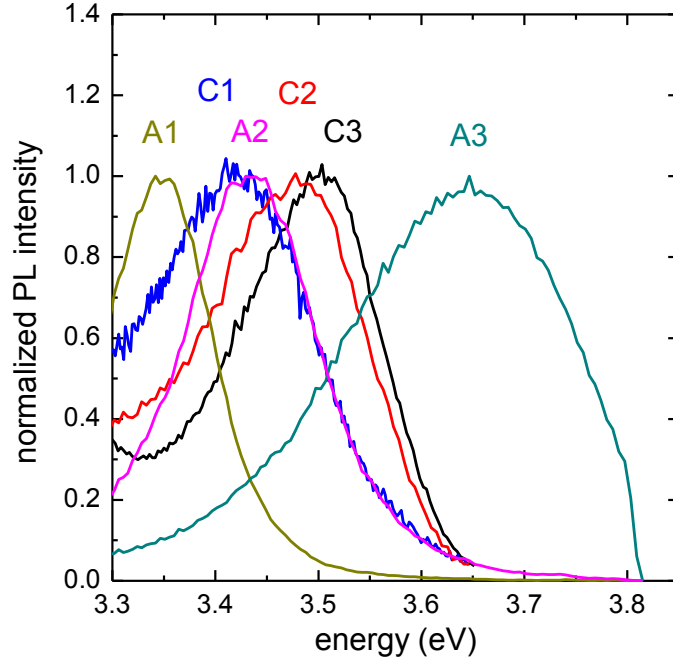
Fig. 35: Normalized room temperature PL spectra

4.2.3 Model Calculations

Model calculations based on a single band effective mass model with periodic boundary conditions using nextnano[3] [13] are performed to obtain theoretical intersubband transition energies. More detailed information on nextnano[3] can be found in [39] and [14]. A modification of the band gap due to strain can be calculated using Eq. (4.1) and Eq. (4.2).

$$E_{gap,strained} = E_{gap,0} + 2a_c \left(1 - \frac{c_{12}}{c_{11}}\right) \varepsilon_{xx} \tag{4.1}$$

$$\varepsilon_{xx} = \left(\frac{a_{GaN}}{a_{AlN}} - 1\right) \tag{4.2}$$

Here $E_{gap,strained}$, is the band gap energy of the strained layer, $E_{gap,0}$ is the band gap energy of the bulk material, a_c is the deformation potential, c_{11} and c_{12} are the elastic constants. ε_{xx} is the misfit between GaN and AlN with the lattice parameters a_{AlN} and a_{GaN}. For all QW samples an enhancement of effective masses due to non parabolicity effects is also taken into account. It has been shown in thin GaAs/AlAs QWs that the effective electron masses increase with decreasing well width [40]. For all samples the

62

energy dependency of the effective electron mass is calculated using a modified Kane formula (Eq. (4.3)) [41, 42].

$$\frac{m_0}{m^*(\varepsilon)} = 1 + 2F + \frac{E_p}{3}\left(\frac{2}{E_g + \varepsilon} + \frac{1}{E_g + \Delta + \varepsilon}\right) \tag{4.3}$$

Here ε is the confinement energy of the lowest subband, E_p is the interband matrix element, F accounts for coupling to remote bands and Δ is the spin-orbit splitting of the valence band. The value of F was assumed to be 0.6 so that the effective mass for zero confinement energy results in the bulk value. The parameters of cubic GaN and AlN used for these calculations are given in Table 3. It has to be noted here that for all calculations the indirect band gap of AlN is used. This is due to the periodicity of the structure and is consistent with the results of the group of Prof. Schmidt. The conduction band offset is then used as a fitting parameter to achieve optimal agreement between calculated and measured intersubband transition energies.

Table 3: Parameters used for transition energy calculations.

Parameter	c-AlN	c-GaN
$E_{gap,300K}$ (eV)	5.3 [43]	3.2 [44]
a (Å)	4.38 [45, 46]	4.52 [45, 46]
m^*_{hh}/m_0	1.2 [47, 48]	0.8 [47, 48]
m^*_{lh}/m_0	0.33 [47, 48]	0.18 [47, 48]
m_e/m_0	0.19 [47, 48]	0.13 [47, 48]
a_c (eV)	-6.8 [49, 50]	-2.77 [49, 50]
c_{11} (GPa)	304 [49, 50]	296 [49, 50]
c_{12} (GPa)	152 [49, 50]	156 [49, 50]
E_p (eV)	23.84 [51]	16.86 [51]
F	-	0.6
Δ (eV)	-	0.017 [52]
ε_r		9.7 [44]

The intersubband- and interband transition energies in our SLs are calculated with an effective mass model using nextnano[3]. From Eq. (4.3) I obtain a maximum effective electron mass of 0.15 m_0 for the largest confinement energy. Fig. 36 shows a comparison between measured and calculated intersubband transition energies. The symbols

represent the experimental data. For fixed well- and barrier widths the conduction band offset is one parameter which influences the intersubband transition energy. For all samples I varied the CBO between 1.0 eV and 1.7 eV which corresponds to a ratio E_c:E_v between 50:50 and 90:10, respectively. The curves in Fig. 36 are calculated intersubband transition energies and are plotted versus the conduction band offset. First, it can be seen that the transition energy dependency on the CBO is increasing with decreasing well width and hence higher confinement energies. Therefore, the samples with higher intersubband transition energies provide higher reliability of the determined CBO. I find good agreement for all samples assuming a conduction band offset of 1.4 ±0.1 eV resulting in (74±5) % of the band gap differences E_{gap} between GaN and AlN.
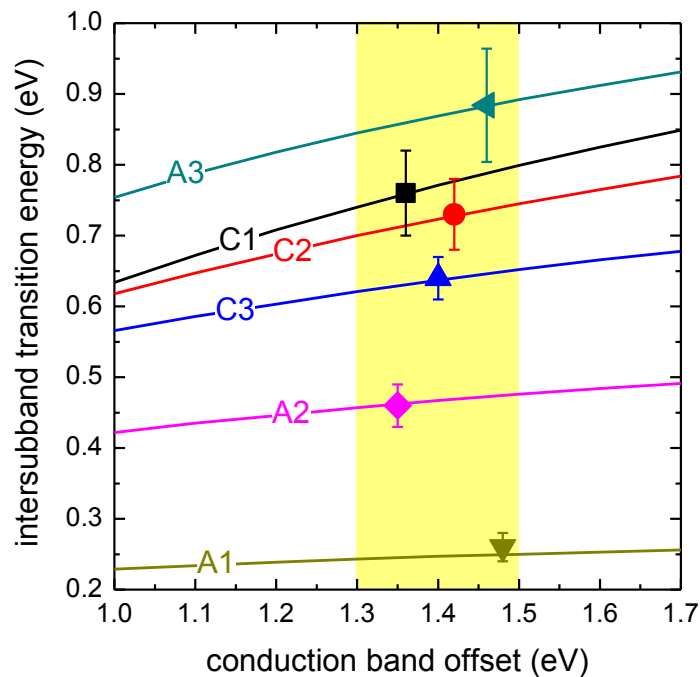
Fig. 36: Calculated intersubband transition energy for different conduction band offsets (lines) in comparison with experimental values (symbols). The bars indicate the calculated variation of the transition energy for a variation of the well width of ±1 ML.

In Fig. 37 calculated and measured interband transition energies are compared. These studies verify the results of the intersubband transition investigations. All samples show good agreement within the uncertainty resulting from a variation of the calculated transition energy for a variation of the well width of ±1 ML. The band offset dependency of the interband transition energy is larger for thinner QWs, e.g. samples C1, C2, C3 and A3. This results in smaller slopes of the calculated curves for thick QWs (A1, A2) than in thin QWs. Furthermore, it is found that a one monolayer fluctuation in QW thickness results in a larger change of transition energy for thinner QWs. All experimental data

show good agreement to the calculations based on the preliminarily determined band offsets and effective masses from intersubband spectroscopy. In addition, a fluctuation in layer thickness of more than one monolayer cannot be excluded for larger well widths. In summary, comparison of experimental intersubband and interband transition energies with model calculations gives evidence for a conduction band offset in the range of 1.4 ±0.1 eV. This value differs from experimental values for the hexagonal system where a CBO of 1.7 eV is found [53]. Although the local structure and bonding is very similar for both systems, there are significant differences. In contrast to the indirect cubic AlN, the wurtzite AlN is a direct semiconductor with a 0.7 eV larger band gap [54]. Furthermore, the band gap of cubic GaN is 0.19 eV smaller than in hexagonal GaN [44]. This may explain the differences in band offsets although the local structure is very similar.
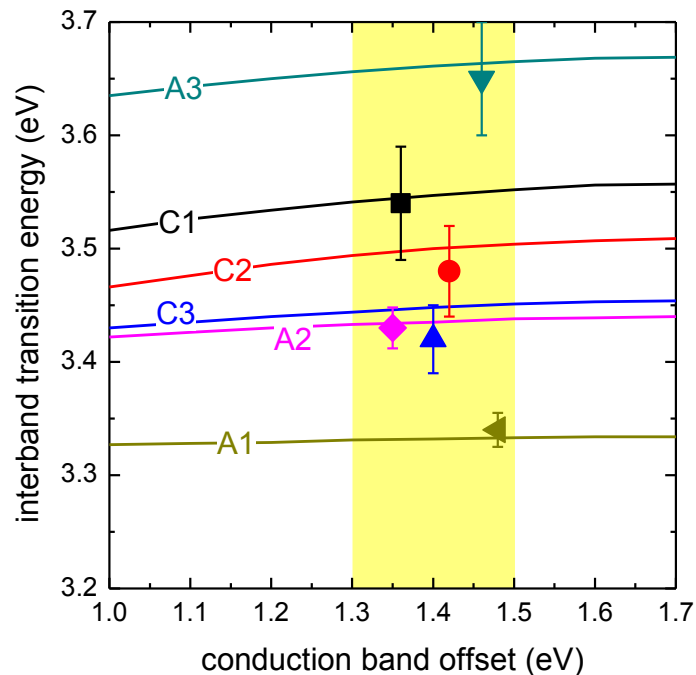
Fig. 37: Calculated interband transition energy for different conduction band offsets (lines) in comparison with experimental values (symbols). The bars indicate the calculated variation of the transition energy for a variation of the well width of ±1 ML.

In the following, I want to compare experimental results to the theoretical values obtained from Prof. Schmidt's group. For the theoretical calculations density functional theory (DFT) calculations [55, 56] using the projector-augmented wave (PAW) method [57, 58] as implemented in the Vienna ab-initio simulation package (VASP) [59] are performed. An energy cut-off of 400 eV was used throughout this work to expand the Kohn-Sham orbitals into plane wave basis sets. Within the DFT approach the electronic

band structure of semiconductors, and therefore the band gap, depends on the choice of the exchange correlation (XC) functional. Therefore, both the local density approximation (LDA) [60, 61] and nonlocal, screened Coulomb potential hybrid density functionals (HSE) [62, 63, 64, 65] are applied. The optimal agreement between experimental and theoretical data is achieved using the hybrid density functionals (HSE06) including the G_0W_0 approach. A detailed description of the theoretical model and the calculations can be found in [66]. The theoretical values are a CBO of 1.31 eV and a VBO of 0.56 eV. A comparison between experimental and theoretical values is given in Fig. 38.
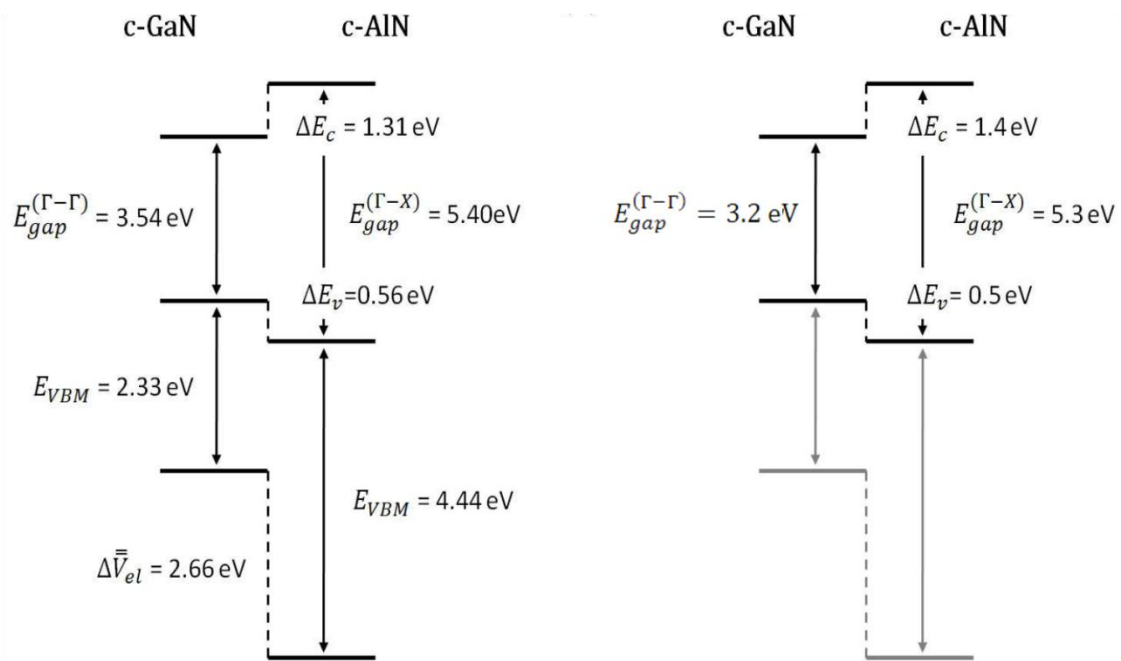
Fig. 38: Schematic diagram of the calculated type-I QP-band alignment (left hand) HSE06+G_0W_0 and (right hand) experimental results.

4.2.4 Conclusions

In summary, high quality cubic AlN/GaN superlattices were fabricated using plasma assisted MBE. The ratio of CBO to VBO between c-GaN and c-AlN in cubic III-nitride superlattices is determined by the analysis of intersubband- and interband transition energies. For the calculation of intersubband and interband transition energies the CBO is varied using the structural properties known from HRXRD. Optimal agreement between calculated and experimental data was achieved for a CBO to VBO ratio of (74:26) % within accuracy of ±5 % of the band gap difference E_{gap}. For all quantum wells an energy dependency of effective masses was taken into account to fit the experimental values. These values were verified by the analysis of interband transition energies of my samples in comparison with calculated values using the conduction band offset obtained from intersubband spectroscopy and model calculations. Furthermore, it is demonstrated that state-of-the art hybrid functional DFT calculations and the inclusion of many-body corrections on the G_0W_0 level are able to reproduce the experimental valence and conduction band offsets within an accuracy of ±0.1 eV. Finally, it is concluded that the comprehensive experimental and theoretical results give strong evidence for a CBO of (1.4±0.1) eV and a VBO of (0.5±0.1) eV in cubic AlN/GaN superlattice structures.

4.3 Resonant Tunneling

In this chapter, experimental data of the first resonant tunneling diodes based on group III-nitrides grown on 3C-SiC is presented. Clear room temperature negative differential resistance (NDR) is measured. Furthermore, the experimental data is compared to model calculations of IV-characteristics. Resonant tunnelling diodes of cubic Al(Ga)N/GaN are grown by plasma assisted molecular beam epitaxy on 3C-SiC (001). A pronounced NDR at about 1.2 V with a peak-to-valley ratio (PVR) of 1.3 to 2.7 is observed at room temperature. Experimental data is in good agreement with calculated IV-curves showing only a small deviation of 0.3 V of the resonance peak voltage. I find a decrease of the PVR when the IV-characteristic is measured repeatedly with short time intervals between the voltage-cycles. However, the IV-characteristics can be recovered fully when the diodes are illuminated by UV-light indicating charge trapping in our devices. Mesa structures are prepared by reactive ion etching. The size of the top ohmic contact is (25x11) μm^2. The Al content of the barrier material is varied between 30 % and 100 %.

The presented samples are grown by plasma assisted molecular beam epitaxy (PA-MBE) on free standing n-type cubic silicon carbide (3C-SiC). All resonant tunnelling diodes (RTDs) consist of a highly doped 50 nm thick c-GaN buffer layer doped with silicon (Si). Doping concentration is $5x10^{19}$ cm^{-3} for all samples. The buffer layer is followed by the resonant tunnelling structure. The tunnelling structure consists of a 1 nm thick unintentionally doped (u.i.d.) c-GaN quantum well (QW) embedded in two Al(Ga)N barriers which are unintentionally doped as well. The barrier thickness was varied between 1-3 nm while the Al-content in the barrier was 100 % for sample RTD1 and 30 % for samples RTD2 and RTD3. The structural properties of the tunnelling structures are given in Table 4. Layer thicknesses are measured in-situ by reflection high energy electron diffraction (RHEED) and growth rates are calculated with an accuracy of one monolayer. The double barrier structure is then capped by another highly doped 30 nm thick c-GaN cap layer. Furthermore, the double barrier structure is separated from the highly doped regions by 2 nm unintentionally doped c-GaN spacer layers to avoid interdiffusion of Si into the tunnelling structure. After growth a mesa structure is fabricated using UV-photolithography and reactive ion etching (RIE). On top of the mesa structure the ohmic top contact is deposited by thermal evaporation of 15 nm Ti, 50 nm Al, 15 nm Ti and 50 nm Au. The size of the top contact is (11 x 25) μm^2. The back contact is formed by indium on a copper plate. A schematic drawing of the RTD is shown in Fig. 39.
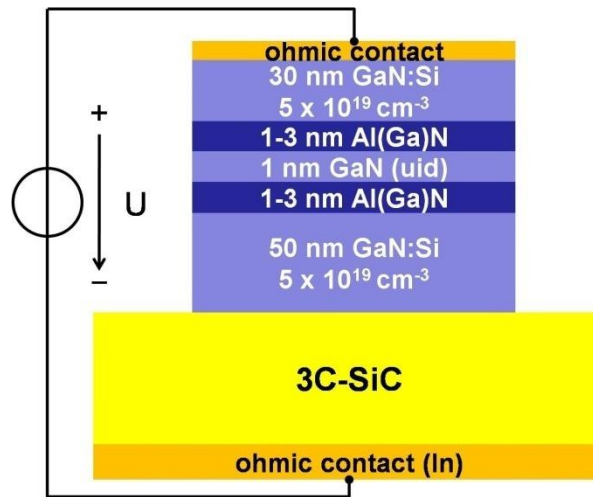
Fig. 39: Schematic drawing of the cubic Al(Ga)N/GaN resonant tunneling diode structure.

No further thermal annealing of the contacts is performed to avoid interdiffusion of the Si-dopants into the tunnelling structure. The fabricated devices are then characterized by dc current-voltage (I-V) measurements using an Agilent 4156C parameter analyzer. The voltage is applied to the top contact while the current through the whole structure is measured. All measurements are performed in dc-mode with an integration time of 0.64 ms and a step size of 0.01 V.

Table 4: List of RTD samples.

Sample	Barrier Material	Barrier Thickness	PVR
RTD1	AlN	3 nm	2.1
RTD2	$Al_{0.3}Ga_{0.7}N$	1 nm	1.3
RTD3	$Al_{0.3}Ga_{0.7}N$	2 nm	2.7

4.3.1 I-V-Characteristics

I-V-characteristics of three different devices reveal a clear NDR in forward bias direction. However, the resonance peak is only observed sweeping from zero bias to higher voltages and does not occur in the opposite direction. Furthermore, the I-V-curve is asymmetrical as an effect of the hetero-junction between 3C-SiC and c-GaN. No NDR can be observed in negative bias direction. Hence I will discuss only the forward bias direction in the following. In Fig. 40 the room temperature I-V-characteristics of samples RTD1, RTD2 and RTD3 are plotted for the first voltage sweep. The current is normalized for better comparability. Overall peak-to-valley ratios from 2.7 to 1.3 are observed.
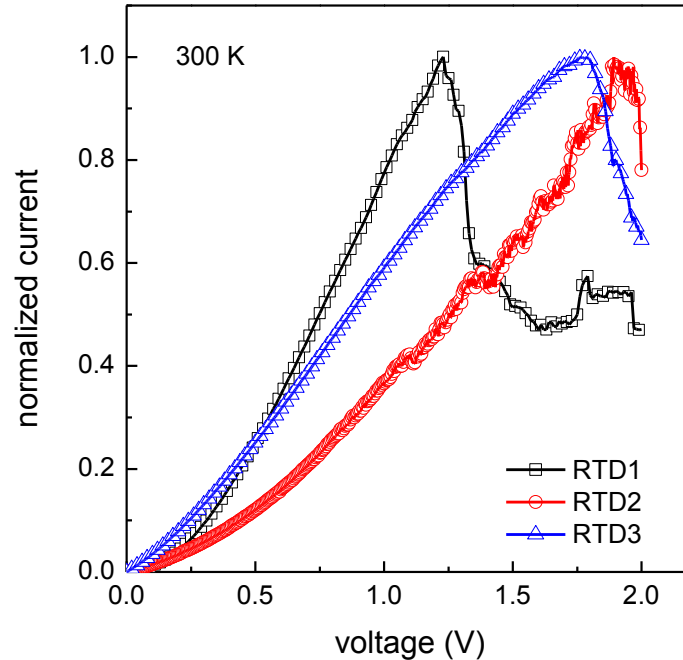
Fig. 40: Typical I-V-characteristics of samples RTD1, RTD2 and RTD3 for the first measurement at room temperature.

For samples with AlGaN barriers the resonance peak occurs at higher bias voltage than for RTD1, although for RTD1 the confinement energy is larger due to the larger band offset between barriers and QW. This is an effect of higher contact resistances of the different samples, because the contacts are not thermally annealed in order to avoid interdiffusion of dopants. Furthermore, the I-V-curves of RTD2 and RTD3 do not reach the current valley, because no bias voltages larger than 2 V are applied in the first measurement in order to protect the sample from being damaged by too high current densities.

When measuring the first I-V-characteristics, I observe that the NDR vanishes after the first or second voltage sweep, which has already been observed in the hexagonal system as well [67]. In order to find the physical origin of this behaviour, I have illuminated the sample with UV-light. An Osram Ultra Vitalux UV-lamp, with a maximum intensity at a wavelength of 370 nm, is used. After one hour of UV-exposure the NDR can be recovered several times. In Fig. 41 I-V-curves are plotted measured before and after illumination. The first and second I-V-curves show clear NDR which vanishes in the third sweep. After one hour of UV-illumination the I-V-characteristics are recovered and vanish again in the fifth sweep which is measured immediately after the fourth I-V-curve.
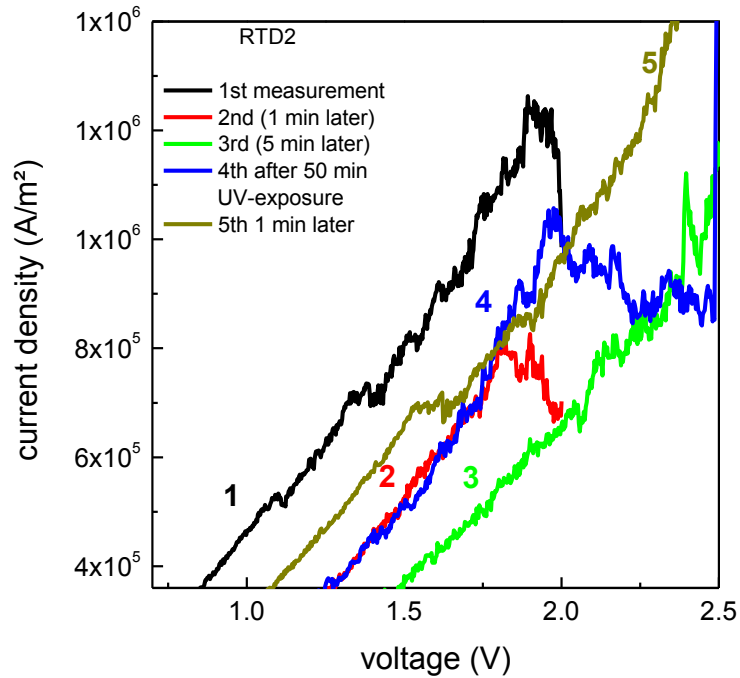
Fig. 41: Sequenced I-V-characteristics of RTD2 with vanishing (green and dark yellow curve) and recovering (blue curve) negative differential resistance.

The same behaviour is found for other samples as well and is an indication for charge trapping as is mentioned in [67] as well. Another effect can be observed in subsequent I-V-measurements. With increasing number of sweeps the peak-to-valley ratio decreases. Furthermore, the resonance peak shifts slightly to higher voltages. This effect has also been observed in hexagonal AlGaN/GaN double barrier diodes [67]. In Fig. 42 further current-voltage traces for RTD2 are plotted. One can clearly observe again the recovery of the NDR additional to the flattening and shifting of the resonance peak for I-V-sweeps six and eight. The decrease of the PVR may be an indication for a too low intensity of the UV-lamp. This effect has to be further investigated for spectral- and intensity-dependencies.
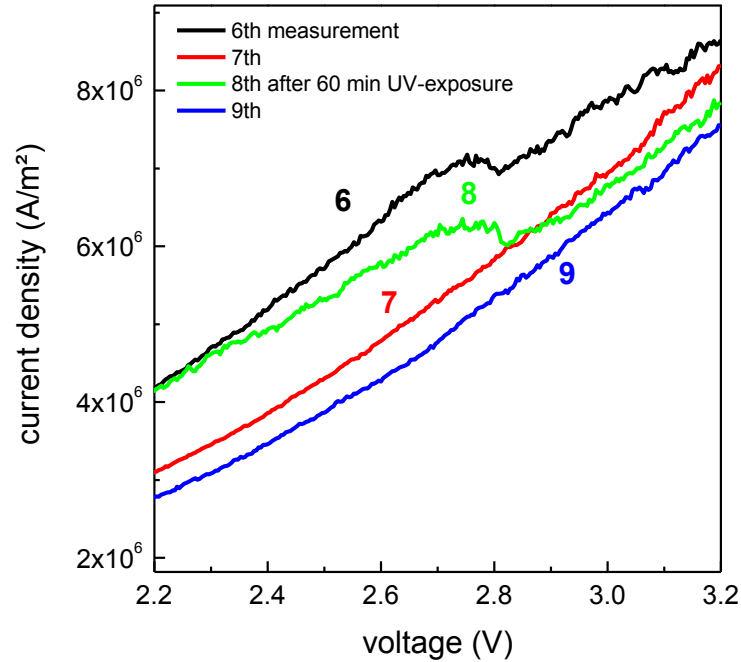
Fig. 42: Further I-V-characteristics of sample B showing shifted NDR peak and decrease in peak-to-valley ratio.

Besides room temperature measurements, I also investigate the I-V characteristics at low temperatures. For this purpose, the samples are mounted on the cooling finger of a closed cycle helium cryostat reaching a temperature of 7.5 K. In Fig. 43 the I-V characteristics of RTD1 at room temperature and 7.5 K are plotted for comparison. Both curves show a pronounced NDR around 1 V bias with peak-to-valley ratios of 2.1 at room temperature and 2.5 at 7.5 K. The current density at low temperature is about one order of magnitude lower due to a lower concentration of free carriers at low temperature.
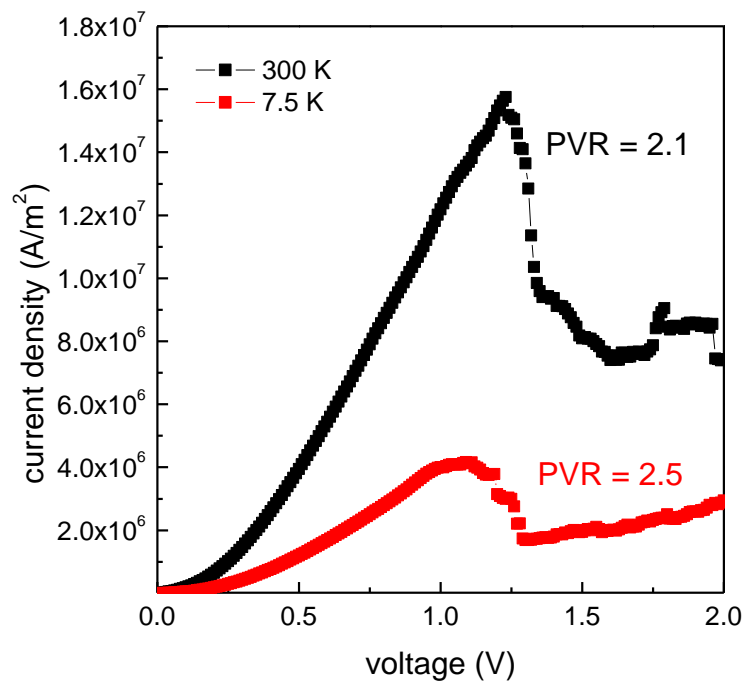
Fig. 43: Comparison of I-V characteristics of sample RTD1 at room temperature (black) and low temperature (7.5 K red). Both curves show pronounced NDR around 1 V bias. The PVR at low temperature is slightly higher, while the overall current density is about one order of magnitude lower.

4.3.2 Model Calculations

The tunnelling characteristics are calculated using nextnano³. I-V-characteristics as well as electron densities are calculated using the contact block reduction method (CBR). More information about the theoretical model can be found in [20]. In Fig. 44 the calculated room temperature I-V-characteristics of RTD1 are plotted together with the measured values. The current densities are normalized on the resonance peak value. Only a small deviation of the peak voltage between calculation and experimental data is observed.
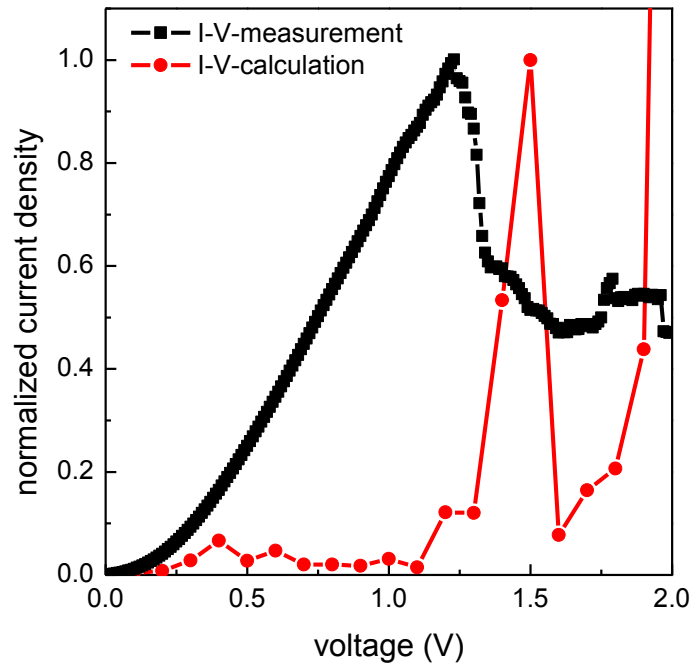
Fig. 44: Calculated I-V-characteristics of sample RTD1 (red dots) in comparison with the measured I-V-curve (black squares).

However, the deviation in the region below the resonance may be due to leakage current through conducting channels or non-resonant tunnelling which is not included in the calculation. Interface roughness and layer thickness fluctuations also influence the experimental results and lead to a broadening of the resonance peak. The calculated electron densities for three different bias voltages, below resonance, resonant tunnelling and off resonance are plotted in Fig. 45 together with the corresponding band structure. Only if the Fermi level is resonant with the localized state, a remarkable electron density is found inside the quantum well. If bias voltage is further increased, current transfer above the barrier structure occurs.
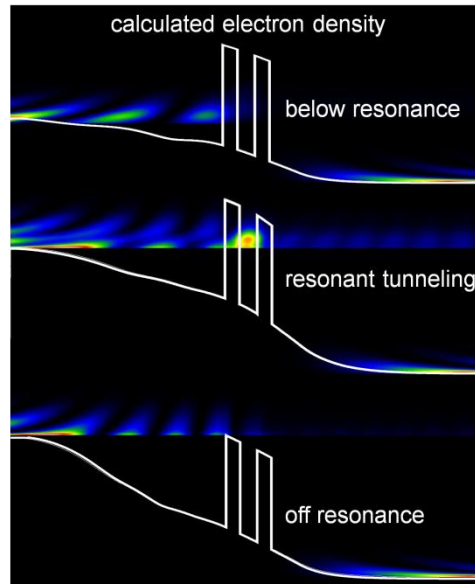
Fig. 45: Calculated electron density and corresponding band structure for three different bias voltages. Resonant tunneling occurs for the case of high density inside the QW (middle).

In order to further investigate the effect of vanishing NDR, I-V characteristics for sample RTD2 have been calculated introducing fixed charges at the AlGaN/GaN interface. These fixed charges result in a strong bending of the band structure pushing the quantized state below the Fermi level which is one possible explanation for the vanishing NDR. Fig. 46 shows the calculated I-V characteristics for a sheet concentration of fixed charges of 1e11 cm^{-2} (red line) and 1e12 cm^{-2} (blue line). Due to the smaller barrier height of RTD2, the calculated NDR occurs at lower voltage (0.6 V) compared to RTD1 (1.5 V). Assuming a sheet density of 1e11 cm^{-2} the NDR remains while the effect vanishes for a sheet concentration of 1e12 cm^{-2}. Furthermore, the calculated current density is higher assuming the higher sheet concentration. This is most likely due to the strong band bending allowing current transport above the barrier structure. These model calculations support the thesis of charge trapping effects leading to the disappearance of the NDR in subsequent measurements. A possible site for these traps is the interface between AlGaN and GaN. Illumination with high energetic light releases the trapped charges restoring the initial band bending and the NDR can be recovered.
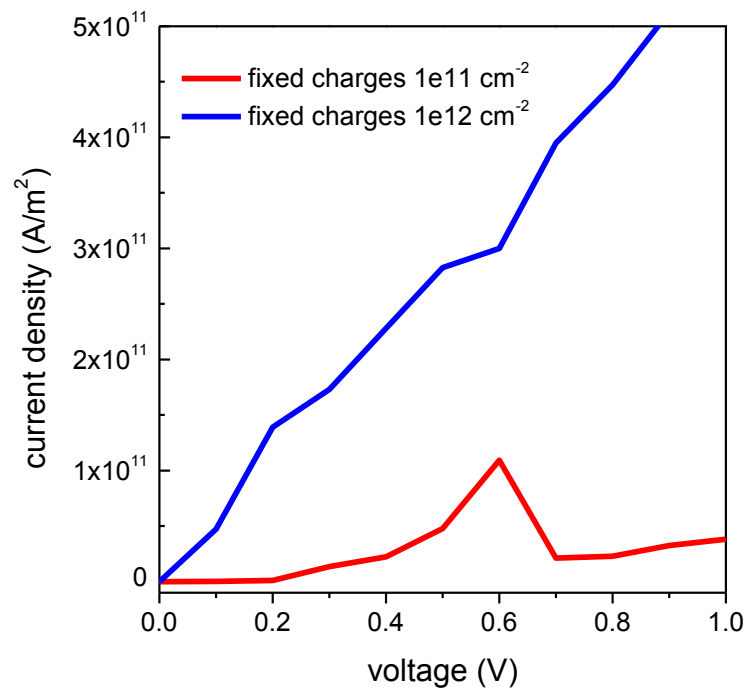
Fig. 46: I-V characteristics of sample RTD2 assuming two different sheet concentrations of fixed charges at the AlGaN/GaN interface. With higher concentration of fixed charges the NDR vanishes.

4.3.3 Conclusions

In conclusion, resonant tunnelling diodes with reproducible I-V-characteristics and recoverable NDR based on Al(Ga)N/GaN double barrier structures were grown on free standing 3C-SiC (001) by plasma assisted molecular beam epitaxy. All devices show clear negative differential resistance with peak-to-valley ratios between 1.3 and 2.7. Furthermore, model calculations of the I-V-characteristics and electron density were performed using nextnano³ showing only a small deviation of the resonance peak voltage of 0.3 V. After the first I-V-measurements the PVR decreases, but can be fully recovered by illuminating the samples with UV-light. I suppose that this effect is due to charge trapping in our device. This is supported by calculations of the I-V-characteristics assuming fixed charges at the Al(Ga)N/GaN interface showing no negative differential resistance.

4.4 Absorption in Fountain Laser Structures

In this chapter, I will show first absorption results in coupled AlN/GaN MQWs as a first step towards an unipolar light emitting device of cubic AlN/GaN. As described in chapter 3.3, I have grown multiple coupled AlN/GaN quantum wells by MBE. Model calculations are performed for asymmetric coupled QWs (ACQW) to show the tunability of transition energies and variation of the distance between the e1 and e2 state. As mentioned in chapter 3.3, the energy separation between e1 and e2 should be in the order of the LO-phonon energy to effectively depopulate e2 to reach occupation inversion. Based on this theoretical preliminary work, two series of ACQW samples of different thickness were grown. The thickness of the first QW which is doped by silicon is varied between 1.8 nm and 2.0 nm for series A, while it is kept at a thickness of 2.1 nm for series B. The tunneling barrier of AlN is varied between 0.9 nm and 1.1 nm for series fountain A and is kept constant at 0.9 nm for series fountain B. The second GaN QW thickness is varied from 1.0 nm to 1.1 nm for series fountain A and from 0.7 nm to 1.9 nm for series fountain B. The coupled QWs are separated to the next coupled MQW system by a 2.3 nm AlN barrier for series fountain A and a 3 nm AlN barrier for series fountain B. These structures are chosen to investigate the effects of the separation between the two lower electron states on the absorption spectra. The given thicknesses are estimated by calculation of the ISBT energy correlated to RHEED and HRXRD data. Thus, thickness variations below one monolayer (0.2 nm) are obtained, which are meant as a nominal thickness and not meaning an accuracy of thickness estimation below 1 ML. The nominal layer thicknesses and the doping concentrations are summarized in Table 5.

Table 5: Nominal layer thicknesses and doping concentrations of coupled QW samples.

Sample	AlN 1	GaN 1	AlN 2	GaN 2	Si-Doping Concentration
fountain A1	2.3 nm	1.8 nm	0.9 nm	1.1 nm	1e20 cm^{-3}
fountain A2	2.3 nm	1.8 nm	1.1 nm	1.0 nm	1e20 cm^{-3}
fountain A3	2.5 nm	1.9 nm	0.9 nm	1.1 nm	1e20 cm^{-3}
fountain A4	2.3 nm	2.0 nm	1.1 nm	1.0 nm	1e20 cm^{-3}
fountain B1	3 nm	2.1 nm	0.9 nm	1.6 nm	1e19 cm^{-3}
fountain B2	3 nm	2.1 nm	0.9 nm	1.4 nm	1e19 cm^{-3}
fountain B3	3 nm	2.1 nm	0.9 nm	1.2 nm	1e19 cm^{-3}
fountain B4	3 nm	2.1 nm	0.9 nm	0.9 nm	1e19 cm^{-3}
fountain B5	3 nm	2.1 nm	0.9 nm	0.7 nm	1e19 cm^{-3}
fountain B6	3 nm	2.1 nm	0.9 nm	1.9 nm	1e19 cm^{-3}

4.4.1 Model Calculations on Asymmetric Coupled Quantum Wells

For a better theoretical understanding of ACQWs, band structure calculations are performed using nextnano³. A calculated band structure for one period of ACQW is given exemplarily for sample fountain B1 in Fig. 47. The Fermi level (E_F) is slightly above e1 leaving e2 unoccupied. Furthermore, the squared wave functions of the electrons corresponding to the localized states are shown. One can clearly see that electrons in the occupied state e1 are most likely confined in QW GaN1 with only small penetration through the AlN2 tunneling barrier resulting in a weak tunneling probability. Electrons in e2 are basically confined in GaN2 with a slightly higher tunneling probability than e1. From the squared wave function in e3 state I conclude again that electrons are basically confined in GaN1 but have a much higher tunneling probability due to the high energy of this state. The confinement in GaN1 is desirable due to a large spatial overlap of wave functions between e1 and e3 resulting in a high transition probability from e1 to e3 followed by a tunneling process to GaN2 where the recombination should take place. Afterwards a phonon assisted scattering process from e2 to e1 is very effective to depopulate e2.
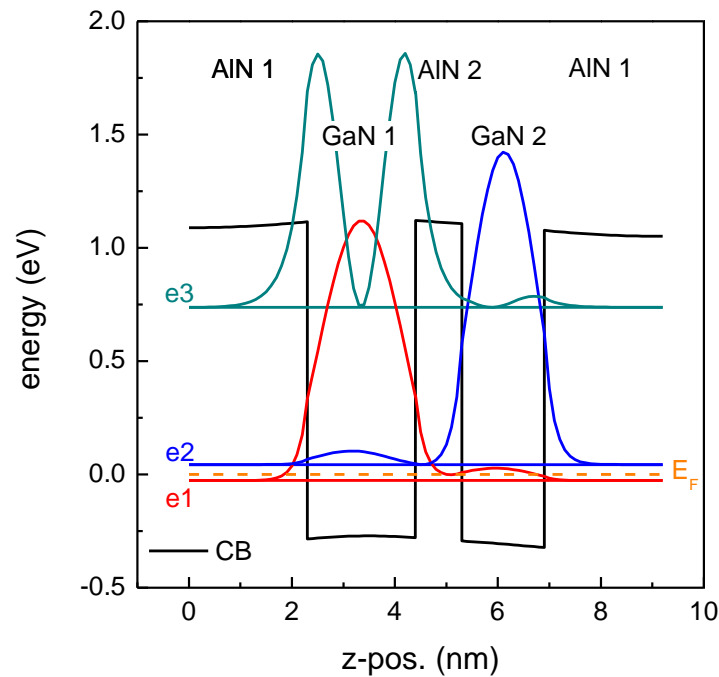
Fig. 47: Calculated conduction band structure for sample fountain B1.

To investigate the dependency of the position of the localized states e1-e3 and thereby the transition energies, three different parameters are varied. First, the thickness of the Si-doped QW GaN1 is varied from 1-3 nm in steps of 0.2 nm while the difference in thickness between GaN1 and GaN2 is kept constant (GaN2 is 0.4 nm thinner than GaN1). The thicknesses of all AlN layers are constant for these calculations. AlN1 is 3 nm thick and the tunneling barrier AlN2 is 1 nm thick. The transition energy for the transitions e1-e3, e3-e2 and e2-e1 as a function of GaN1 thickness is shown in Fig. 48. The transition energy e1-e3 as well as e3-e2 can be varied over a large spectral range by changing the QW thickness and can be tuned to the 1.55 µm (0.8 eV) region which is especially interesting for optical telecommunication. For QW thicknesses below 1.6 nm the confinement energy is that high that only two localized states are formed in the ACQW structure which is undesirable for the planned application. Furthermore, I find that the e2-e1 transition energy is slightly shifted as well although I keep the difference in thickness between GaN1 and GaN2 constant. This can easily be explained by the fact that the confinement energy rises stronger for thin QWs and thereby the difference between GaN1 and GaN2 becomes more pronounced.
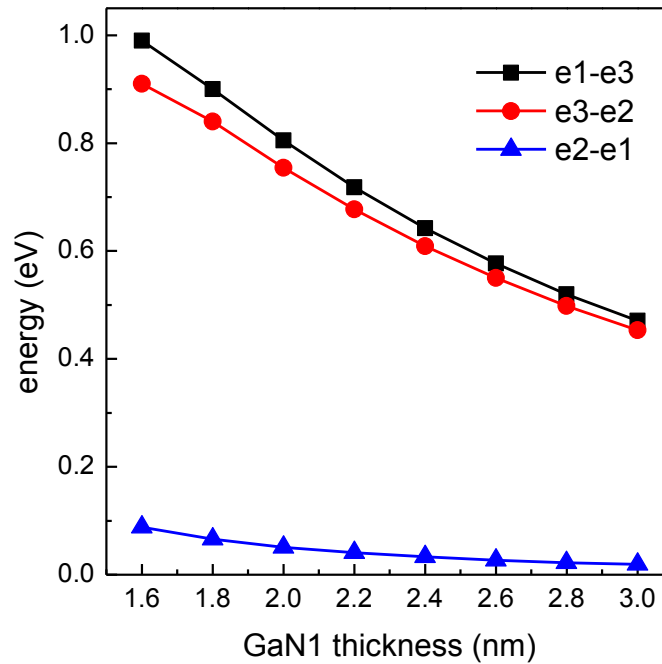
Fig. 48: Calculated transition energies for one pair of ACQWs for a thickness variation of QW GaN1 while GaN2 is 0.4 nm thinner than GaN1 for all calculations.

In the following I want to investigate the dependency of the transition energies depending on a thickness variation of only one QW. Hence, the thickness of GaN1 is kept constant (1.9 nm) and GaN2 thickness is varied between 0.9 nm and 1.1 nm. The calculated transition energies are plotted versus the GaN2 thickness in Fig. 49. Depending on the thickness of GaN2, the e3-e2 transition energy is clearly shifted while the e1-e3 transition remains unaffected by this thickness variation. This is due to the localization of the e1 and e2 states. Because e1 is nearly completely localized in GaN1 with only a small interaction with GaN2, the effect of a thickness variation in GaN2 is very small. The energetic position of e2 is strongly dependent on the GaN2 thickness due to its localization in GaN2. The variation of the GaN2 thickness shifts e2 to higher energies for thinner GaN2 and therefore the transition energy e3-e2 is reduced. The same calculations using a constant GaN2 and a variation in the GaN1 thickness show that all three transition energies are shifted. This is consistent with the preliminary results, because the e3 state is mainly localized in GaN1. A variation of the GaN1 thickness affects e1 and e3 state while e2 stays unaffected resulting in a shift of all transition energies. The calculated transition energies for a variation of the GaN1 thickness between 1.6 nm and 2.6 nm assuming a constant GaN2 thickness of 1.2 nm are shown in Fig. 50.
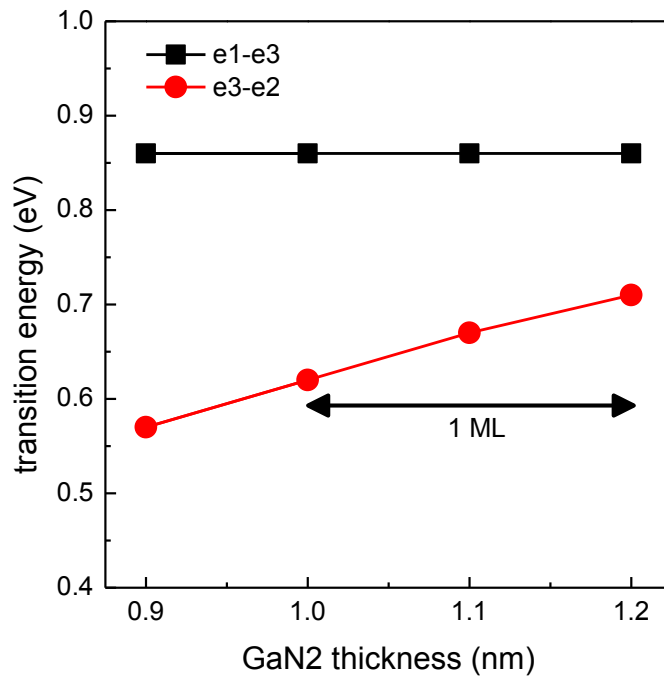
Fig. 49: Calculated transition energies for a variation of GaN2 thickness between 0.9 nm and 1.2 nm with a constant GaN1 thickness of 1.9 nm. While e3-e2 is clearly shifted e1-e3 stays unaffected by this variation. A thickness fluctuation of one monolayer results in a shift of the e3-e2 transition of about 100 meV.
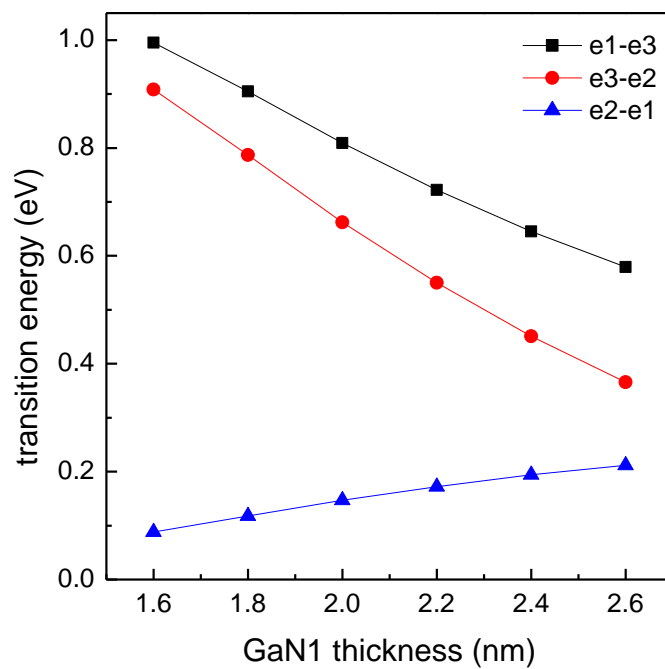
Fig. 50: Calculated transition energies for a variation of GaN1 thickness between 1.6 nm and 2.6 nm with a constant GaN1 thickness of 1.2 nm. All three transitions show a clear shift. Due to the strong localization of e1 and e3 in GaN1 these states are affected by the thickness variation while e2 stays unaffected.

After the investigation of the consequences of thickness variation using a constant difference between GaN1 and GaN2, constant GaN1 and constant GaN2 thickness I want to go on with the optimization of ACQW structures for optical telecommunication applications. I have already shown in Fig. 48 that the 1.55 μm region is covered by the suggested ACQW structures. Furthermore, I have mentioned the requirements for an optically pumped laser device. In the following calculations, I will show the possibility to optimize the ACQW structures to fulfill the requirements for a quantum fountain laser. Fig. 48 gives a good hint for a starting point of such an optimization. A thickness of 1.8 nm for GaN1 and 1.4 nm for GaN2 fits the transition energy of 0.8 eV pretty good. In addition, the energetic difference between e2 and e1 should be in the order of the LO-phonon energy which is 92 meV for cubic GaN. This is not yet fulfilled (Δe2-e1=66 meV). Therefore a series of transition energy calculations is performed in order to minimize the deviation from the requirements. For GaN1 thicknesses of 1.7 nm, 1.8 nm, and 1.9 nm the GaN2 thickness is slightly varied. The results of these calculations are shown in Fig. 51. On the x-axis the combination of GaN1/GaN2 thickness is given. Dots represent the calculated e3-e2 transition energy, triangles the e2-e1 transition energy. The blue line marks the LO-phonon energy and the red line marks the desired transition energy corresponding to a wavelength of 1.55 μm. Best agreement to both requirements is reached for the second combination of 1.8 nm/1.3 nm which is highlighted by the yellow box.
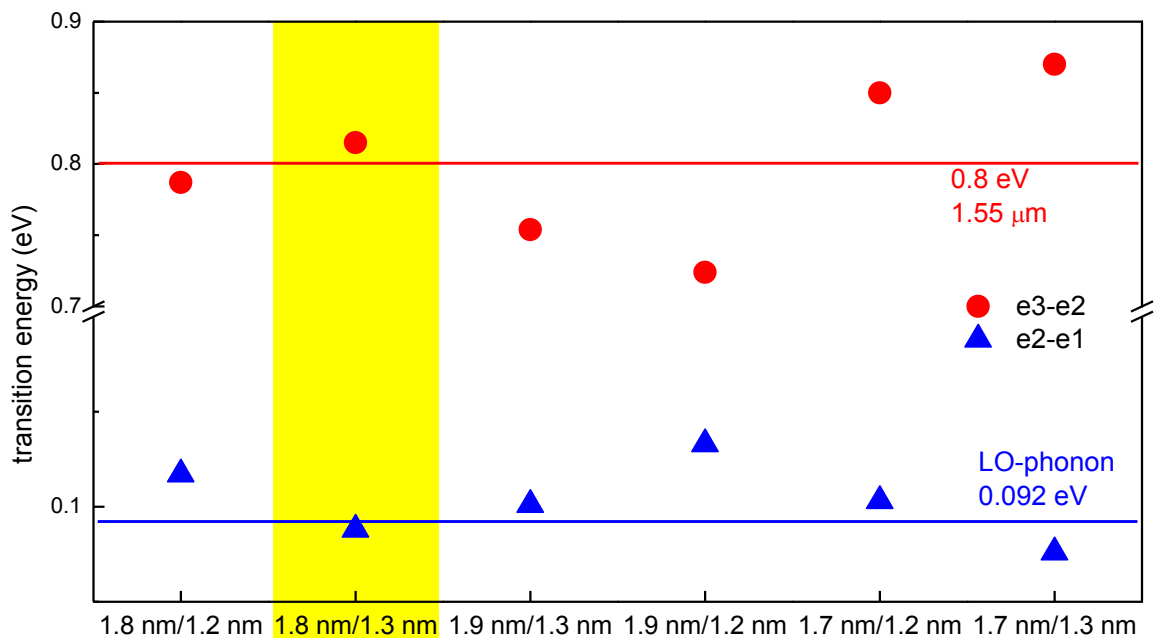
Fig. 51: Optimization of ACQW structure for application in optical telecommunication. On the x-axis the combination of GaN1/GaN2 thickness is given. Dots represent the calculated e3-e2 transition energy, triangles the e2-e1 transition energy. The blue line marks the LO-phonon energy and the red line marks the desired transition energy corresponding to a wavelength of 1.55 μm. Best agreement to both requirements is reached for the second combination of 1.8 nm/1.3 nm which is highlighted by the yellow box.

4.4.2 Structural Properties of Fountain Laser Structures

The structural properties of the samples are investigated using high resolution X-ray diffraction (HRXRD). Clear SL satellites revealing the high quality of the samples are detected in reciprocal space maps (RSM) of the asymmetric (113) reflection. Furthermore, conclusions on the strain status of the SL can be drawn from the positions of the satellites. Fig. 52 shows the RSM of the (113) reflection for fountain A2. The position of the satellites with respect to the position of the buffer layer indicates that the multilayer system forms an equilibrium lattice constant between c-GaN and c-AlN. This equilibrium lattice constant results in strained GaN and AlN epilayers. This leads to compressive strained QWs and tensile strained barriers and has to be taken into account in layer thicknesses and changes in the band gap energy.
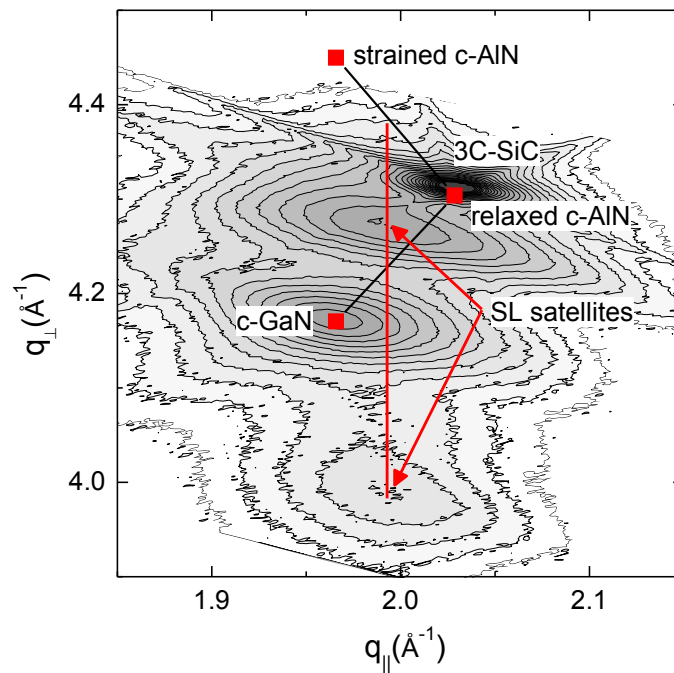
Fig. 52: RSM of the (113) reflection of sample fountain A2 revealing clear SL satellites. The position of the SL satellites reveals that the SL forms an equilibrium lattice constant between GaN and AlN.
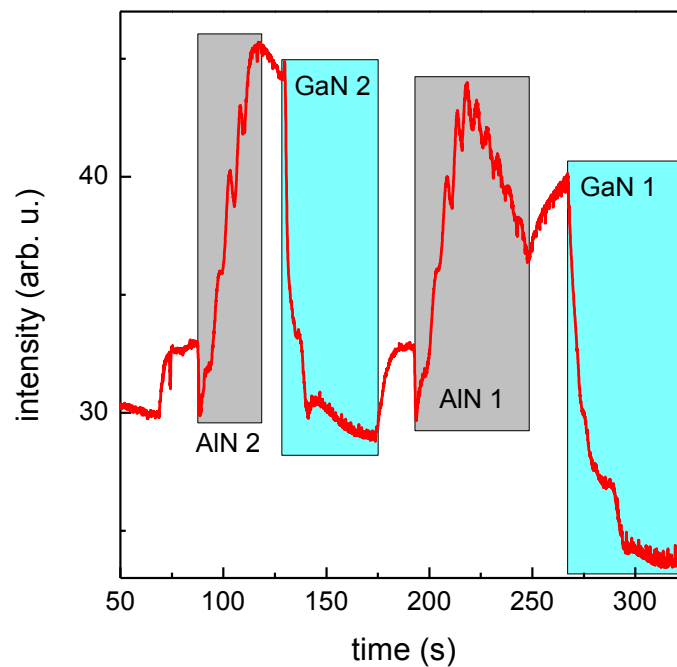
Fig. 53: RHEED intensity oscillations during growth of one cycle of the ACQW structure. GaN QWs are highlighted by blue and AlN barriers by gray. After each layer a short growth interruption is made to evaporate excess material.

The structural data of all coupled QW samples is given in Table 5 and was confirmed by RHEED oscillations and HRXRD data. Fig. 53 shows a typical time scan of RHEED intensity during growth of one period of ACQW. During AlN growth clear intensity oscillations are observed while no oscillations occur during GaN growth. More details on optimal growth conditions of cubic GaN and AlN can be found in [68].

For further investigation of the structural properties of the multilayer structures another sample containing the same layer thicknesses as sample fountain B1 was grown and prepared for TEM. Fig. 54 shows the TEM bright field picture of the sample, the acceleration voltage is 200 kV and the magnification is x400k. At the bottom of the picture we see the GaN buffer layer (larger dark area). Due to the atomic weight difference between Ga and Al the brighter layers can be assigned to AlN and the darker areas to GaN. The picture starts at the bottom with the GaN buffer layer, followed by the first 3 nm AlN barrier. After that the ACQW structure follows containing 2.1 nm GaN:Si QW1, 1 nm AlN tunneling barrier and 1.6 nm GaN QW2. It can clearly be seen that the starting roughness of the buffer layer does not result in disruption of the layers, although they are very thin (AlN tunneling barrier ~1 nm). The initial roughness of the buffer layer is a result of the relaxation process of GaN on 3C-SiC. After the critical thickness of 2-3 ML the GaN buffer relaxes forming 3D islands similar to the Stranski-Krastanow growth mode. These islands are then overgrown forming a 2D layer again, but with a roughness of 2-3 nm. The roughness of the 3C-SiC is in the order of 0.5 nm while the roughness of the buffer layer is in the order of 1-3 nm. Nevertheless, the MQW structure covers the roughness like a cloth, forming this wavelike structure. Besides the undulated structure, the thickness of the single layers undergoes thickness fluctuations. An area with such fluctuations is highlighted by the red circle. This gives first proof that the previous assumption of a fluctuation in the order of ±1 ML is realistic. Additionally, we get a first idea of the distribution of defects in the structure. Some areas are almost defect free (yellow circle) while other areas are very defect rich (blue circle). Contrary to GaAs/AlGaAs, defects are not annihilated by the superlattice [69, 70, 71], they pass the whole structure more or less unaffected. Nevertheless, I want to focus on the red box which shows an area of smooth layers without any fluctuations or wave form. I conclude that besides the thickness fluctuations and defect rich areas, a large amount of the sample shows the desired structure giving proof that even such a complicated ACQW structure can successfully be grown by MBE of cubic III-nitrides. Unfortunately the TEM system was installed a short time ago and the length scale was not calibrated so that the real thickness of the layers could not be measured, but from RHEED oscillations I know the thickness of the AlN layers and can estimate a length

scale. The thicker AlN layers (bright layers) have a thickness of 3 nm. Now I assign this 3 nm to an arrow representing the thickness of the AlN barrier. Rotating this arrow makes it possible to estimate how often this arrow fits into the in plane length of the undistorted area (zoom of Fig. 54). Using this trick I can estimate the elongation of the undistorted area to about 48 nm, which is in the order of the exciton diffusion length in cubic GaN (30 nm) [72]. Furthermore, I have calculated the exciton Bohr radius λ_B for cubic GaN to be in the order of 5 nm using Eq. (4.4) [73]. From this estimation I conclude that the possibility for an exciton, generated in an undistorted area, to diffuse into distorted areas or to be affected by areas with high dislocation density is marginal.

$$\lambda_B = \frac{4\pi \varepsilon_r \varepsilon_0 \hbar^2}{\mu e^2} \tag{4.4}$$

$$\frac{1}{\mu} = \frac{1}{m_e^*} + \frac{1}{m_{hh}^*} \tag{4.5}$$

The exciton Bohr radius λ_B is calculated using the dielectric constant ε_r, the electric field constant ε_0, the reduced Planck constant $\hbar$, the electron charge e and the reduced mass μ, which is calculated as shown in Eq. (4.5). I have used the effective electron mass m_e^* and the effective mass of a heavy hole m_{hh}^*, which form the exciton. The values are already given in Table 3.

To summarize what we can learn from this TEM picture:

- Thickness fluctuations of about ±1 ML
- Roughness of the buffer layer has minor effects on the SL itself
- Large areas of constant thickness and the desired structure can be found
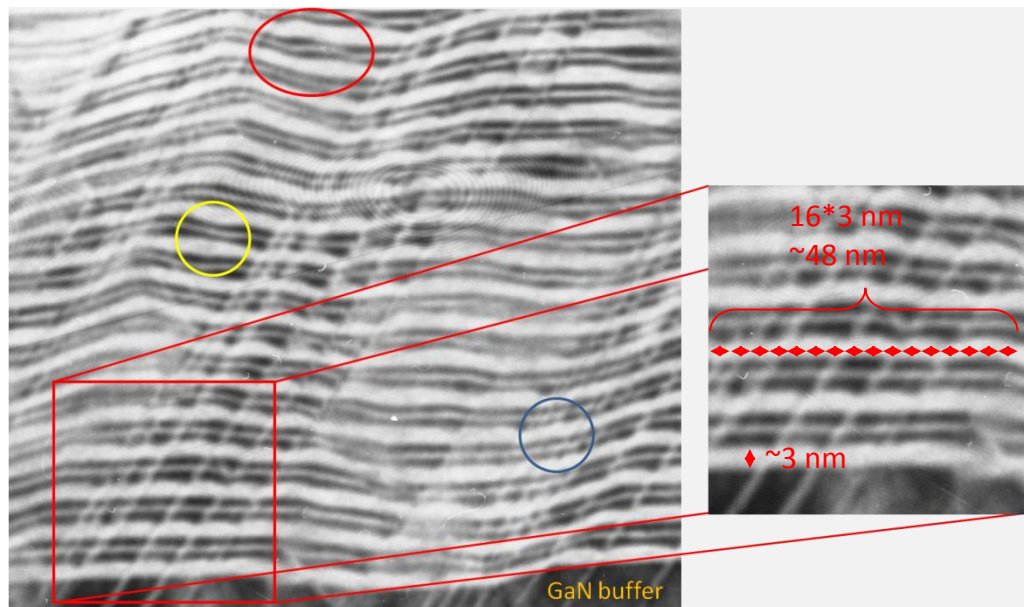
Fig. 54: TEM bright field picture of a sample with the same structure like fountain B1. Layer thickness fluctuations are found (red circle) as well as defect rich (blue circle) and low defect density areas (yellow circle) can be found. Nevertheless large areas show the desired structure.

4.4.3 Influence of Strain on Intersubband- and Interband Transitions

As mentioned in 4.4.2, the MQWs form an equilibrium lattice constant resulting in partial strain on the QWs as well as the barriers. In the following I want to shortly discuss the influence of strain on intersubband- and interband-transitions. Therefore, I calculate the transition energies for the structures given in Table 5 and compare the results to measured transition energies. I calculate the two extremes of strain meaning first the AlN barriers fully strained on the GaN QWs and then the AlN barriers fully relaxed, while the GaN QWs are fully strained.

First, I want to focus on the intersubband transitions. In Table 6 the calculated ISBT energies for the above mentioned strain of barriers or QWs are summarized. Besides the calculated values, the measured transition energies are given for comparison. Good agreement between measurement and calculation is found. The strain results in a small shift in the order of 10 meV of the ISBT energy and is negligible compared to the effect of a monolayer fluctuation of around 100 meV.

Table 6: Measured ISBT energies and calculated values for different strain status.

Sample #	Strained On	e1-e3 (eV) (calc)	e1-e3 (eV) (measured)	e2-e3 (eV) (calc)	e2-e3 (eV) (measured)
Fountain A1	AlN	0.85	0.87	0.69	0.67
	GaN	0.86		0.70	
Fountain A2	AlN	0.85	0.87	0.65	0.63
	GaN	0.86		0.66	
Fountain A3	AlN	0.81	0.81	0.64	0.63
	GaN	0.82		0.64	
Fountain A4	AlN	0.77	0.77	0.54	0.55
	GaN	0.78		0.54	

Next I want to perform the same considerations for interband transition energies and compare the results to measured cathodoluminescence data. In Table 7 the calculated IBT energies for the above mentioned strain of barriers or QWs are summarized. For both, strained and relaxed QWs, the energetic lowest transition is the conduction band heavy hole band transition (e1-hh1). The influence of the strain on the interband transition energy is definitely larger and is in the order of 80 meV and a factor of two larger than the effect of a thickness fluctuation of one ML which is in the order of 40 meV. Therefore, I conclude that the strain of the MQW structure has a considerable

influence on the CL spectra. This effect is larger for samples A1 and A2 due to a smaller volume fraction of GaN compared to AlN due to thinner QWs.

Table 7: Measured IBT energies and calculated values for different strain status.

Sample #	Strained On	IBT energy (eV) (calc)	CL peak maximum (eV)
fountain A1	AlN	3.66	3.66
	GaN	3.58	
fountain A2	AlN	3.66	3.66
	GaN	3.58	
fountain A3	AlN	3.64	3.58
	GaN	3.56	
fountain A4	AlN	3.62	3.58
	GaN	3.54	

4.4.4 Optical Properties of Fountain Laser Structures

My MQW samples are optically investigated using cathodoluminescence (CL) and Fourier transform infrared spectroscopy (FTIR). CL probes interband transitions (IBT) while FTIR reveals ISBTs in the infrared spectral range. Fig. 55 shows CL spectra of samples fountain A2 and A4. A clear shift of the emission maximum to higher energies is observed with narrower QWs. The arrows indicate the calculated transition energies of the e1-heavy hole 1 (hh1) for relaxed GaN QWs and strained barriers (blue) and for strained GaN QWs with relaxed barriers (black). The influence of the strain is consistent with HRXRD data showing a partial strain of the QWs with respect to the buffer layer which is fully relaxed. In Table 7 the measured peak maxima of all CL spectra are given in comparison to calculated transition energies.
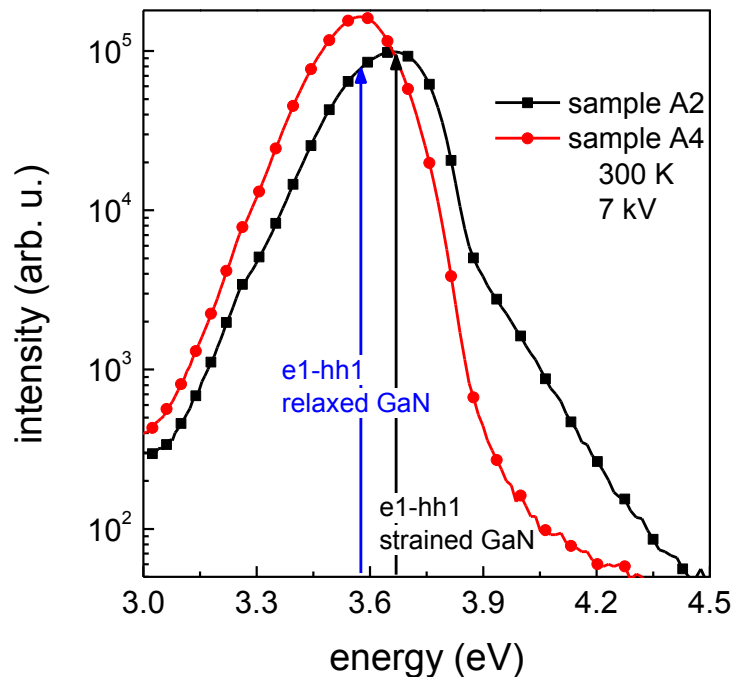
Fig. 55: Room temperature CL spectra of sample fountain A2 (black line) and sample fountain A4 (red line).The arrows indicate the calculated e1-hh1 transition energies for fully relaxed GaN QWs and strained AlN barriers (blue) and for fully strained GaN QWs on relaxed AlN barriers (black) for sample A2 exemplarily.

The infrared absorption spectrum of sample fountain A1 is shown in Fig. 56. All samples show pronounced TM-polarized absorption ranging from 0.55 to 0.87 eV. The full width at half maximum (FWHM) is about 450 meV, which is much higher than the typical broadening of 150 meV observed in single AlN/GaN QWs [9]. The shape of the absorption is asymmetric and can be fitted by two Gaussian functions. The presence of two components in the ISB absorptions can be attributed to the transitions from the

ground state and from the first excited state. It is likely that the doping concentration exceeds the nominal one, so that the Fermi level is above the second energy level and the absorption from e2 to e3 can be observed. For sample fountain A1 transition energies of 0.87 eV (e1-e3) and 0.67 eV (e2-e3) are found. From the area underneath the Gaussian fit curves I conclude that the absorption e1-e3 is comparable to e2-e3 which is a hint for comparable occupation as a result of too high doping. The FWHM of individual transitions is taken from the Gaussian fit and is in the order of 200 meV for both transitions. The broadening can be explained by thickness fluctuations of the QWs which are confirmed by model calculations (see Fig. 49).
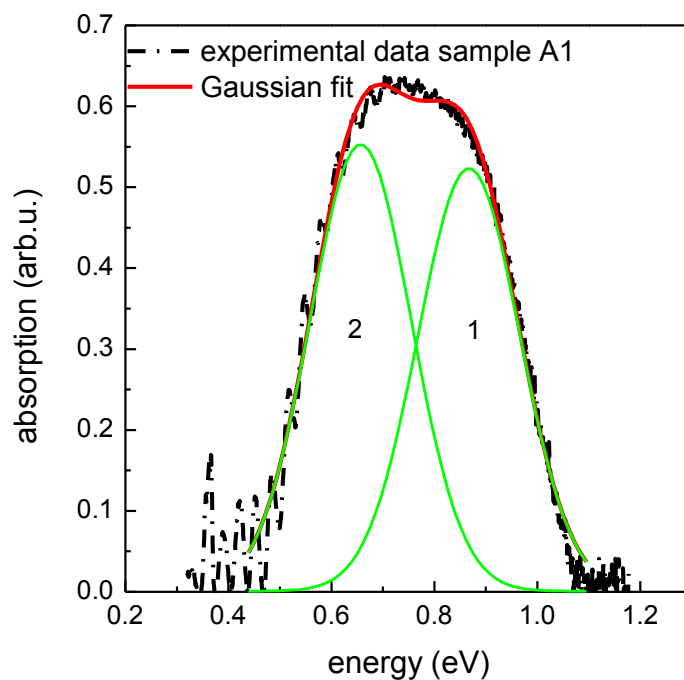
Fig. 56: Sample fountain A1 room temperature (RT) absorption spectrum (black) with Gaussian fits (green) and cumulative curve (red).

In Fig. 57 the absorption spectrum of sample fountain A2 is plotted together with a fit by two Gaussian functions. The maxima of the Gaussian curves are at 0.87 eV and 0.63 eV. For this sample the e2-e3 absorption is found to be much weaker than the e1-e3 transition (area under curve 2 is more than a factor of 2 lower than under curve 1). This is due to a larger separation between e1 and e2 in sample A2 compared to sample A1 and therefore a larger distance to the Fermi level assuming same doping concentration for both samples. In Table 8 the experimental transition energies are summarized in comparison to the calculated transition energies for samples fountain A1-A4. Good agreement between measurement and calculation is found.
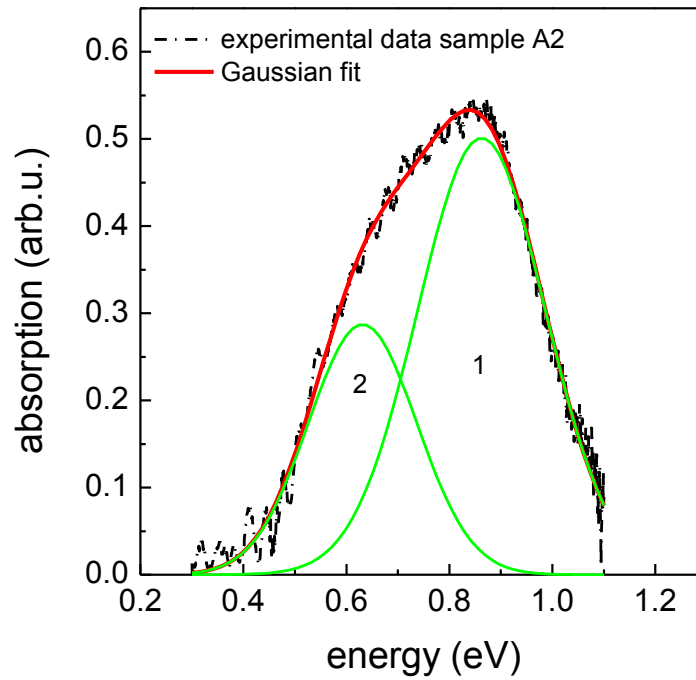
Fig. 57: Sample fountain A2 (RT) absorption spectrum (black) with Gaussian fits (green) and cumulative curve (red).

Table 8: Calculated and measured ISBT energies for series fountain A.

Sample	e1-e3 exp.(calc.)	e2-e3 exp.(calc.)
fountain A1	0.87 eV (0.85 eV)	0.67 eV (0.69 eV)
fountain A2	0.87 eV (0.85 eV)	0.63 eV (0.65 eV)
fountain A3	0.81 eV (0.81 eV)	0.63 eV (0.64 eV)
fountain A4	0.77 eV (0.77 eV)	0.55 eV (0.54 eV)

4.4.5 Conclusions for Series Fountain A

Quantum confinement in asymmetric coupled AlN/GaN QWs is studied theoretically and experimentally. Asymmetric coupled quantum wells of cubic AlN/GaN are successfully grown by MBE. Intersubband absorption in the 0.55-0.87 eV range is observed at room temperature. The asymmetric shape of the infrared absorptions reveals the existence of a three level system. The structures are attributed to the contributions of the e1-e3 as well as the e2-e3 transitions. This is confirmed using model calculations which reproduce transition energy and position of Fermi level reliably. The e2 state is populated due to the excessive carrier concentration, which may originate from higher background doping than estimated. Moreover, the calculated transition energies for the given QW thicknesses are in good agreement with experimental data.

From HRXRD results I conclude, that the MQWs form an equilibrium lattice constant between GaN and AlN. Interband transitions are observed using CL. In CL spectra a clear shift to higher energies for thinner QWs is found. Transition energy calculations show that the emission peak is influenced by the strain of the QWs shifting the emission band maximum to higher energies. These results show the potential of asymmetric coupled quantum wells of cubic AlN/GaN for optically pumped ISB devices. For future samples the doping concentration should be decreased in order to keep the e2 state unpopulated. Hence, the Si-doping concentration is decreased by one order of magnitude for the second series of ACQW samples, series B.

4.4.6 Optical Properties of Series Fountain B

As already mentioned in 4.4.3, the optical properties are investigated by CL and infrared absorption measurements. In this chapter, I will give a short summary of the optical properties of the second series of fountain laser structures (fountain B). The variations in layer thicknesses as well as the different doping concentrations as a consequence of the previous results will shortly be discussed while the improvement compared to series fountain A will be clearly accentuated.

The structural properties of series fountain B samples are given in Table 5 and have been obtained similarly to series A. The thickness of the AlN barriers has been slightly increased to 3 nm in order to avoid coupling between the adjacent ACQWs. The number of periods has been decreased to 40 which is a compromise between growth issues and interaction volume. Furthermore, a better comparability to previously grown superlattice samples containing only 40 periods as well (see e.g. chapter 4.1) is ensured. The thickness of the AlN tunnelling barrier is kept constant to ensure better comparability between series B samples. In order to show the possible tunability of the e3-e2 transition energy and to ensure that e2 state is unpopulated due to a larger distance to e1, the thickness of GaN2 is varied between 1.9 nm and 0.7 nm. As a result from the observed double absorptions in series A, the doping concentration in GaN1 is decreased by one order of magnitude to 1e19 cm^{-3}.

Fig. 58 shows the room temperature CL spectrum of sample fountain B5 having its maximum intensity around 3.6 eV. The arrows indicate calculated interband transitions between the first electron state e1 and the first heavy hole (hh1) for relaxed GaN QWs (blue) and QWs fully strained on AlN barriers. The acceleration voltage was 5 kV for this measurement which is lower than for the first series. This is due to the smaller thickness of the sample which requires a smaller penetration depth. Furthermore, the CL data of series fountain B are very similar to series fountain A giving proof of the reproducibility

of ACQW samples, because the IBT is mainly influenced by the GaN1 thickness which is comparable for series A and B.
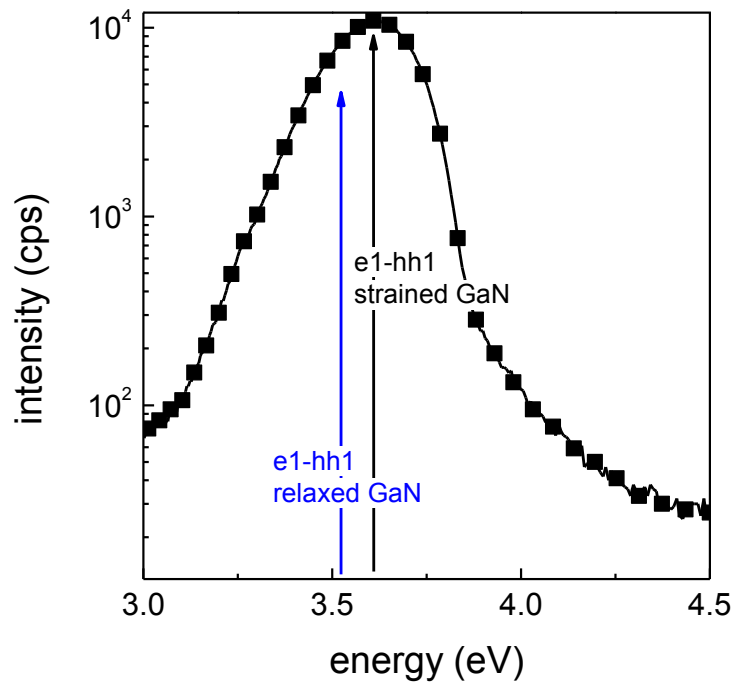
Fig. 58: Room temperature CL spectrum of sample fountain B5. Arrows indicate calculated interband transitions for fully relaxed GaN QWs and strained AlN barriers (blue) and for fully strained GaN QWs on relaxed AlN barriers (black).

In the following I will show the infrared absorption data of series fountain B samples measured using FTIR. Again all samples show clear polarization dependent absorption giving proof of the intersubband origin of these absorptions. Compared to the first series of ACQW samples, no double absorptions are observed which means that the lower doping concentration successfully kept the e1 state occupied, while e2 stays unoccupied. Fig. 59 and Fig. 60 show the transmission through the waveguide for samples B1 and B2. Clear absorption is found for TM polarized light around 0.7 eV. The maximum of the absorption is not shifted between these two samples due to the constant GaN1 thickness which mainly influences the e1-e3 transition observed here. A more detailed investigation of the influences of transition energy and QW thickness is already given in 4.4.1. The FWHM of the absorptions is around 250 meV for all samples and can be explained by layer thickness fluctuations. As I have shown in 4.4.1, a fluctuation of one of the QWs can result in a 100 meV shift of the transition energy (see Fig. 49 and Fig. 50) and even using MBE a thickness fluctuation of one ML over such a multilayer system cannot be excluded.
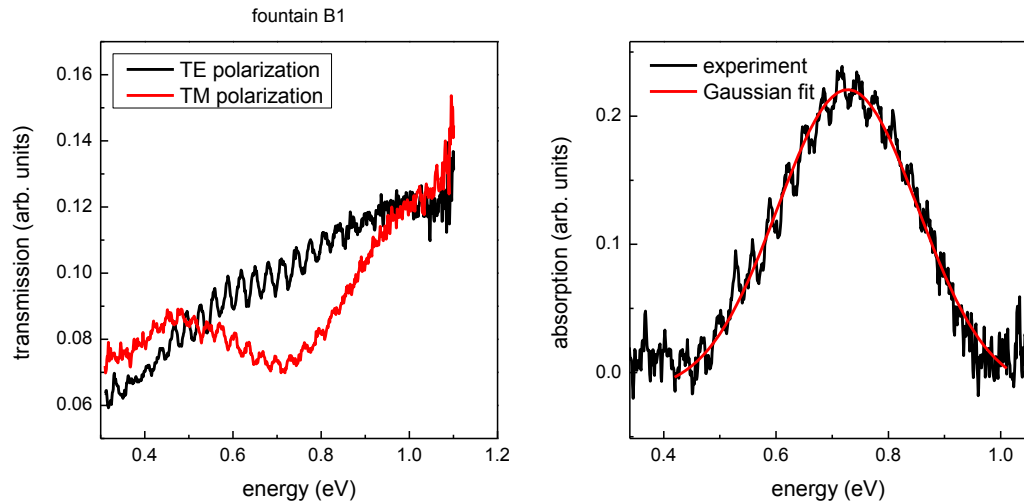
Fig. 59: Transmission through sample fountain B1 for TE and TM polarization. Clear absorption is found for TM polarization around 0.7 eV (left hand diagram). Resulting absorption spectrum with Gaussian fit (right hand diagram). The FWHM of the absorption peak is about 250 meV.
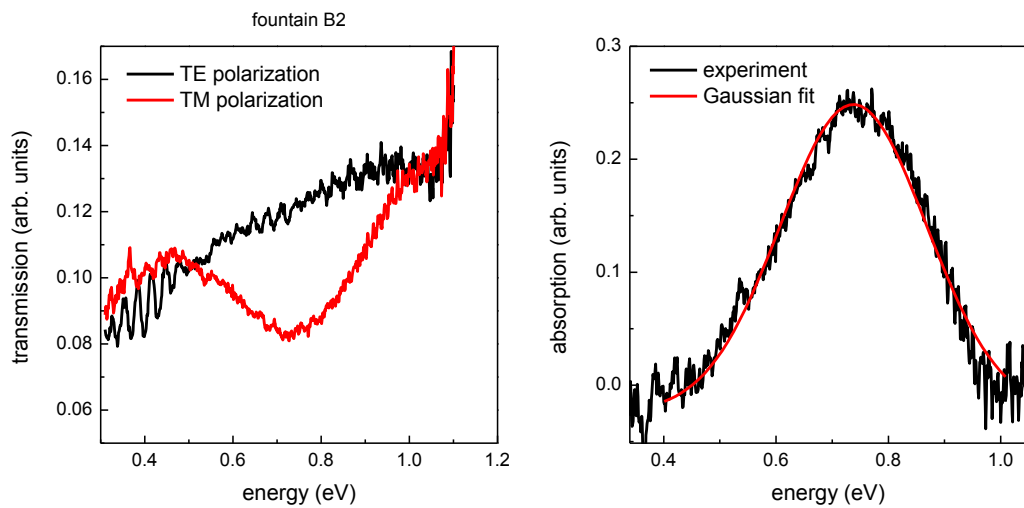
Fig. 60: Transmission through sample fountain B2 for TE and TM polarization. Clear absorption is found for TM polarization 0.7 eV (left hand diagram). Resulting absorption spectrum with Gaussian fit (right hand diagram). The FWHM of the absorption peak is about 250 meV.

4.4.7 Conclusions for Series Fountain B

In summary, I have shown that the improvements proposed in 4.4.5 for the second series of samples have been successfully realized. The fixed GaN1 thickness leads to an e1-e3 absorption energy which is constant at about 0.7 eV. Due to the reduced doping concentration no double absorptions are observed giving proof that the second electron state e2 remains unoccupied which is crucial for further measurements as well as future sample design. The next step will be to perform a first measurement of light emission which could not be realized in this work. Nevertheless, clear polarization dependent infrared absorption has been measured in cubic AlN/GaN ACQW samples for the first time. For future superlattice samples the thickness of the structure of the samples should be modified by means of the calculations in chapter 4.4.1 to reach the optical telecommunication spectral range.

5 Summary and Outlook

In my work I have studied the physics of Al(Ga)N/GaN quantum wells, multi-quantum-wells and superlattices. In order to realize a sophisticated unipolar device like a quantum cascade laser, a lot of physical effects have to be studied and a lot of challenges have to be overcome. I have shown the possibility of resonant tunneling through Al(Ga)N/GaN double barrier structures with clear recoverable negative differential resistance. Peak-to-valley ratios from 2.7-1.3 could be achieved. Furthermore, I have investigated the tunability of intersubband transition energies in Al(Ga)N/GaN multi-quantum-wells and superlattices reaching from 20 meV to 900 meV representing the highest and lowest transition energy published in this material system up to now. The transition energy was changed by the variation of different parameters like the quantum well thickness, the barrier thickness and the height of the barrier.

Using high resolution X-ray diffraction, model calculations and transmission electron microscopy it was possible to characterize the structural properties of such superlattices. Using the knowledge of these structural properties it was possible to estimate the thicknesses of single layers with an accuracy of ±1 monolayer. Besides the layer thickness it was shown by transmission electron microscopy that a significant roughness induced by the relaxation process of GaN on 3C-SiC does not influence the superlattice structure in a negative way. The multi layer structure covers the roughness like a piece of cloth forming an undulated structure.

Moreover, I have determined the so far unknown band offset in AlN/GaN superlattices. Studying the optical properties by photoluminescence- and absorption-spectroscopy and comparing it to nextnano³ calculations it was possible to set limits for the conduction- and valence band offset between GaN and AlN. In cooperation with the theoretical physics group of Professor W.G. Schmidt, who has studied the band offset using state-of-the art hybrid functional density functional theory calculations, we have managed to prove the experimental results. We conclude that our comprehensive experimental and theoretical results give strong evidence for a conduction band offset of (1.4±0.1) eV and a valence band offset of (0.5±0.1) eV in cubic AlN/GaN superlattice structures. These results apply for superlattice structures where, due to the periodicity, the indirect band gap of AlN with 5.3 eV has to be considered. Furthermore, strain conditions and the resulting band gap energy variations have to be taken into account. In conclusion, a conduction band offset to valence band offset ratio of (74:26) % of the band gap energy difference with and accuracy of ±5 % was found.

Moreover, I have investigated asymmetric coupled multi-quantum-wells as a potential basis for optically pumped lasers or quantum fountain lasers. The main

challenges for a future fountain laser system are the accurate adjustment of the Fermi level to occupy the ground state while the first excited state remains unoccupied and the sensitive setting of the energy difference between the first two localized states in the order of a LO-phonon. The first challenge has been leading to double absorptions in series fountain A. The doping concentration has therefore been readjusted and this obstacle has been overcome.

Furthermore, the development of asymmetric coupled quantum wells has to be continued. In my work I have shown the possibilities to realize a light emitting device in the technologically interesting 1.55 μm range. One of the main challenges in group-III nitrides is still the large misfit between 3C-SiC and GaN and, as a consequence of the relaxation process, the large dislocation density. The relaxation process could be changed by using an AlGaN buffer layer with a graded Al content where the strain can be reduced gradually. Another possibility to reduce the dislocation density may be the use of nanoheteroepitaxy which is also investigated in our group and shows some promising results [74].

6 Appendix

6.1 Superlattice Growth without GaN Buffer

In this chapter, I want to show first results of improved AlN/GaN SL structures grown directly on 3C-SiC without any GaN buffer layer. For this reason, I have grown two equal superlattice structures containing 100 periods of 4 nm GaN QWs with 2 nm AlN barriers. For sample A the SL is grown on a 50 nm GaN buffer layer and for sample B the SL is grown directly on the 3C-SiC substrate. After growth both samples were characterized by HRXRD and PL. Results will be discussed in the following.

6.2 Structural Properties

To investigate the structural properties of the two different SL samples I have performed HRXRD. Fig. 61 shows the reciprocal space maps of sample A on the left hand side and B on the right hand side. In both cases clear SL satellites are observed. From the position of the satellites a slightly different strain status of the SL is observed. Sample A is 45 % strained on AlN and sample B 51 %. For sample A, besides the SL satellites, a clear contribution of the GaN buffer layer is found, smearing out the SL satellite next to the theoretical value of relaxed c-GaN. This contribution is not observed for sample B where only SL satellites appear. The SL satellites of sample B show broadening compared to sample A which can be an indicator for an increased dislocation density, but has to be investigated further before drawing a final conclusion.
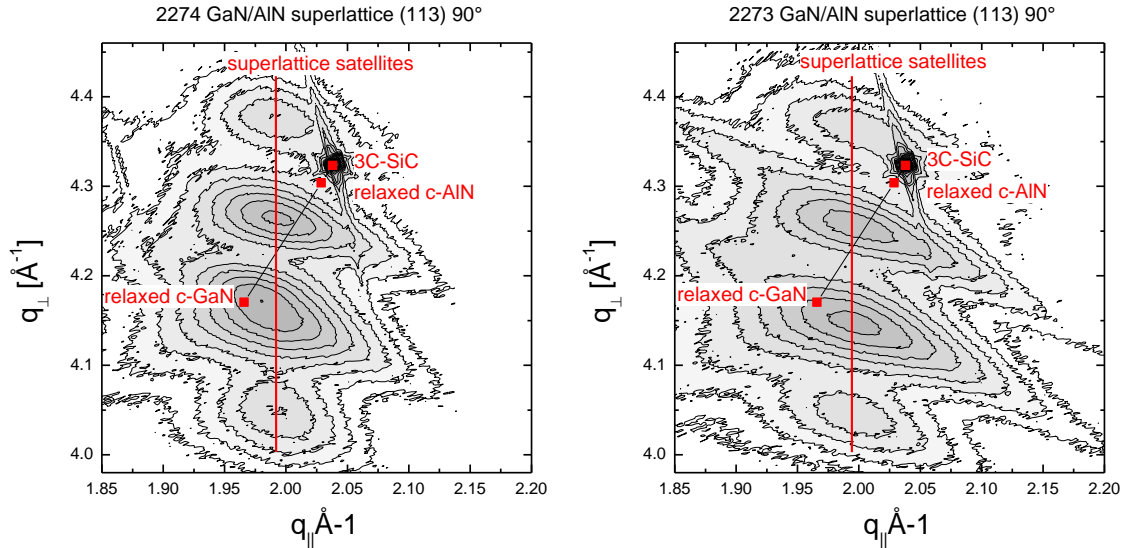
Fig. 61: Reciprocal space maps of the asymmetric (113) reflection of sample A (left hand) and sample B (right hand). In both cases clear SL satellites are observed. From the position of the satellites a slightly different strain status of the SL is observed. Sample A is 45 % strained on AlN and sample B 51 %.

6.3 Optical Properties

The optical properties of the two samples are investigated using PL. The samples are illuminated by a HeCd laser while a room temperature photoluminescence spectrum is recorded. The PL spectra of both samples are shown in Fig. 62. The spectrum of sample A is represented by the red line while the spectrum of sample B is represented by the black line. Both samples show clear luminescence around 3.4 eV which can be assigned to the superlattice. The emission band maximum of sample B is slightly red shifted in comparison to sample A. The difference between the maxima is 40 meV. This shift may be due to thinner QWs in the superlattice, which may be due to slightly different growth rates, although the samples were grown on subsequent days. However a much more remarkable result is that the FWHM of the luminescence of sample B is considerably smaller than the FWHM of the emission of sample A. The difference in FWHM is in the order of 50 meV which can be seen as an indicator for a better structural quality. The smaller FWHM is an indicator for a higher crystalline quality of sample B. Another indicator for a better quality of sample B is the lower intensity of the emission band located at 2-2.5 eV which is known as red luminescence in cubic GaN while the intensity of the peak is higher. The ratio of the red luminescence intensity divided by the intensity of the band edge luminescence is $1.4 \cdot 10^{-3}$ for sample B without the GaN buffer and $2.7 \cdot 10^{-3}$ for sample A with the 50 nm GaN buffer and thereby two times lower for sample B. All these results are just hints and have to be confirmed by further experiments.
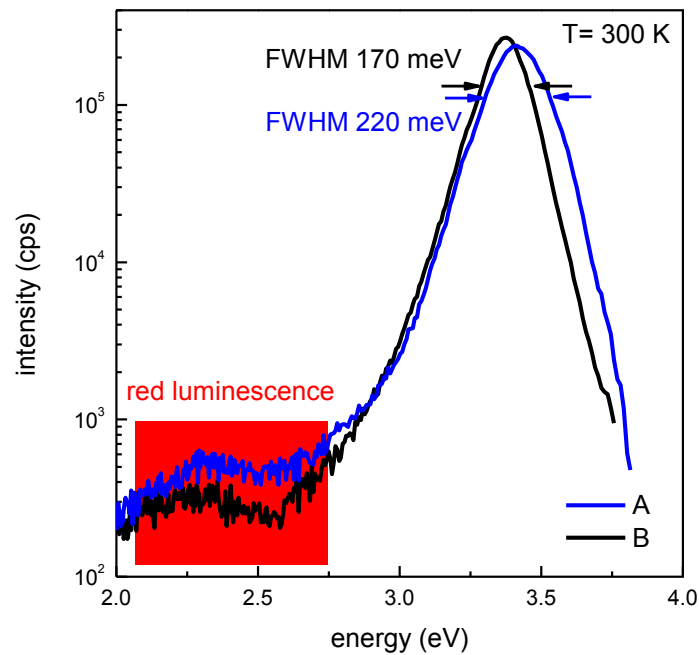
Fig. 62: Room temperature PL spectra of samples A (red line) and B (black line). Both samples show clear luminescence around 3.4 eV which can be assigned to the superlattice.

In summary, I have presented superlattice structures grown without a GaN buffer layer. While X-ray measurements seem to show no improvement the photoluminescence data looks promising for a possible improvement, for future superlattice growth. The full width at half maximum of the emission peak was explicitly reduced while the intensity was comparable or slightly higher than with a GaN buffer for comparable superlattices. This effect has to be investigated further in future works.

6.4 Abstract of the nextnano Material File Dealing with III-Nitrides

6.4.1 Cubic GaN Material Parameters

In the following the material parameters of cubic GaN are shown. The most important values that I have varied for e.g. the band offset calculations are highlighted in yellow. The conduction band has to be taken into account for exact calculations of thin QWs, because the effective electron mass differs from the bulk values for thin QWs. Furthermore, the conduction and valence band energies are important for a variation of band offset or band gap energy.

```
!----------------------------------------------------------------------!
! GaN (zincblende) --- Source: Vurgaftman et al., J. Appl. Phys. 89 (11), 5815 (2001)
!                 Vurgaftman et al., J. Appl. Phys. 96 ( 6), 3675 (2003)
! S. Birner
!----------------------------------------------------------------------!
 $binary-zb-default                        !
  binary-type              = GaN(zb)-zb-default       !
  conduction-bands         = 3              ! total number of conduction bands
possible
                                            values > 0.0 [m0]. 3 numbers per
                                            band; numbers corresponds to band
                                            no. 1, 2, ...
  conduction-band-masses       = 0.132d0   0.132d0   0.132d0   ! Gamma
Vurgaftman1,
                                      Vurgaftman2  cb1 - 1st principal axis,
                                   2nd, 3rd
                             0.2d0   0.2d0   0.2d0   ! ??? L   cb2 - 1st
principal axis,
                                                   2nd, 3rd - m_l m_t
                                   m_t
                             0.5d0   0.3d0   0.3d0 ! X
Vurgaftman1/Vurgaftman2
                                        cb3 - 1st principal axis, 2nd,
                                   3rd –
                                   m_l m_t m_t
  conduction-band-degeneracies    = 2    8    6       ! including spin degeneracy
  conduction-band-nonparabolicities  = 0.213d0 0d0    0d0     ! (Where does this
value come from? Shur website?) As used in a hyperbolic dispersion k^2 ~ E(1+aE). a =
nonparabolicity [1/eV]
  conduction-band-energies       = 2.579d0 4.870d0 3.800d0    ! 0K
Vurgaftman1, Vurgaftman2  conduction band edge energies relative to valence band
number 1 (number corresponds
  !conduction-band-energies      = 2.504d0 4.811d0 3.741d0    ! 300K
Vurgaftman1/Vurgaftman2  conduction band edge energies relative to valence band
number 1 (number corresponds to the ordering of the entries below
  valence-bands            = 3              ! total number of valence bands
```

```
    valence-band-masses              = 1.3d0   1.3d0   1.3d0        ! hh
http://www.ioffe.rssi.ru/SVA/NSM/Semicond/GaN/bandstr.html Leszczynski et al.
(1996), Fan et al. (1996)
                                     0.19d0  0.19d0  0.19d0      ! lh
http://www.ioffe.rssi.ru/SVA/NSM/Semicond/GaN/bandstr.html Leszczynski et al.
(1996), Fan et al. (1996)
                                     0.29d0  0.29d0  0.29d0    ! split-off
Vurgaftman1/Vurgaftman2
    valence-band-degeneracies        = 2      2      2          ! including spin degeneracy
    valence-band-nonparabolicities   = 0.0d0   0.0d0   0.0d0       ! As used in a
hyperbolic dispersion k^2 ~ E(1+aE). a = nonparabolicity [1/eV]
    valence-band-energies            = -0.726d0               ! A. Zunger, average valence
band energy E_v,av [eV]
    varshni-parameters               = 0.593d-3 0.593d-3 0.593d-3    ! alpha
[eV/K](Gamma, L, X) Vurgaftman1/Vurgaftman2
                                     600d0   600d0   600d0      ! beta  [K]  (Gamma, L, X)
Vurgaftman1/Vurgaftman2
    static-dielectric-constants      = 9.7d0   9.7d0   9.7d0       !
http://www.ioffe.rssi.ru/SVA/NSM/Semicond/GaN/optic.html Bougrov et al. (2001)
(300 K)
    optical-dielectric-constant      = 5.3d0                  ! high frequency (300 K)
    band-shift                       = 0d0                  ! to adjust band alignments (should be
zero in database): adds to all band energies
    absolute-deformation-potential-vb  = 0.69d0                  ! a_v [eV] Zunger
    !absolute-deformation-potential-vb   = 0.69d0                   ! a_v [eV] Vurgaftman2
has different sign convention -> -0.69
    !absolute-deformation-potential-vb   = 5.2d0                    ! a_v [eV] Vurgaftman1
has different sign convention -> -5.2
    !absolute-deformation-potentials-cbs = -2.2d0   -7.46d0  -0.52d0     ! Vurgaftman1
(Gamma) / Zunger - absolute deformation potentials of conduction band minima a_cd ,
a_ci's
    !absolute-deformation-potentials-cbs = -6.71d0  -7.46d0  -0.52d0     ! Vurgaftman2
(Gamma) / Zunger - absolute deformation potentials of conduction band minima a_cd ,
a_ci's
    absolute-deformation-potentials-cbs = -6.68d0  -7.46d0  -0.52d0     ! Zunger -
absolute deformation potentials of conduction band minima a_cd , a_ci's
    !uniax-vb-deformation-potentials    = -2.2d0   -3.4d0            ! b,d [eV]  Vurgaftman1
    uniax-vb-deformation-potentials     = -2.0d0   -3.7d0            ! b,d [eV]  Vurgaftman2
    uniax-cb-deformation-potentials   = 0d0      14.26d0   8.61d0       ! [eV] ? no idea, I
took GaAs values, Xi_u(at minimum)
    lattice-constants                = 0.452d0  0.452d0  0.452d0    ! [nm]
Vurgaftman1/Vurgaftman2  300 K
    lattice-constants-temp-coeff     = 0d0     0d0     0d0         ! [nm/K]
    elastic-constants                = 293d0    159d0   155d0      ! c11, c12, c44
Vurgaftman1/Vurgaftman2
    piezo-electric-constants         = 0d0      0d0     0.56d0     ! -,-,e14 [C/m^2] taken
from M. Shur http://nina.ecse.rpi.edu/shur/Tutorial/GaNtutorial1/sld038.htm
```

```
    !Luttinger-parameters         = 2.67d0   0.75d0   1.10d0   ! gamma1, gamma2,
gamma3 - [Vurgaftman1]
    Luttinger-parameters          = 2.70d0   0.76d0   1.11d0  0d0 0d0 ! gamma1,
gamma2, gamma3 - [Vurgaftman2]
    !6x6kp-parameters             = -6.67d0  -2.17d0  -6.60d0   ! Vurgaftman1  L,M,N
[hbar^2/2m] (--> divide by hbar^2/2m)
    6x6kp-parameters              = -6.74d0  -2.18d0  -6.66d0   ! Vurgaftman2  L,M,N
[hbar^2/2m] (--> divide by hbar^2/2m)
                        0.017d0                  ! Vurgaftman1/Vurgaftman2 delta_(split-
off) in [eV]
    ! Eg=3.299                                  ! Vurgaftman1/Vurgaftman2
    !8x8kp-parameters             = 0.895d0 -2.17d0   0.965d0   ! Vurgaftman1  L',M,N'
[hbar^2/2m] (--> divide by hbar^2/2m)
    8x8kp-parameters              = 0.825d0 -2.18d0   0.905d0   ! Vurgaftman2  L',M,N'
[hbar^2/2m] (--> divide by hbar^2/2m)
                        0.0d0    25.0d0  -0.898d0   ! Vurgaftman2  B [hbar^2/2m], E_P
[eV], S [-]
    !                 0.0d0    25.0d0  -0.90d0    ! Vurgaftman2  B [hbar^2/2m], E_P
[eV], S [-] (S = 1 + 2F = 1 + 2 (-0.95) = -0.90) [Vurgaftman2]
    !                 0.0d0    25.0d0  -0.84d0    ! Vurgaftman1  B [hbar^2/2m], E_P
[eV], S [-] (S = 1 + 2F = 1 + 2 (-0.92) = -0.84) [Vurgaftman1]
    !rescaled parameters S=1                        ! Vurgaftman1/Vurgaftman2
    !8x8kp-parameters             = -1.0034d0 -2.170d0 -0.933d0 ! Vurgaftman1
L',M,N' [hbar^2/2m] (--> divide by hbar^2/2m)
    !8x8kp-parameters             = -1.0073d0 -2.170d0 -0.993d0 ! Vurgaftman2
L',M,N' [hbar^2/2m] (--> divide by hbar^2/2m)
    !                 0.0d0    18.726d0   1.0d0 ! Vurgaftman1/Vurgaftman2   B
[hbar^2/2m], E_P [eV], S [-]
    LO-phonon-energy              = 0.091d0 ! GaN wurtzite value!! ! [eV] J. Piprek (300
K)
    number-of-minima-of-cband      = 1 4 3                 !
    conduction-band-minima        = 0d0     0d0     0d0     ! components of k-vector
along crystal xyz [k0]
                      0.866d0  0.866d0  0.866d0   ! L1  1 1 1
                      0.866d0  0.866d0 -0.866d0   ! L2  1 1-1
                     -0.866d0  0.866d0  0.866d0   ! L3 -1 1 1
                     -0.866d0  0.866d0 -0.866d0   ! L4 -1 1-1
                                     !
                      1.000d0  0d0     0d0       ! X1  100
                      0d0     1.000d0  0d0       ! X2  010
                      0d0     0d0     1.000d0   ! X3  001
                                     !
    principal-axes-cb-masses       = 1.000d0  0d0     0d0      ! Normalization will be
done internally by the program
                      0d0     1.000d0  0d0     !
                      0d0     0d0     1.000d0  !
                                     !
```

```
                    1.000d0  1.000d0  1.000d0  ! L1 -> ml -  1 1 1
                    1.000d0 -1.000d0  0d0      !
                    1.000d0  1.000d0 -2.000d0  !
                    1.000d0  1.000d0 -1.000d0  ! L2 -> ml -  1 1-1
                    1.000d0 -1.000d0  0d0      !
                   -1.000d0 -1.000d0 -2.000d0  !
                   -1.000d0  1.000d0  1.000d0  ! L3 -> ml -  -1 1 1
                    1.000d0  1.000d0  0d0      !
                   -1.000d0  1.000d0 -2.000d0  !
                   -1.000d0  1.000d0 -1.000d0  ! L4 -> ml -  -1 1-1
                    1.000d0  1.000d0  0d0      !
                    1.000d0 -1.000d0 -2.000d0  !
                                     !
                    1.000d0  0d0      0d0      ! X1 -> ml - 100
                    0d0      1.000d0  0d0      !
                    0d0      0d0      1.000d0  !
                    0d0     -1.000d0  0d0      ! X2 -> ml - 010
                    0d0      0d0     -1.000d0  !
                    1.000d0  0d0      0d0      !
                    0d0      0d0      1.000d0  ! X3 -> ml - 001
                    1.000d0  0d0      0d0      !
                    0d0      1.000d0  0d0      !
                                     !
  number-of-minima-of-vband      = 1 1 1             !
  valence-band-minima         = 0d0    0d0     0d0     ! components of k-vector
along crystal xyz [k0]
                    0d0     0d0      0d0      !
                    0d0     0d0      0d0      !
                                     !
  principal-axes-vb-masses     = 1.000d0  0d0     0d0      ! Normalization will be
done internally by the program
                    0d0      1.000d0  0d0      !
                    0d0      0d0      1.000d0  !
                    1.000d0  0d0      0d0      !
                    0d0      1.000d0  0d0      !
                    0d0      0d0      1.000d0  !
                    1.000d0  0d0      0d0      !
                    0d0      1.000d0  0d0      !
                    0d0      0d0      1.000d0  !
  $end_binary-zb-default                    !
  !----------------------------------------------------------------!
```

6.4.2   Cubic AlN Material Parameters

In this parameter set I highlighted the values which I have varied for band offset calculations. It is very important to use the correct band offset values for the desired application. For superlattice calculations the indirect band gap of AlN has to be used while for resonant tunneling diodes the direct band gap of AlN has to be used (see below).

```
!-------------------------------------------------------------------!
! AlN (zincblende) --- Source: Vurgaftman et al., J. Appl. Phys. 89 (11), 5815 (2001)
!                      Vurgaftman et al., J. Appl. Phys. 96 ( 6), 3675 (2003)
! S. Birner
!-------------------------------------------------------------------!
$binary-zb-default                              !
 binary-type                 = AlN(zb)-zb-default        !
 conduction-bands            = 3                 ! total number of conduction bands
possible values > 0.0 [m0]. 3 numbers per band; numbers corresponds to band no. 1, 2,
...
    conduction-band-masses      = 0.28d0   0.28d0   0.28d0   ! Gamma
Vurgaftman1/Vurgaftman2  cb1 - 1st principal axis, 2nd, 3rd
                              0.2d0   0.2d0   0.2d0   ! ??? L  cb2 - 1st
principal axis, 2nd, 3rd - m_l m_t m_t
                              0.53d0   0.31d0   0.31d0   ! X
Vurgaftman1/Vurgaftman2  cb3 - 1st principal axis, 2nd, 3rd - m_l m_t m_t
    conduction-band-degeneracies    = 2      8      6       ! including spin degeneracy
    conduction-band-nonparabolicities  = 0d0     0d0     0d0      ! As used in a
hyperbolic dispersion k^2 ~ E(1+aE). a = nonparabolicity [1/eV]
    !conduction-band-energies        = 3.979d0  7.780d0  3.380d0     !  indirect gap for
SL calculations CBO 1.4 eV Eg=5.255 eV (Goldhahn)
    conduction-band-energies         = 4.624d0  7.721d0  3.321d0       ! direct gap Eg=5.9
eV (Goldhahn)
    !conduction-band-energies        = 4.480d0  7.780d0  3.380d0    !  0K  Vurgaftman1
conduction band edge energies relative to valence band number 1 (number corresponds
    !conduction-band-energies        = 4.421d0  7.721d0  3.321d0      ! 300K
Vurgaftman1  conduction band edge energies relative to valence band number 1
(number corresponds to the ordering of the entries below
    valence-bands               = 3                 ! total number of valence bands
    valence-band-masses          = 1.2d0  1.2d0  1.2d0     ! ???  possible values > 0.0
[m0]. Ordering of numbers corresponds to band no. 1, 2, ...
                    0.3d0  0.3d0  0.3d0     ! ???
                      0.47d0  0.47d0  0.47d0     ! split-off
Vurgaftman1/Vurgaftman2
    valence-band-degeneracies       = 2      2      2       ! including spin degeneracy
    valence-band-nonparabolicities    = 0.0d0    0.0d0    0.0d0       ! As used in a
hyperbolic dispersion k^2 ~ E(1+aE). a = nonparabolicity [1/eV]
    valence-band-energies           = -1.276d0                 ! A. Zunger, average valence
band energy E_v,av [eV]
    varshni-parameters          = 0.593d-3 0.593d-3 0.593d-3    ! alpha
[eV/K](Gamma, L, X) Vurgaftman1/Vurgaftman2
```

```
                    600d0   600d0   600d0      ! beta  [K]   (Gamma, L, X)
Vurgaftman1/Vurgaftman2
     static-dielectric-constants       = 9.14d0   9.14d0  9.14d0  ! ??? Landolt-Boernstein
epsilon(0)     wurtzite, Collins et al. (1967)
     optical-dielectric-constant       = 4.84d0               ! ??? Landolt-Boernstein
epsilon(infinity) wurtzite, Collins et al. (1967)
     band-shift            = 0d0                ! to adjust band alignments (should be
zero in database): adds to all band energies
     absolute-deformation-potential-vb  = 4.94d0              ! a_v [eV] Zunger
     !absolute-deformation-potential-vb  = 4.9d0              ! a_v [eV] Vurgaftman2
has different sign convention -> -4.9
     !absolute-deformation-potential-vb  = 3.4d0              ! a_v [eV] Vurgaftman1
has different sign convention -> -3.4
     !absolute-deformation-potentials-cbs = -6.0d0  -4.95d0 3.81d0    ! Vurgaftman1
(Gamma) / Zunger - absolute deformation potentials of conduction band minima a_cd ,
a_ci's
     !absolute-deformation-potentials-cbs = -4.5d0  -4.95d0 3.81d0    ! Vurgaftman2
(Gamma) / Zunger - absolute deformation potentials of conduction band minima a_cd ,
a_ci's
     absolute-deformation-potentials-cbs = -5.22d0 -4.95d0 3.81d0    ! Zunger
- absolute deformation potentials of conduction band minima a_cd , a_ci's
     !uniax-vb-deformation-potentials    = -1.9d0   -10d0        ! b,d [eV]  Vurgaftman1
     uniax-vb-deformation-potentials    = -1.7d0   -5.5d0        ! b,d [eV]  Vurgaftman2
     uniax-cb-deformation-potentials    = 0d0     14.26d0 8.61d0    ! [eV] ? no idea, I
took GaAs values, Xi_u(at minimum)
     lattice-constants     = 0.4373d0  0.4373d0  0.4373d0   ! [nm]
Vurgaftman1/Vurgaftman2  300 K
     lattice-constants-temp-coeff      = 0d0     0d0     0d0       ! [nm/K]
     elastic-constants           = 304d0    160d0    193d0    ! c11, c12, c44
Vurgaftman1/Vurgaftman2
     piezo-electric-constants       = 0d0     0d0     0.92d0   ! ? -, -, e14 [C/m^2] taken
from Shur http://nina.ecse.rpi.edu/shur/Tutorial/GaNtutorial1/sld038.htm (wurtzite)
     Luttinger-parameters       = 1.92d0   0.47d0   0.85d0 0d0 0d0  ! gamma1,
gamma2, gamma3 - [Vurgaftman1/Vurgaftman2]
     6x6kp-parameters          = -4.80d0  -1.98d0  -5.10d0   !
Vurgaftman1/Vurgaftman2  L,M,N   [hbar^2/2m] (--> divide by hbar^2/2m)
                     0.019d0              ! Vurgaftman1/Vurgaftman2  delta_(split-
off) in [eV]
     ! Eg=5.9 direct (ERROR in Vurgaftman1 paper!)             ! Vurgaftman1
     ! Eg=5.3 indirect                            ! Vurgaftman2
     !8x8kp-parameters          = -0.288d0 -1.98d0  -0.588d0  ! Vurgaftman1
L',M,N' [hbar^2/2m] (--> divide by hbar^2/2m)
     !                 0.0d0   27.1d0   -0.512d0  ! Vurgaftman1    B [hbar^2/2m],
E_P [eV], S [-]
     !                 0.0d0   27.1d0   -0.52d0  ! Vurgaftman1       B
[hbar^2/2m], E_P [eV], S [-] (S = 1 + 2F = 1 + 2 (-0.76) = -0.52) [Vurgaftman1]
```

```
     8x8kp-parameters                = 0.213d0  -1.98d0   -0.087d0  ! Vurgaftman2
L',M,N' [hbar^2/2m] (--> divide by hbar^2/2m)
                           0.0d0    27.1d0   -1.013d0  ! Vurgaftman2     B [hbar^2/2m],
E_P [eV], S [-]
     !                     0.0d0    27.1d0   -1.02d0   ! Vurgaftman2         B
[hbar^2/2m], E_P [eV], S [-] (S = 1 + 2F = 1 + 2 (-1.01) = -1.02) [Vurgaftman2]
     !rescaled parameters S=1                         !
     !8x8kp-parameters                = -1.800d0  -1.980d0  -2.100d0  !
Vurgaftman1/Vurgaftman2  L',M,N' [hbar^2/2m] (--> divide by hbar^2/2m)
     !                     0.0d0    16.219d0  1.0d0   ! Vurgaftman2   B [hbar^2/2m],
E_P [eV], S [-]
     !!                    0.0d0    18.019d0  1.0d0   ! Vurgaftman1    B [hbar^2/2m],
E_P [eV], S [-]
     LO-phonon-energy              = 0.110d0 ! AlN wurtzite value!! ! [eV] J. Piprek (300 K)
     number-of-minima-of-cband       = 1 4 3              !
     conduction-band-minima        = 0d0     0d0      0d0      ! components of k-vector
along crystal xyz [k0]
                     0.866d0  0.866d0  0.866d0  ! L1  1 1 1
                     0.866d0  0.866d0  -0.866d0  ! L2  1 1-1
                    -0.866d0  0.866d0  0.866d0  ! L3 -1 1 1
                    -0.866d0  0.866d0  -0.866d0  ! L4 -1 1-1
                                     !
                     1.000d0  0d0     0d0      ! X1  100
                     0d0     1.000d0  0d0      ! X2  010
                     0d0     0d0     1.000d0  ! X3  001
     principal-axes-cb-masses       = 1.000d0  0d0     0d0      ! Normalization will be
done
                                       internally by the program
                     0d0     1.000d0  0d0     !
                     0d0     0d0     1.000d0  !
                     1.000d0  1.000d0  1.000d0  ! L1 -> ml -  1 1 1
                     1.000d0  -1.000d0  0d0     !
                     1.000d0  1.000d0  -2.000d0  !
                     1.000d0  1.000d0  -1.000d0  ! L2 -> ml -  1 1-1
                     1.000d0  -1.000d0  0d0     !
                    -1.000d0  -1.000d0  -2.000d0  !
                    -1.000d0  1.000d0  1.000d0  ! L3 -> ml -  -1 1 1
                     1.000d0  1.000d0  0d0     !
                    -1.000d0  1.000d0  -2.000d0  !
                    -1.000d0  1.000d0  -1.000d0  ! L4 -> ml -  -1 1-1
                     1.000d0  1.000d0  0d0     !
                     1.000d0  -1.000d0  -2.000d0  !
                     1.000d0  0d0     0d0      ! X1 -> ml - 100
                     0d0     1.000d0  0d0     !
                     0d0     0d0     1.000d0  !
                     0d0     -1.000d0  0d0     ! X2 -> ml - 010
                     0d0     0d0     -1.000d0  !
```

```
                    1.000d0  0d0     0d0     !
                    0d0      0d0     1.000d0 ! X3 -> ml - 001
                    1.000d0  0d0     0d0     !
                    0d0      1.000d0 0d0     !
    number-of-minima-of-vband        = 1 1 1              !
    valence-band-minima       = 0d0     0d0     0d0 ! components of k-vector along
crystal xyz [k0]
                    0d0      0d0     0d0     !
                    0d0      0d0     0d0     !
    principal-axes-vb-masses        = 1.000d0  0d0     0d0     ! Normalization will be
done
                                                     internally by the program
                    0d0      1.000d0 0d0     !
                    0d0      0d0     1.000d0 !
                    1.000d0  0d0     0d0     !
                    0d0      1.000d0 0d0     !
                    0d0      0d0     1.000d0 !
                    1.000d0  0d0     0d0     !
                    0d0      1.000d0 0d0     !
                    0d0      0d0     1.000d0 !
    $end_binary-zb-default                        !
```

6.5   nextnano³ Input File for a AlN/GaN Superlattice

In the following I have copied the source code for AlN/GaN superlattice calculations exemplarily. It is mainly based on the example file 1D_simple_GaAs_QW by Stefan Birner including some changes to make It suitable for our material system and superlattice calculations. The text which is relevant for the calculation is black while comments are coloured in light blue.

```
!******             OVERALL           SIMULATION           PARAMETERS
*************************************!

  !----------------------------------------------------------------------!
  $numeric-control                                      !
  simulation-dimension  = 1                          ! only simulate directions in
  which charge
                                                 carriers   are   bound,   therefore   1D
                                          simulation
                                          for a quantum well
   zero-potential        = yes                                 ! don't consider charge
  redistribution
   varshni-parameters-on = yes              ! consider temperature dependence of
  band gap
    $end_numeric-control                                !
  !----------------------------------------------------------------------!

  !----------------------------------------------------------------------!
  $simulation-dimension                              !
   dimension  = 1                             ! 1D simulation
   orientation = 0 0 1                          ! along z axis (as defined below)
  $end_simulation-dimension                          !
  !----------------------------------------------------------------------!

  !----------------------------------------------------------------------!
  $global-parameters                            !
   lattice-temperature = 300d0                          ! 300 Kelvin
  $end_global-parameters                          !
  !----------------------------------------------------------------------!

  !----------------------------------------------------------------------!
  $simulation-flow-control                          !
   flow-scheme       = 3   ! solve Schroedinger equation only (because no charge
  redistribution here)
   raw-directory-in   = raw_data1/                      !
   raw-potential-in   = no                      !
   strain-calculation  = zero-strain-amorphous                ! don't consider strain
    $end_simulation-flow-control                          !
```

```
!----------------------------------------------------------------------!

!----------------------------------------------------------------------!
$domain-coordinates                                    !
 domain-type          = 0 0 1                          ! again: along z axis
 z-coordinates        = 0d0 8.0d0                      ! beginning and end of simulated
region in nm
 growth-coordinate-axis = 0 0 1                        ! needed if pseudomorphic strain is to
be calculated
 pseudomorphic-on      = SiC(zb)                       ! needed if pseudomorphic strain is to
be calculated
$end_domain-coordinates                                !
!----------------------------------------------------------------------!
!******REGIONS AND CLUSTERS****************************!
!----------------------------------------------------------------------!
$regions                                          !
 region-number = 1   base-geometry = line   region-priority = 1      ! First fill whole
simulation
                                                            region   with   AlN
                                             barrier
   z-coordinates = 0d0  8d0                          !
                                            !
 region-number = 2   base-geometry = line   region-priority = 2      ! Then specify
the quantum
                                                          well   with   higher
                                         priority
   z-coordinates = 3d0 5d0                          ! 2 nm GaN quantum well
$end_regions                                      !
!----------------------------------------------------------------------!
! You specified n regions in the simulation area. If they do not        !
! completely fill the simulation area, the resulting rest area is       !
! automatically assigned as region number n+1.                  !
! So you ALWAYS have one region more than you actually specified (even if   !
! they completely fill the simulation area).                    !
!----------------------------------------------------------------------!

!----------------------------------------------------------------------!
$grid-specification                                   ! for every boundary between
regions, there
                                         has to exist a grid line
 grid-type        =   0 0 1                          ! again: along z axis
 z-grid-lines     =   0d0 3d0 5d0 8d0                 ! explicity specified grid lines
 z-nodes          =      79   79   79                ! number of additional grid lines
between those
 z-grid-factors   =      1d0   1d0   1d0              ! can be used for
inhomogeneous grids
$end_grid-specification                               !
```

```
!-------------------------------------------------------------------!

!-------------------------------------------------------------------!
$region-cluster                                    ! regions can be grouped into
clusters
 cluster-number = 1    region-numbers = 1 3   ! AlN barrier, includes additional
 region n+1
 cluster-number = 2   region-numbers = 2              ! quantum well
$end_region-cluster                          !
!-------------------------------------------------------------------!
!****** MATERIALS AND ALLOY PROFILES****************************
!-------------------------------------------------------------------!
$material                               !
 material-number = 1                      !
 material-name   = AlN(zb)                ! AlN barriers, alloy concentrations
specified below
 cluster-numbers = 1                      !also arbitrary concentration
profiles possible
 material-number = 2                      !
 material-name   = GaN(zb)                ! GaN quantum wells
 cluster-numbers = 2                      !
$end_material                             !
!-------------------------------------------------------------------!
$doping-function                          !

 doping-function-number    = 1                    !
 impurity-number         = 1          ! properties of this impurity type have to be
specified below
 doping-concentration    = 50.0d0
 only-region          = 3d0  5d0
! position          = 4.0d0              ! doping concentration refers to
that position

$end_doping-function
!-------------------------------------------------------------------!
$impurity-parameters                      !

 impurity-number        = 1
 impurity-name          = Si            ! impurity numbers labelled in doping-
function
 impurity-type          = n-type            ! n-type, p-type
 number-of-energy-levels    = 1                  ! number of energy levels of
this impurity
                                          (only 1 is currently allowed)
 energy-levels-relative    = 0.02d0              ! energy relative to 'nearest'
band edge
```

```
                                      (n-type  ->  conduction  band,  p-type  ->
                                      valence band)
        degeneracy-of-energy-levels  = 2              ! degeneracy of energy levels, 2 for n-type,
4 for p-type

        $end_impurity-parameters                              !

        !******QUANTUM*************************************************!

        !--------------------------------------------------------------------!
        $quantum-regions                        ! Schroedinger equation is only solved inside
this region(s)
         region-number        = 1                              ! usually only one simulation
region
          base-geometry        = line                              !
          region-priority      = 1                              !
          z-coordinates        = 0d0 8d0                              ! can also be smaller than total
simulation region
        $end_quantum-regions                              !
        !--------------------------------------------------------------------!

        !--------------------------------------------------------------------!
        $quantum-cluster                              ! again: regions can be grouped
into clusters
         cluster-number      = 1                              !
          region-numbers      = 1                              !
          deactivate-cluster  = no                              !
        $end_quantum-cluster                              !
        !--------------------------------------------------------------------!

        !--------------------------------------------------------------------!
        $quantum-model-electrons                      ! how to solve Schroedinger equation
for electrons
         model-number                = 1                      !
         model-name                = effective-mass          ! quantum model, here: single
band
                                              effective mass approximation
         cluster-numbers                = 1          ! quantum cluster numbers to which this
model applies
         conduction-band-numbers    = 1      ! select conductions bands (minima), here: only
gamma point
         number-of-eigenvalues-per-band          = 4                              ! how many
eigenenergies are
                                              calculated for each band
         separation-model              = eigenvalue              ! to determine separation
between
                                              classic and quantum density
```

```
    maximum-energy-for-eigenstates      = 1d0                ! has to be present but is ignored in

                                                             separation      model
                                              "eigenvalue"
    quantization-along-axes          = 0 0 1           ! directions in which charge carriers are

                                              quantized, here: same as simulation
                                         direction
    boundary-condition-001           = periodic             ! periodic boundary conditions for

                                              superlattice calculations
    num-ks-001               = 5            !number of superlattice periods calculated (here 5)
   $end_quantum-model-electrons                    !
   !--------------------------------------------------------------------!

   !--------------------------------------------------------------------!
   $quantum-model-holes                              ! same for holes
    model-number              = 1              !
    model-name                 =  effective-mass          ! quantum model, here: single band

                                              effective mass approximation
    cluster-numbers             = 1                 ! quantum cluster numbers to which this

                                              model applies
    valence-band-numbers          = 1 2 3              ! select valence bands (maxima), 1 =

                                              heavy holes, 2 = light holes, 3 = split-off holes
    number-of-eigenvalues-per-band     =  4 4 4               ! how many eigenenergies are

                                              calculated for each band
    separation-model            = eigenvalue          ! to determine separation between

                                              classic and quantum density
    maximum-energy-for-eigenstates     = 1d0 1d0 1d0          ! has to be present but is

                                              ignored   in   separation   model
                                         "eigenvalue"
    quantization-along-axes          = 0 0 1             ! directions in which charge carriers are

                                              quantized, here: same as simulation
                                         direction
    boundary-condition-001          = periodic             ! ! periodic boundary conditions for

                                              superlattice calculations
```

```
    num-ks-001                      =  5                    !number of superlattice periods
calculated (here 5)
    $end_quantum-model-holes                              !
    !---------------------------------------------------------------------------!


    !****** OUTPUT*******************************************!


    !---------------------------------------------------------------------------!
    $output-1-band-schroedinger                            !
     destination-directory              = sg_1band/              !
     sg-structure                 = no                    !
     conduction-band-numbers             = 1                    ! only gamma point (as
specified above)
     cb-min-ev                  = 1                    !
     cb-max-ev                   = 4                    ! four eigenvalues per band (as
specified above)
     valence-band-numbers            = 1 2 3              ! heavy hole, light hole and
split-off hole
                                                         (as specified above)
     vb-min-ev                  = 1                    !
     vb-max-ev                   = 4                    ! four eigenvalues per band (as
specified above)
     complex-wave-functions            = no                    !
     scale                    = 2d0                    ! for psi_squared, no physical
relevance
     interband-matrix-elements           = yes
     intraband-matrix-elements            = yes                              ! electron-
hole transition
                                                 energies  and  wave  function
                                            overlaps
    $end_output-1-band-schroedinger                         !
    !---------------------------------------------------------------------------!


    !---------------------------------------------------------------------------!
    $output-bandstructure                     ! output for the band structure and the
potential
     destination-directory              = band_struc/              !
     conduction-band-numbers              = 1                    ! conduction band edge at
gamma point
     valence-band-numbers             = 1 2 3                  ! valence band edge for
heavy, light and
                                                 split-off holes
     potential                  = no                    !
    $end_output-bandstructure                              !
    !---------------------------------------------------------------------------!
```

6.6 nextnano³ Input File for a GaN/AlGaN RTD Structure Using CBR Method

Subsequently, the source code for the calculation of the I-V characteristic of an AlGaN/GaN resonant tunneling structure is given. It is also based on a sample file by Stefan Birner. Again it was modified for our material system. Source code is printed black while comments are light blue.

```
!****** OVERALL SIMULATION PARAMETERS*******************!

!-----------------------------------------------------------------!
$numeric-control                                        !
 simulation-dimension  = 1                              ! only simulate directions in
which charge
                              carriers are bound, therefore 1D simulation for a
                      quantum well
 zero-potential         = no                            ! don't consider charge
redistribution
 varshni-parameters-on = yes                            ! consider temperature dependence
of band gap
$end_numeric-control                                    !
!-----------------------------------------------------------------!


!-----------------------------------------------------------------!
$simulation-dimension                                   !
 dimension   = 1                                        ! 1D simulation
 orientation = 0 0 1                                    ! along z axis (as defined below)
$end_simulation-dimension                               !
!-----------------------------------------------------------------!


!-----------------------------------------------------------------!
$global-parameters                                      !
 lattice-temperature = 300d0                            ! 300 Kelvin
$end_global-parameters                                  !
!-----------------------------------------------------------------!


!-----------------------------------------------------------------!
$simulation-flow-control                                !
 flow-scheme      = 10                                  ! use CBR method
 raw-directory-in    = raw_data1/                       !
 raw-potential-in    = no                               !
 strain-calculation  = zero-strain-amorphous            ! don't consider strain
$end_simulation-flow-control                            !
!-----------------------------------------------------------------!


!-----------------------------------------------------------------!
```

```
$domain-coordinates                              !
 domain-type          = 0 0 1                              ! again: along z axis
 z-coordinates        = -0.5d0 33.7d0                     ! beginning and end of simulated
region in nm
 growth-coordinate-axis = 0 0 1                 ! needed if pseudomorphic strain is to be
calculated
 pseudomorphic-on      = SiC(zb)               ! needed if pseudomorphic strain is to be
calculated
 $end_domain-coordinates                              !
 !-----------------------------------------------------------------------------!

 !****** REGIONS AND CLUSTERS*******************************!

 !-----------------------------------------------------------------------------!
 $regions
 region-number = 1    base-geometry = line    region-priority = 1          !first ohmic
contact
 z-coordinates = -0.5d0  0d0

 region-number = 2    base-geometry = line   region-priority = 1          !n-doped GaN
layer
 z-coordinates = 0d0  15.0d0

 region-number = 3    base-geometry = line    region-priority = 1          !first barrier
layer
 z-coordinates = 15d0  16.0d0                              !

 region-number = 4    base-geometry = line   region-priority = 1          !undoped QW
 z-coordinates = 16d0  17.2d0

 region-number = 5    base-geometry = line   region-priority = 1          !second barrier
layer
 z-coordinates = 17.2d0  18.2d0

 region-number = 6    base-geometry = line   region-priority = 1          ! n-doped GaN
layer
 z-coordinates = 18.2d0  33.2d0

 region-number = 7    base-geometry = line   region-priority = 1          ! second ohmic
contact
 z-coordinates = 33.2d0  33.7d0

 $end_regions                              !
 !-----------------------------------------------------------------------------!
 ! You specified n regions in the simulation area. If they do not          !
 ! completely fill the simulation area, the resulting rest area is          !
 ! automatically assigned as region number n+1.                           !
```

```
! So you ALWAYS have one region more than you actually specified (even if   !
! they completely fill the simulation area).                    !
!-------------------------------------------------------------------------!

!-------------------------------------------------------------------------!
$grid-specification                              ! for every boundary between
regions, there

                                    has to exist a grid line
grid-type     =  0 0 1                        ! again: along z axis
z-grid-lines        =        -0.5d0  0d0  15d0  16.0d0  17.2d0  18.2d0  33.2d0  33.7d0
!
                                        !explicity    specified
                                grid lines
z-nodes       =      9 299  19    23    19    299   9     ! for CBR method the grid
spacing has to
                                    be equidistant
z-grid-factors   =    1d0 1d0    1d0     1d0    1d0   1d0     1d0  ! can be used for
inhomogeneous grids
$end_grid-specification                        !
!-------------------------------------------------------------------------!

!-------------------------------------------------------------------------!
$region-cluster                                  ! regions can be grouped into
clusters
cluster-number = 1   region-numbers = 1        ! first contact
cluster-number = 2   region-numbers = 2 4 6      ! GaN layers
cluster-number = 3   region-numbers = 3 5       ! AlGaN barriers
cluster-number = 4   region-numbers = 7 8            ! second contact
$end_region-cluster                      !
!******        MATERIALS      AND       ALLOY      PROFILES
*************************************

!-------------------------------------------------------------------------!
$material                              !
 material-number = 1                      !
 material-name   = GaN(zb)
 cluster-numbers = 1 2 4

 material-number = 2                        !
 material-name    = Al(x)Ga(1-x)N(zb)        ! AlGaN barriers, alloy concentrations
specified below
 cluster-numbers = 3                        !
 alloy-function  = constant              ! also arbitrary concentration profiles
possible
                        !
$end_material                      !
!-------------------------------------------------------------------------!
```

```
    $alloy-function                                 !

     material-number      = 2                       !
     function-name        = constant
    ! xalloy            = 0.1d0                          ! Al0.1Ga0.9N
     xalloy             = 0.4d0                          ! Al0.4Ga0.7N

    $end_alloy-function                             !
    !---------------------------------------------------------------------!
    !---------------------------------------------------------------------!
    $ternary-zb-default                             !
     ternary-type                = Al(x)Ga(1-x)N-zb-default      !
     apply-to-material-numbers      = 1 2 3 4                    ! Bowing parameters b
are defined
                                    for  Q[A(x)B(1-x)C] = x*Q[AC]+(1-x)*Q[BC]-
                          b*x*(1-x)
     bow-conduction-band-masses        = 0.000d0 0.000d0 0.000d0      ! DEFAULT
                          0.000d0 0.000d0 0.000d0        !
                          0.000d0 0.000d0 0.000d0        !
     bow-conduction-band-nonparabolicities = 0d0    0d0    0d0         !
     bow-conduction-band-energies      = 0.0d0   0.0d0   0.055d0     ! ZERO BOWING
FOR
                                          GAMMA   IN   THIS
                                  TUTORIAL!!!
    $end_ternary-zb-default                         !
    !---------------------------------------------------------------------!
                          !
    !---------------------------------------------------------------------!
    $poisson-boundary-conditions                    !

     poisson-cluster-number    = 1                       ! an integer number (dense
numbering as usual)
     region-cluster-number     = 1        ! an integer number which refers to an existent
region-cluster
     applied-voltage           = 0d0            ! apply voltage to poisson-cluster (required
for Dirichlet)
     boundary-condition-type   = ohmic
     contact-control           = voltage


     poisson-cluster-number             = 2             !r! an integer number (dense
numbering as usual)
     region-cluster-number     = 4       !r! an integer number which refers to an existent
region-cluster
     applied-voltage                  = 0d0          ! apply voltage to poisson-cluster (required
for Dirichlet)
     boundary-condition-type             = ohmic
```

```
    contact-control              = voltage
    $end_poisson-boundary-conditions                        !
    !--------------------------------------------------------------------!

    $voltage-sweep                              !here parameters for IV characteristics
are initialized
     sweep-number          = 1
     sweep-active          = yes
     poisson-cluster-number  = 1
     step-size            = -0.1d0                       ! 0.1 V per step
     number-of-steps       = 10                         !10 steps
     data-out-every-nth-step = 1                        !read out data every step
    $end_voltage-sweep

    $current-regions
     region-number              = 1
     base-geometry              = line
     region-priority          = 1
     z-coordinates              = -0.50d0 33.7d0
    $end_current-regions                         !oo!

    !------------------------------------------------------------------!
    $current-cluster                            !
     cluster-number              = 1                    ! an integer number to refer to
geometry element
      region-numbers              = 1 2                   ! region numbers, belonging to
cluster
      deactivate-cluster          = no                   ! flag to switch off current clusters
(yes|Yes|YES).
                                        Anything else means NO (default)
    $end_current-cluster                        !
    !------------------------------------------------------------------!
    $current-models                            !
     model-number              = 1               !
     transport-model-name        = simple-drift-model     !
     cluster-numbers            = 1               !
    $end_current-models                           !
    !------------------------------------------------------------------!

    !---------------------------------------------------------------
    !For drift diffusion, a mobility is needed.
    !Therefore on has to specify a certain mobility model and provide all
    !relevant parameters for each material in system.
    !The parameters can be listed in database and input file
    !---------------------------------------------------------------

    !---------------------------------------------------------------!
```

```
    $simple-drift-models                         !
     model-number                 = 1           !
     mobility-model               = mobility-model-simba-2  !
     current-model-numbers        = 1           !
    $end_simple-drift-models                     !


    !****** QUANTUM*****************************************!


    !-----------------------------------------------------------------!
    $quantum-regions                        ! Schroedinger equation is only solved inside
this region(s)
      region-number      = 1                           ! usually only one simulation
region
      base-geometry      = line                        !
      region-priority    = 1                          !
      z-coordinates      = 0d0 33.2d0                  ! can also be smaller than total
simulation region

      $end_quantum-regions                       !
    !-----------------------------------------------------------------!


    !-----------------------------------------------------------------!
    $quantum-cluster                            ! again: regions can be grouped
into clusters
      cluster-number     = 1                           !
      region-numbers     = 1                           !
      deactivate-cluster = no                          !

      !cluster-number     = 2                           !
      ! region-numbers    = 2                           !
      ! deactivate-cluster = yes                        !

      $end_quantum-cluster                       !
    !-----------------------------------------------------------------!


    !-----------------------------------------------------------------!
    $quantum-model-electrons                    ! how to solve Schroedinger equation
for electrons
      model-number                 = 1                 !
      model-name                   = effective-mass         ! quantum model, here:
single band

                                                       effective mass approximation
      cluster-numbers              = 1                 ! quantum cluster numbers to
which this

                                                       model applies
      conduction-band-numbers      = 1                 ! select conductions bands
(minima),
```

```
                                                    here: only gamma point
    number-of-eigenvalues-per-band        = 400          ! how many eigenenergies are
calculated
                                                    for each band (has to be much larger
                                                    than    normal    transition    energy
                                                    calculation)
    separation-model                = eigenvalue              ! to determine separation
between
                                                    classic and quantum density
    maximum-energy-for-eigenstates        = 1d0                  ! has to be present but
is ignored in
                                                    separation            model
                                                    "eigenvalue"
    quantization-along-axes           = 0 0 1        ! directions in which charge carriers
are quantized,
                                                    here: same as simulation direction
    boundary-condition-100          = Dirichlet              ! Dirichlet
    boundary-condition-010          = Dirichlet              ! Dirichlet
    boundary-condition-001            = Neumann                    ! Neuman along
propagation direction
    num-ks-001               = 5

    $end_quantum-model-electrons                          !
    !-------------------------------------------------------------------------!
    CBR method can only be used for electrons or holes that is why the hole part is
marked as
    comment
    !-------------------------------------------------------------------------!
    !$quantum-model-holes                              ! same for holes
    ! model-number              = 1                    !
    ! model-name                = effective-mass            ! quantum model, here:
single band effective mass approximation
    ! cluster-numbers              = 1                    ! quantum cluster numbers to
which this model applies
    ! valence-band-numbers          = 1 !2 !3              ! select valence bands
(maxima), 1 = heavy holes, 2 = light holes, 3 = split-off holes
    ! number-of-eigenvalues-per-band      = 4 !4 !4                  ! how many
eigenenergies are calculated for each band
    ! separation-model            = eigenvalue            ! to determine separation
between classic and quantum density
    ! maximum-energy-for-eigenstates      = 1d0 !1d0 !1d0                ! has to be
present but is ignored in separation model "eigenvalue"
    ! quantization-along-axes        = 0 0 1              ! directions in which charge
carriers are quantized, here: same as simulation direction
    ! boundary-condition-100        = Dirichlet            ! Dirichlet
    ! boundary-condition-010        = Dirichlet            ! Dirichlet
```

```
    ! boundary-condition-001            = Neumann            ! Neuman along
propagation direction
    ! num-ks-001               = 5
    !$end_quantum-model-holes                       !
    !-------------------------------------------------------------------------!
    !******                                                          CBR
********************************************************************!
    !-------------------------------------------------------------------------!
   $CBR-current                                    !

    destination-directory           = CBR_data1/                ! directory for output and
data files
    calculate-CBR              = yes                ! flag: "yes"/"no"
    calculate-CBR-DOS           = yes                 ! flag: "yes"/"no"
    !calculate-CBR-DOS          = no                 ! flag: "yes"/"no"
    self-consistent-CBR         = yes!no                 ! flag: "yes"/"no"
    read-in-CBR-states          = no                 ! flag: "yes"/"no"
                                          !
    main-qr-num              = 1                ! number of main quantum region
for which
                                       transport is calculated
    num-leads         = 2  ! must be '2' in 1D          ! total number of leads attached to
main region
    lead-qr-numbers             = 2 3             ! quantum region numbers corresponding
to each lead
    !propagation-direction          = 1 1 ! '1' = x          ! direction of propagation (1,2,3)
for each lead
    propagation-direction         = 3 3 ! '3' = z            ! direction of propagation (1,2,3)
for each lead
    num-modes-per-lead           = 1 1 ! cannot be larger than '1' in 1D ! number of
modes per lead

                             used for CBR calculation must be <= number
                          of eigenvalues specified in corresponding quantum
                          model
    !++++++++++++++++++++++++++++++++++++++++++++++++++++++++++++++++++++++
    !num-eigenvectors-used         = 10                ! number of eigenvectors in
main
                                quantum   region   used   for   CBR
                                calculation
    !num-eigenvectors-used         = 40                ! number of eigenvectors in
main
                                quantum   region   used   for   CBR
                                calculation
    !num-eigenvectors-used         = 101                ! number of eigenvectors in
main
                                quantum   region   used   for   CBR
                                calculation
```

```
    num-eigenvectors-used           = 40                    ! number of eigenvectors in
main quantum

                                               region used for CBR calculation
    !+++++++++++++++++++++++++++++++++++++++++++++++++++++++++++++++++++++++++
++++++++
    E-min                  = -1.5d0                ! lower boundary for transmission
energy interval
    E-max                  =  1.5d0                ! upper boundary for transmission
energy interval
    ! E-min                 =  -0.6d0               ! upper boundary for transmission
energy interval
    ! E-max                 =  0.6d0                ! upper boundary for transmission
energy interval
    !E-max                  =  2.5d0                ! upper boundary for transmission
energy interval
    !num-energy-steps        =  250                ! number of energy steps
    !num-energy-steps        =  700                ! number of energy steps
    !num-energy-steps        = 1000                ! number of energy steps
    num-energy-steps            = 1000 ! to get a higher resolution     ! number of
energy steps
    adaptive-energy-grid        = no                        ! use adaptive energy grid
(very useful if

                                       self-consistent-CBR = yes)
    !adaptive-energy-grid        = adaptive-exponential        ! use adaptive energy
grid (very

                                       useful if self-consistent-CBR =
                              yes)
                                     !
    $end_CBR-current                        !
    !----------------------------------------------------------------------!
    !******                          END                          CBR
*********************************************************!

    $doping-function                              !

    doping-function-number    = 1                    !
    impurity-number          = 1                      ! properties of this impurity type
have to be
                                       specified below
    doping-concentration      = 50.0d0                  !GaN layer n-doped 5e19 per
cm^3
    only-region            = 0.0d0  13.0d0            ! doping concentration refers to
that position

    doping-function-number    = 2                    !
    impurity-number          = 1                      ! properties of this impurity type
have to be
```

```
                                                           specified below
        doping-concentration       = 0.1d0                          !GaN spacer layer uid
background doping
        only-region          = 13d0  15.0d0              ! doping concentration refers to
that position


        doping-function-number    = 3                              !
         impurity-number         = 1                       ! properties of this impurity type
have to be

                                                           specified below
        doping-concentration       = 0.5d0                 !AlGaN background doping
        only-region          = 15d0  16d0             ! doping concentration refers to that
position


        doping-function-number    = 4                              !
         impurity-number         = 1                       ! properties of this impurity type
have to be

                                                           specified below
        doping-concentration       = 0.1d0                          !GaN  spacer  layer  uid
background doping
        only-region          = 16d0  17.2d0           ! doping concentration refers to that
position


        doping-function-number    = 5                              !
         impurity-number         = 1                       ! properties of this impurity type
have to be

                                                           specified below
        doping-concentration     = 0.5d0                  AlGaN background doping
        only-region          = 17.2d0  18.2d0         ! doping concentration refers to that
position


        doping-function-number    = 6                              !
         impurity-number         = 1                       ! properties of this impurity type
have to be

                                                           specified below
        doping-concentration       = 0.1d0                          !GaN  spacer  layer  uid
background doping
        only-region            = 18.2d0  20.2d0         ! doping concentration refers to
that position


        doping-function-number    = 7                              !
         impurity-number         = 1                       ! properties of this impurity type
have to be

                                                           specified below
        doping-concentration     = 50.0d0                  !GaN layer n-doped 5e19 per cm^3
        only-region           = 20.2d0  33.2d0         ! doping concentration refers to that
position
```

```
$end_doping-function
!----------------------------------------------------------------------!
$impurity-parameters                              !

 impurity-number        = 1
 impurity-name          = Si                  ! impurity numbers labelled in doping-
function
 impurity-type          = n-type                  ! n-type, p-type
 number-of-energy-levels    = 1                      ! number of energy levels of
this impurity
                                            (only 1 is currently allowed)
 energy-levels-relative    = 0.02d0                  ! energy relative to 'nearest'
band edge
                                      (n-type  ->  conduction  band,  p-type  ->
                        valence band)
 degeneracy-of-energy-levels  = 2          ! degeneracy of energy levels, 2 for n-type,
4 for p-type

$end_impurity-parameters                       !

!++++++++++++++++++++++++++++++++++++++++++++++++++!
!Here interfaces for fixed charge calculations are introduced!
!++++++++++++++++++++++++++++++++++++++++++++++++++!
$material-interfaces                   !optional !
 interface-number              = 1     !required !
 apply-between-material-numbers      = 2 1   !required !
 state-numbers               = 1   !required !

 interface-number              = 2    !  required !
 apply-between-material-numbers      = 1 2   !required !
 state-numbers               = 1     ! required !

$end_material-interfaces                  !optional !

!----------------------------------------------------------!
$interface-states                  !optional !
 state-number             = 1        !required  !
 state-type               = fixed-charge     !required ! trap, fixed-charge, electrolyte
 interface-density           = 5d12        !5e12 per cm^2
! number-of-energy-levels       integer     !optional  ! for trap
! energy-levels-relative       double_array   !optional  ! for trap
! degeneracy-of-energy-levels    integer_array  !optional  ! for trap
! transition-times-cb-to-levels   double_array   !optional  ! for trap
! transition-times-levels-to-vb   double_array   !optional  ! for trap
! adsorption-constant         double      !optional  ! for electrolyte
! dissociation-constant        double      !optional  ! for electrolyte
```

```
    ! pressure                    double        !optional  ! for gas
    ! surface-phonon-frequencies      double_array    !optional  ! for gas (1st = weakly,
2nd =
                                             strongly  chemisorbed  surface
                      state)
    ! accomodation-coefficients      double_array    !optional  ! for gas (1st = weakly,
2nd = strongly
                                             chemisorbed surface state)
    ! energy-levels-chemisorbed-states  double_array   !optional  ! for gas (1st = weakly,
2nd =
                                             strongly  chemisorbed  surface
                      state)
    ! free-molecule-energy          double        !optional  ! for gas
    ! molecule-mass                double        !optional  ! for gas
    $end_interface-states                   !optional  !
    !--------------------------------------------------------------!

    !****** OUTPUT*********************************************!

    !----------------------------------------------------------------------!
    $output-1-band-schroedinger                        !
     destination-directory          = sg_1band/              !
     sg-structure                = yes                 !
     conduction-band-numbers          = 1                  ! only gamma point (as
specified above)
     cb-min-ev                = 0                  !
     cb-max-ev                = 40                  ! 40 eigenvalues per band (as
specified above)
     !valence-band-numbers          = 1                  ! heavy hole, light hole and
split-off hole
                                             (as specified above)
     !vb-min-ev                = 1                  !
     !vb-max-ev                = 10                  ! four eigenvalues per band (as
specified above)
     complex-wave-functions          = no                 !
     scale                 = 0.1d0                  ! for psi_squared, no physical
relevance
     interband-matrix-elements        = no
     intraband-matrix-elements         = no                  ! electron-hole transition
energies and
                                             wave function overlaps
    $end_output-1-band-schroedinger                      !
    !----------------------------------------------------------------------!


    !----------------------------------------------------------------------!
    $output-bandstructure                        ! output for the band structure and
the potential
```

```
    destination-directory         = band_struc/          !
    conduction-band-numbers          = 1                    ! conduction band edge at
gamma point
    !valence-band-numbers        = 1 !2 !3      ! valence band edge for heavy, light and
split-off holes
    potential                = yes                !
    $end_output-bandstructure                        !
    !-----------------------------------------------------------------------!
    $output-densities                            !
    destination-directory         = densities1/
    electrons              = yes                !
    holes              = no                !
    charge-density            = yes!no                !
    ! piezo-electricity          = no                !
    ! pyro-electricity          = no                !
    interface-density            = yes                !
    $end_output-densities                        !

    ! This is the output for the current.              !
    !-----------------------------------------------------------------------!
    $output-current-data                        !
    destination-directory          = current1/            !
    current              = no!yes                !
    !current               = no                !
    fermi-levels              = yes                !
    !fermi-levels              = no                !
    !mobility-out              = no                !
    !IV-curve-out              = no                !
    IV-curve-out              = yes                !
    !recombination            = no
    $end_output-current-data                        !
    !-----------------------------------------------------------------------!

    !-----------------------------------------------------------------------!
    ! This is the output for the doping concentration, …            !
    !-----------------------------------------------------------------------!
    $output-material
    destination-directory        = material1/                    !
    conduction-band-masses        = conduction_band_masses1D.dat
    conduction-band-energies      = conduction_band_energies1D.dat
    $end_output-material                        !
    !-----------------------------------------------------------------------!
    ! This is the output for the material grid.              !
    !-----------------------------------------------------------------------!
    $output-grid                            !
    grid-coordinate              = 0 0 1                !
    output-file              = z_grid.dat
```
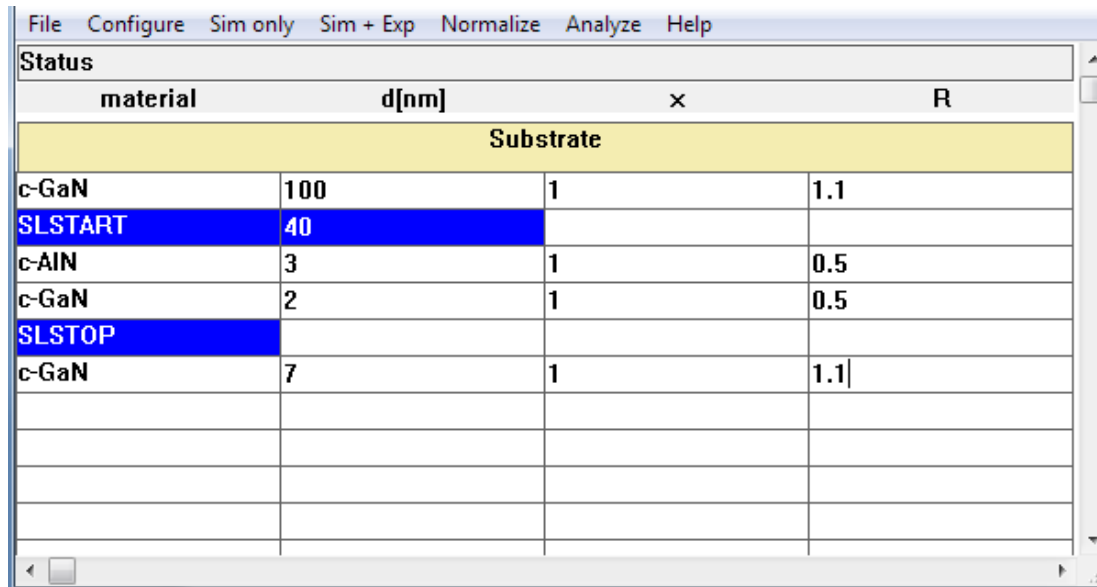
```
$end_output-grid                                  !
!---------------------------------------------------------------------!
!$output-current-data                                    !
! destination-directory            = current1\
! current                  = yes !
! IV-curve-out = yes
!$end_output-current-data
```

$end_output-grid   !
!---!

6.7 MadMax Input

Below you see a screen shot of the input interface of MadMax. Any layer system can be chosen by a drag down menu and even superlattices can easily be implemented considering number of periods or strain conditions.

material	d[nm]	x	R
File Configure Sim only Sim + Exp Normalize Analyze Help			
Status			
Substrate			
c-GaN	100	1	1.1
SLSTART	40		
c-AlN	3	1	0.5
c-GaN	2	1	0.5
SLSTOP			
c-GaN	7	1	1.1

7 Bibliography

[1]   D. J. As, *Microelectronics Journal*, **40**, 204 (2009).

[2]   S. V. Novikov, C. T. Foxon, and A. J. Kent, *phys. stat. sol. (a)* **207**, 1277 (2010).

[3]   J. Schörmann, S. Potthast, D. J. As, and K. Lischka, *Appl. Phys. Lett.* **89**, 131910 (2006).

[4]   T. Schupp, K. Lischka, and D. J. As, *J. Crystal Growth* **312**, 1500 (2010).

[5]   M. Helm, *Intersubband Transition in Quantum Wells: Physics and Device Applications I, Vol. 62 of Semiconductors and Semimetals*, H. C. Liu and F. Capasso, Eds. Academic, New York (2000).

[6]   E. Tschumak, R. Granzner, J. K. N. Lindner, F. Schwierz, K. Lischka, H. Nagasawa, M. Abe, and D. J. As, *Appl. Phys. Lett.* **96**, 253501 (2010).

[7]   N. Zainal, S. V. Novikov, C. J. Mellor, C. T. Foxon, and A. J. Kent, *Appl. Phys. Lett.* **97**, 112102 (2010).

[8]   J. E. A. DeCuir, E. Fred, M. O. Manasreh, J. Schörmann, D. J. As, and K. Lischka, *Appl. Phys. Lett.* **91**, 041911 (2007).

[9]   H. Machhadani, M. Tchernycheva, L. Rigutti, S. Sakr, R. Colombelli, C. Mietze, D. J. As, and F. H. Julien, *Phys. Rev. B* **83**, 075313 (2011).

[10]   J. H. Davies, *The physics of low-dimensional semiconductors: an introduction*, Cambridge University Press (1998).

[11]   T. Ando, A. B. Fowler, and F. Stern, *Rev. Mod. Phys.* **54**, 437 (1982).

[12]   F. C. H.C. Liu, Ed., *Semiconductors and Semimetals Volume 62: Intersubband Transitions in Quantum Wells: Physics and Device Applications I*. Academic Press (2000).

[13]   nextnano³ device simulator, nextnano3 device simulator: The program is available at www.nextnano.de.

[14]   S. Birner, S. Hackenbuchner, M. Sabathil, G. Zandler, J. A. Majewski, T. Andlauer, T. Zibold, R. Morschl, A. Trellakis, and P. Vogl, *Acta Physica Polonica A* **110**, 111 (2006).

[15]   W. L. Bragg, *Proc. Cambridge Phil. Soc.* **17**, 43 (1913).

[16]   P. F. Fewster, *X-ray scattering from semiconductors*. Imperial College Press (2000).

[17]   C. B. C. David B. Williams, *Tranmission Electron Microscopy - A Textbook for Material Science*. Springer Science+Business Media (2009).

[18]   M. Bürger, T. Schupp, K. Lischka, and D. As, *phys. stat. sol. (c)* **9**, 1273 (2012).

[19]   O. Brandt, P. Waltereit, and K. H. Ploog, *Journal of Physics D: Applied Physics* **35**, 577 (2002).

[20]   S. Birner, C. Schindler, P. Greck, M. Sabathil, and P. Vogl, *Journal of Computational Electronics* **8**, 267 (2009).

[21]   N. Suzuki and N. Izuka, *Jpn. J. Appl. Phys. Part 2* **36**, L1008 (1999).

[22]   N. Suzuki and N. Izuka, *Jpn. J. Appl. Phys. Part 2* **37**, L369 (1998).

[23]   T. Asano, K. Tomoda, and S. Noda, in *Extended Abstracts of the 25th International Symposium on Compound Semiconductors* (1998).

[24]   J. E. A. DeCuir, M. O. Manasreh, E. Tschumak, J. Schormann, D. J. As, and K. Lischka, *Appl. Phys. Lett.* **92**, 201910 (2008).

[25]   C. Mietze, J. E. A. DeCuir, M. O. Manasreh, K. Lischka, and D. J. As, *phys. stat. sol. (c)* **8**, 1204 (2011).

[26]   R. Tsu and L. Esaki, *Appl. Phys. Lett.* **22**, 562 (1973).

[27]   H. Mizuta and T. Tanoue, *The Physics and Applications of Resonant Tunneling Diodes*, Cambridge University Press (1995).

[28]   L. L. Chang, L. Esaki, and R. Tsu, *Appl. Phys. Lett.* **24**, 593 (1974).

[29]   O. G. Lafaye, P. Boucaud, F. H. Julien, S. Sauvage, S. Cabaret, J. M. Lourtioz, V. T. Mieg, and R. Planel, *Appl. Phys. Lett.* **71**, 3619 (1997).

[30]   F. H. Julien, A. Sa'ar, J. Wang, and J. P. Leburton, *Electron. Lett.* **31**, 838 (1995).

[31]   A. S. Barker and M. Ilegems, *Phys. Rev. B* **7**, 743 (1973).

[32]   L. Patrick and W. J. Choyke, *Phys. Rev.* **123**, 813 (1961).

[33]   A. Helman, M. Tchernycheva, A. Lusson, E. Warde, F. H. Julien, K. Moumanis, G. Fishman, E. Monroy, B. Daudin, L. S. Dang, E. Bellet-Amalric, and D. Jalabert, *Appl. Phys. Lett.* **83**, 5196 (2003).

[34]   M. Tchernycheva, L. Nevou, L. Doyennette, F. H. Julien, E. Warde, F. Guillot, E. Monroy, E. Bellet-Amalric, T. Remmele, and M. Albrecht, *Phys. Rev. B* **73**, 125347 (2006).

[35]   F. Julien, M. Tchernycheva, L. Nevou, L. Doyennette, R. Colombelli, E. Warde, F. Guillot, and E. Monroy, *phys. stat. sol. (a)* **204**, 1987 (2007).

[36]   T. Unuma, M. Yoshita, T. Noda, H. Sakaki, and H. Akiyama, *J. Appl. Phys.* **93**, 1586 (2003).

[37]   C. Q. Chen, R. Helbiga, J. Zemanb, and A. J. L. Poulterb, *Physica B* **293**, 402 (2001).

[38]   H. Machhadani, P. Kandaswamy, S. Sakr, A. Vardi, A. Wirtmüller, L. Nevou, F. Guillot, G. Pozzovivo, M. Tchernycheva, A. Lupu, L. Vivien, P. Crozat,

E. Warde, C. Bougerol, S. Schacham, G. Strasser, G. Bahir, E. Monroy, and F. H. Julien, *New Journal of Physics* **11**, 125023 (2009).

[39]   A. Trellakis, T. Zibold, T. Andlauer, S. Birner, R. K. Smith, R. Morschl, and P. Vogl, *Journal of computational Electronics* **5**, 285 (2006).

[40]   M. Städele and K. Hess, *J. Appl. Phys.* **88**, 6945 (2000).

[41]   E. O. Kane, *Journal of Physics and Chemistry of Solids* **1**, 249 (1957).

[42]   C. Wetzel, R. Winkler, M. Drechsler, B. K. Meyer, U. Rössler, J. Scriba, J. P. Kotthaus, V. Härle, and F. Scholz, *Phys. Rev. B* **53**, 1038 (1996).

[43]   M. Röppischer, R. Goldhahn, G. Rossbach, P. Schley, C. Cobet, N. Esser, T. Schupp, K. Lischka, and D. J. As, *J. Appl. Phys.* **106**, 076104 (2009).

[44]   V. Bougrov, M. E. Levinshtein, S. L. Rumyantsev, and A. Zubrilov, *in Properties of Advanced Semiconductor Materials GaN, AlN, InN, BN, SiC, SiGe.* New York: John Wiley & Sons (2001).

[45]   I. Petrov, E. Mojab, R. C. Powell, J. E. Greene, L. Hultman, and J.-E. Sundgren, *Appl. Phys. Lett.* **60**, 2491 (1992).

[46]   M. Mizuta, S. Fujieda, Y. Matsumoto, and T. Kawamura, *Jpn. J. Appl. Phys.* **25** Part 2, L945 (1986).

[47]   S. K. Pugh, D. J. Dugdale, S. Brand, and R. A. Abram, *Semiconductor Science and Technology* **14**, 23 (1999).

[48]   W. J. Fan, M. F. Li, T. C. Chong, and J. B. Xia, *J. Appl. Phys.* **79**, 188 (1996).

[49]   C. G. van de Walle and J. Neugebauer, *Appl. Phys. Lett.* **70**, 2577 (1997).

[50]   K. Kim, Lambrecht, R. L. Walter, and B. Segall, *Phys. Rev. B* **53**, 16310 (1996).

[51]   P. Rinke, M. Winkelnkemper, A. Qteish, D. Bimberg, J. Neugebauer, and M. Scheffler, *Phys. Rev. B* **77**, 075202 (2008).

[52]   J. W. Orton, *Semiconductor Science and Technology* **12**, 64 (1997).

[53]   I. Vurgaftman, J. R. Meyer, and L. R. Ram-Mohan, *J. Appl. Phys.* **89**, 5815 (2001).

[54]   Q. Guo and A. Yoshida, *Jpn. J. Appl. Phys.* **33**, 2453 (1994).

[55]   P. Hohenberg and W. Kohn, *Phys. Rev.* **136**, B864 (1964).

[56]   W. Kohn and L. J. Sham, *Phys. Rev.* **140**, A1133 (1965).

[57]   P. E. Blöchl, *Phys. Rev. B* **50**, 17953 (1994).

[58]   G. Kresse and D. Joubert, *Phys. Rev. B* **59**, 1758 (1999).

[59]   G. Kresse and J. Furthmüller, *Computational Materials Science* **6**, 15 (1996).

[60]   D. M. Ceperley and B. J. Alder, *Phys. Rev. Lett.* **45**, 566 (1980).

[61]   J. P. Perdew and A. Zunger, *Phys. Rev. B* **23**, 5048 (1981).

[62]   J. Heyd, G. E. Scuseria, and M. Ernzerhof, *J. Chem. Phys.* **118**, 8207 (2003).

[63]   J. Heyd and G. E. Scuseria, *J. Chem. Phys.* **121**, 1187 (2004).

[64]   J. Heyd, J. E. Peralta, G. E. Scuseria, and R. L. Martin, *J. Chem. Phys.* **123**, 174101 (2005).

[65]   J. Heyd, G. E. Scuseria, and M. Ernzerhof, *J. Chem. Phys.* **124**, 219906 (2006).

[66]   C. Mietze, M. Landmann, E. Rauls, H. Machhadani, S. Sakr, M. Tchernycheva, F. H. Julien, W. G. Schmidt, K. Lischka, and D. J. As, *Phys. Rev. B* **83**, 195301 (2011).

[67]   S. Golka, C. Pflügl, W. Schrenk, C. Skierbiszewski, M. Siekacz, I. Grzegory, S. Porowski, and G. Strasser, *Appl. Phys. Lett.* **88**, 172106 (2006).

[68]   J. Schörmann, S. Potthast, D. J. As, and K. Lischka, *Appl. Phys. Lett.* **90**, 041918 (2007).

[69]   R. Fischer, D. Neuman, H. Zabel, H. Morkoc, C. Choi, and N. Otsuka, *Appl. Phys. Lett.* **48**, 1223 (1986).

[70]   R. Fischer, H. Morkoc, D. A. Neumann, H. Zabel, C. Choi, N. Otsuka, M. Longerbone, and L. P. Erickson, *J. Appl. Phys.* **60**, 1640 (1986).

[71]   S. M. Bedair, T. P. Humphreys, N. A. El-Masry, Y. Lo, N. Hamaguchi, C. D. Lamp, A. A. Tuttle, D. L. Dreifus, and P. Russell, *Appl. Phys. Lett.* **49**, 942 (1986).

[72]   D. J. As, S. Potthast, U. Köhler, A. Khartchenko, and K. Lischka, *MRS Symp. Proc.* **693**, l 2.3 (2002).

[73]   P. Harrison, *Quantum Wells, Wires and Dots*. John Wiley & Sons (2005).

[74]   R. Kemper, M. Weinl., C. Mietze, M. Häberlen, T. Schupp, E. Tschumak, J. Lindner, K. Lischka, and . D.J. As, *J. Crystal Growth* **323**, 84 (2011).

List of Abbreviations

ACQW	Asymmetric Coupled Quantum Well
AFM	Atomic Force Microscope
AlGaN	cubic $Aluminium_x Gallium_{1-x}$ Nitride
AlN	cubic Aluminium Nitride
BEP	Beam Equivalent Pressure
CBO	Conduction Band Offset
CL	Cathodoluminescence
DAP	Donor Acceptor Peak
DFT	Density Functional Theory
DOS	Density of States
FET	Field Effect Transistor
FWHM	Full Width at Half Maximum
GaN	cubic Gallium Nitride
HEMT	High Electron Mobility Transistor
HRXRD	High Resolution X-Ray Diffraction
HSE	Hybrid Density Functionals
ISB	Intersubband
ISBT	Intersubband Transition
IR	Infrared
LDA	Local Density Approximation
MBE	Molecular Beam Epitaxy
MOCVD	Metal-Organic Vapor Phase Deposition
MQW	Multi-Quantum-Wells
PAMBE	Plasma Assisted Molecular Beam Epitaxy
PL	Photoluminescence
PAW	Projector-Augmented Wave
PVR	Peak-to-Valley Ratio
QCL	Quantum Cascade Laser
QCSE	Quantum Confinement Stark Effect
QFL	Quantum Fountain Laser
QW	Quantum Well
QWIP	Quantum Well Infrared Photodetector
rf	Radio-frequency
RHEED	Reflection High Energy Electron Diffraction

RSM   Reciprocal Space Map

RT   Resonant Tunneling

RTD   Resonant Tunneling Diode

SEM   Scanning Electron Microscope

SL   Superlattice

UHV   Ultra High Vacuum

UV   Ultraviolet

VASP   Vienna Ab-initio Simulation Package

VBO   Valence Band Offset

XC   Exchange Correlation

List of Figures

List of Tables

List of Publications

i. **C. Mietze**, E.A. DeCuir, M.O. Manasreh, K. Lischka, and D.J. As: *Inter- and intrasubband spectroscopy of cubic AlN/GaN superlattices grown by molecular beam epitaxy on 3C-SiC* phys. stat. sol. (c) **7** (1), 64 (2010).

ii. A. Scholle, S. Greulich-Weber, D.J. As, **C. Mietze**, N.T. Son, U. Gerstmann, S. Sanna, E. Rauls, W.G. Schmidt: *Magnetic characterization of conductance electrons in GaN* phys. stat. sol. (b) **247** (7), 1728 (2010).

iii. **C. Mietze**, E.A. DeCuir, M.O. Manasreh, K. Lischka, and D.J. As: *Band offset betwen cubic GaN and AlN from intra- and interband spectroscopy of superlattices* AIP Conf. Proc. **1292**, 169 (2010).

iv. **C. Mietze**, E.A. DeCuir, M.O. Manasreh, K. Lischka, and D.J. As: *Intrasubband transitions in cubic AlN/GaN superlatices for detectors from near to far infrared* phys. stat. sol. (c) **8** (4), 1204 (2011).

v. R.M. Kemper, M. Weinl. **C. Mietze**, M. Häberlen, T. Schupp, E. Tschumak, J.K.N. Lindner, K. Lischka, D.J. As: *Growth of cubic GaN on nano-patterned 3C-SiC (001) substrates* J. Crystal Growth **323**, 84 (2011).

vi. H. Machhadani, M. Tchernycheva, L. Rigutti, S. Saki, R. Colombelli, **C. Mietze**, D.J. As, and F.H. Julien: *Intersubband absorption of cubic GaN/Al(Ga)N quantum wells in the near-infrared to THz spectral range* Phys. Rev. B **83**, 075313 (2011).

vii. **C. Mietze**, M. Landmann, E. Rauls, H. Machhadani, S. Sakr, M. Tchernycheva, F.H. Julien, W.G. Schmidt, K. Lischka, and D.J. As: *Band offsets in cubic GaN/AlN superlattices* Phys. Rev. B **83**, 195301 (2011).

viii. **C. Mietze**, K. Lischka, and D.J. As: *Current-voltage characteristics of cubic Al(Ga)N/GaN double barrier structures on 3C-SiC* phys. stat. sol. (a) **209** (3), 439 (2012).

ix. D.J. As and **C. Mietze**: (invited paper) *MBE growth and applications of cubic AlN/GaN quantum wells,* phys. stat. sol. (a) (2012) (published online DOI: 10.1002/pssa.201200653).

x. **C. Mietze**, S. Sakr, M. Tchernycheva, F.H. Julien, and D.J. As: *Cubic III-nitride coupled quantum wells towards unipolar optically pumped lasers*, phys. stat. sol. (a) (2013) (published online DOI:10.1002/pssa.201200476).

Conference Contributions

06/2009	**Poster Presentation** E-MRS (European Material Research Society) 2009 Spring Meeting, Straßburg
Title	**Inter-/ and intrasubband spectroscopy of cubic AlN/GaN superlattices on 3C-SiC**
06/2010	**Oral Presentation** E-MRS (European Material Research Society) 2010 Spring Meeting, Straßburg
Title	**Band offset between cubic GaN and AlN from intra- and interband spectroscopy of superlattices**
08/2010	**Poster Presentation** NOEKS10 (International Workshop on Nonlinear Optics and Excitation Kinetics in Semiconductors), Paderborn
Title	**Intrasubband transitions in cubic AlN/GaN superlattices for detectors from near to far infrared**
08/2010	**Participant** IVAM Summerschool Mikrotechnik, Dortmund
07/2011	**Poster Presentation** ICNS 9 (9th International Conference on Nitride Semiconductors), Glasgow
Title	**Current-voltage characteristics of cubic Al(Ga)N/GaN double barrier structures on 3C-SiC**
10/2011	**Oral Presentation** Deutscher MBE-Workshop 2011, Berlin
Title	**Cubic GaN/AlN superlattices for the near- and far-infrared spectral region**
07/2012	**Poster Presentation** ISGN 4 (4th International Symposium on Growth of III-Nitrides), St. Petersburg
Title	**Cubic III-nitride coupled quantum wells towards unipolar optically pumped lasers**

List of Samples

Sample Number	Substrate	Layer
1874	SFD03AF (d)	600 nm GaN
1875	Sample lost in chamber	
1876	SGB04AG-1#2	600 nm GaN
1889	NovaSiC 100-C500	600 nm GaN
1918	PC571a	600 nm GaN
1919	PC571a	500 nm GaN:Si (T_{Si}=1100°C)
1920	PC571a	500 nm GaN:Si (T_{Si}=1080°C)
1921	PC571a	500 nm GaN:Si (T_{Si}=1120°C)
1922	NovaSiC C497	400 nm GaN
1953	SFB01AA#1	600 nm GaN
1954	SFB01AA#1	Growth on back of substrate
1955	SFB01AA-a	200 nm GaN
1956	SFB01AA-b	substrate 150 nm GaN 2 GaN QW(12 ML) in 3 AlN barriers (14 ML) 30 nm GaN 2 GaN QW(12 ML) in 3 AlN barriers (14 ML) 30 nm GaN
1963	NovaSiC 100-C615	600 nm GaN
1964	NovaSiC 100-C615	100 nm GaN buffer GaN:Si(2e18)/AlN SL 40 per. 12.5 nm/3 nm 10 nm GaN cap
1965	NovaSiC 100-C615	100 nm GaN buffer GaN:Si(2e18)/AlN SL 40 per. 11 nm/3 nm 10 nm GaN cap
1966	NovaSiC 100-C615	100 nm GaN buffer GaN:Si(1e19)/AlN SL 40 per. 3 nm/3 nm 10 nm GaN cap
1967	NovaSiC 100-C615	100 nm GaN buffer GaN:Si(1e19)/AlN SL 40 per.

		2 nm/3 nm
		10 nm GaN cap
1981	NovaSiC 100-C615	100 nm GaN buffer
		GaN:Si(1e19)/AlN SL 40 per.
		5 nm/3 nm
		10 nm GaN cap
1982	PC570a	1000 nm GaN
1983	PC570a	1000 nm GaN
1984	PC570a	1000 nm GaN
1988	PC570a	1000 nm GaN:Si (T_{Si}=995°C)
1989	PC570a	1000 nm GaN:Si (T_{Si}=995°C)
1990	PC570a	1000 nm GaN:Si (T_{Si}=995°C)
1991	PC570a	100 nm GaN
		20 nm AlGaN (30%)
1992	PC570a	100 nm GaN
		20 nm AlGaN (30%)
1993	SFD03AF-f(Ar-implanted)	No growth visible in RHEED
1994	NovaSiC 100-C497 (Ar-impl.)	100 nm GaN
		20 nm AlGaN (30%)
		10 nm AlN
2044	NovaSiC 100-C615	640 nm GaN
2045	NovaSiC 100-C615	100 nm GaN
		3 nm AlN
		2.5 nm GaN
		0.6 nm AlN
		1.6 nm GaN
		3 nm AlN
		10 nm GaN cap
2046	NovaSiC 100-C615	100 nm GaN
		3 nm AlN
		2.5 nm GaN
		1.0 nm AlN
		1.6 nm GaN
		3 nm AlN
		10 nm GaN cap
2047	NovaSiC 100-C615	100 nm GaN
		3 nm AlN
		2.5 nm GaN
		1.4 nm AlN

		1.6 nm GaN 3 nm AlN 10 nm GaN cap
2048	NovaSiC 100-C615	100 nm GaN 3 nm AlN 2.5 nm GaN 1.9 nm AlN 1.6 nm GaN 3 nm AlN 10 nm GaN cap
2049	NovaSiC 100-C615	100 nm GaN 3 nm AlN 2.5 nm GaN 2.5 nm AlN 1.6 nm GaN 3 nm AlN 10 nm GaN cap
2108	SFB01AA-x	100 nm GaN cycle growth
2109	SFB01AA-u	100 nm GaN:Si cycle growth T_{Si}=1080°C
2110	SFB01AA-o	100 nm GaN:Si cycle growth T_{Si}=1080°C
2111	SFB01AA	50 nm GaN:Si (T_{Si}=1080°C) 1 nm AlN 1 nm GaN (u.i.d.) 1 nm AlN 30 nm GaN:Si (T_{Si}=1080°C)
2112	SFB01AA	50 nm GaN:Si (T_{Si}=1080°C) 2 nm AlN 1 nm GaN (u.i.d.) 2 nm AlN 30 nm GaN:Si (T_{Si}=1080°C)
2113	SFB01AA	50 nm GaN:Si (T_{Si}=1080°C) 3 nm AlN 1 nm GaN (u.i.d.) 3 nm AlN 30 nm GaN:Si (T_{Si}=1080°C)
2114	SFB01AA	50 nm GaN:Si (T_{Si}=1080°C) 4 nm AlN

		1 nm GaN (u.i.d.)
		4 nm AlN
		30 nm GaN:Si (T_{Si}=1080°C)
2115	SFB01AA	50 nm GaN:Si (T_{Si}=1080°C)
		1 nm AlGaN 70%
		1 nm GaN (u.i.d.)
		1 nm AlGaN 70%
		30 nm GaN:Si (T_{Si}=1080°C)
2116	SFB01AA	50 nm GaN:Si (T_{Si}=1080°C)
		1 nm AlGaN 30%
		1 nm GaN (u.i.d.)
		1 nm AlGaN 30%
		30 nm GaN:Si (T_{Si}=1080°C)
2117	SFB01AA	50 nm GaN:Si (T_{Si}=1080°C)
		2 nm AlGaN 30%
		1 nm GaN (u.i.d.)
		2 nm AlGaN 30%
		30 nm GaN:Si (T_{Si}=1080°C)
2118	SFB01AA	50 nm GaN:Si (T_{Si}=1080°C)
		3 nm AlGaN 30%
		1 nm GaN (u.i.d.)
		3 nm AlGaN 30%
		30 nm GaN:Si (T_{Si}=1080°C)
2119	SFB01AA	50 nm GaN:Si (T_{Si}=1080°C)
		1.5 nm AlGaN 50%
		1 nm GaN (u.i.d.)
		1.5 nm AlGaN 50%
		30 nm GaN:Si (T_{Si}=1080°C)
2162	NovaSiC 100-C615	600 nm GaN
2163	NovaSiC 100-C615	600 nm GaN
2164	NovaSiC 100-C615	600 nm GaN
2165	NovaSiC 100-C615	4 nm AlN
		300 nm GaN cycles
2166	NovaSiC 100-C615	100 nm GaN
		100 period SL
		2 nm GaN:Si (T_{Si}=1115°C)
		0.8 nm AlN
		1.5 nm GaN
		2 nm AlN

2167	NovaSiC 100-C615	100 nm GaN 100 period SL 2 nm GaN:Si (T_{Si}=1115°C) 1.0 nm AlN 1.5 nm GaN 2 nm AlN
2168	NovaSiC 100-C615	100 nm GaN 100 period SL 2 nm GaN:Si (T_{Si}=1115°C) 0.8 nm AlN 1.8 nm GaN 2 nm AlN
2169	NovaSiC 100-C615	100 nm GaN 100 period SL 2 nm GaN:Si (T_{Si}=1115°C) 1.0 nm AlN 1.8 nm GaN 2 nm AlN
2170	sapphire	1000 nm hex. GaN MQW 5x 2 nm h-AlN 2.4 nm h-GaN 100nm h-GaN cap
2201	NovaSiC 100-C615	600 nm GaN
2202	NovaSiC 100-C615	600 nm GaN
2203	NovaSiC 100-C615	600 nm GaN
2204	NovaSiC 100-C615	600 nm GaN
2205	NovaSiC 100-C615	800 nm GaN
2206	NovaSiC 100-C615	50 nm GaN 40 period 3 nm AlN 2.1 nm GaN QW 0.8 nm AlN 1.6 nm GaN TEM
2207	NovaSiC 100-C615	50 nm GaN Fountain A undoped 40 period 3 nm AlN

		2.1 nm GaN QW
		0.8 nm AlN
		1.6 nm GaN
2208	NovaSiC 100-C615	50 nm GaN
		Fountain B undoped
		40 period
		3 nm AlN
		2.1 nm GaN QW
		0.8 nm AlN
		1.4 nm GaN
2209	NovaSiC 100-C615	50 nm GaN
		Fountain C undoped
		40 period
		3 nm AlN
		2.1 nm GaN QW
		0.8 nm AlN
		1.2 nm GaN
2210	NovaSiC 100-C615	50 nm GaN
		Fountain D undoped
		40 period
		3 nm AlN
		2.1 nm GaN QW
		0.8 nm AlN
		1.0 nm GaN
2211	NovaSiC 100-C615	50 nm GaN
		Fountain E undoped
		40 period
		3 nm AlN
		2.1 nm GaN QW
		0.8 nm AlN
		0.7 nm GaN
2212	NovaSiC 100-C615	50 nm GaN
		Fountain F undoped
		40 period
		3 nm AlN
		2.1 nm GaN QW
		0.8 nm AlN
		1.9 nm GaN
2213	NovaSiC 100-C615	50 nm GaN

		Fountain A Si-doped 1e19 cm^{-3} 40 period 3 nm AlN 2.1 nm GaN:Si QW 0.8 nm AlN 1.6 nm GaN
2214	NovaSiC 100-C615	50 nm GaN Fountain B Si-doped 1e19 cm^{-3} 40 period 3 nm AlN 2.1 nm GaN:Si QW 0.8 nm AlN 1.4 nm GaN
2215	NovaSiC 100-C615	50 nm GaN Fountain C Si-doped 1e19 cm^{-3} 40 period 3 nm AlN 2.1 nm GaN:Si QW 0.8 nm AlN 1.2 nm GaN
2216	NovaSiC 100-C615	50 nm GaN Fountain D Si-doped 1e19 cm^{-3} 40 period 3 nm AlN 2.1 nm GaN:Si QW 0.8 nm AlN 1.0 nm GaN
2217	NovaSiC 100-C615	50 nm GaN Fountain E Si-doped 1e19 cm^{-3} 40 period 3 nm AlN 2.1 nm GaN:Si QW 0.8 nm AlN 0.7 nm GaN

2218	NovaSiC 100-C615	50 nm GaN Fountain F Si-doped 1e19 cm^{-3} 40 period 3 nm AlN 2.1 nm GaN:Si QW 0.8 nm AlN 1.9 nm GaN
2268	SGB04AG	Growth failed after 22 min GaN
2269	SGB04AG	670 nm GaN
2270	SGB04AG	620 nm GaN
2271	SGB04AG	8 nm AlN 620 nm GaN
2272	SGB04AG	Superlattice on SiC 30 periods 2 nm AlN 4 nm GaN
2273	SGB04AG	Superlattice on SiC 100 periods 2 nm AlN 4 nm GaN
2274	SGB04AG	50 nm GaN buffer Superlattice 100 periods 2 nm AlN 4 nm GaN
2275	SGB04AG	Superlattice on SiC 100 periods 2 nm AlN 7 nm GaN
2276	SGB04AG	Superlattice on SiC 100 periods 2 nm AlN 10 nm GaN

Acknowledgement

Curriculum Vitae

Zur Person

Name	Christian Mietze
Geburtsdatum/Ort	08.08.1983/Hamm

Ausbildung

ab 10/2009	**Promotion** (Universität Paderborn)
	▪ AG Optoelektronische Halbleiter - Gruppe III-Nitride
09/2009	**Master of Science** (Universität Paderborn)
	▪ Gesamtnote: 1,1
	▪ Thema der Masterarbeit: ,,Inter- und Intrasubbandübergänge in kubischen AlGaN/GaN Heteroübergängen''
10/2007 bis 09/2009	**Masterstudiengang Physik** (Universität Paderborn)
09/2007	**Bachelor of Science** (Universität Paderborn)
	▪ Gesamtnote: 2,1
	▪ Thema der Bachelorarbeit: ,,Beschleunigte Alterung/Degradation von AlInGaP Leuchtdioden''
10/2004 bis 09/2007	**Bachelorstudiengang Physik** (Universität Paderborn)
06/2003	**Allgemeine Hochschulreife** (Märkisches Gymnasium Hamm)
	▪ Abiturnote: 1,8
	▪ Leistungskurse: Mathematik, Physik
08/1994 bis 06/2003	**Besuch des Märkischen Gymnasiums in Hamm**